

# **Metal and Semiconductor Heteronanostructures**

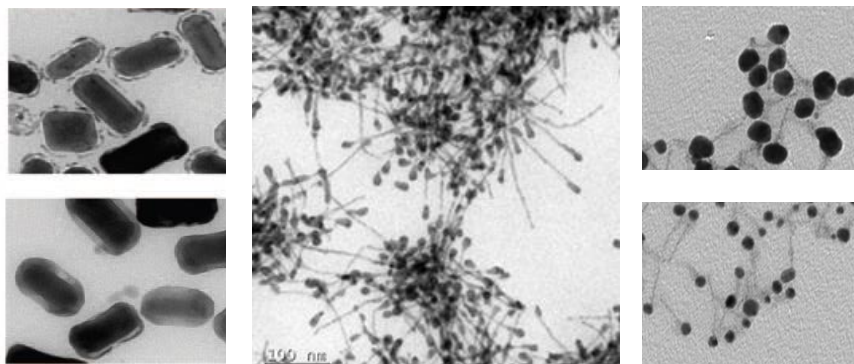
Dissertation

zur Erlangung des Grades

Doktor der Naturwissenschaften

am Fachbereich Chemie, Pharmazie und Geowissenschaften

an der Johannes Gutenberg Universität Mainz



Yuriy Khalavka

Geboren in Stryy, Ukraine

Mainz, 2015

Diese Arbeit entstand im Zeitraum Mai 2007 bis August 2015 im Arbeitskreis Sönnichsen am Institut für Physikalische Chemie, Johannes Gutenberg Universität Mainz.

Johannes Gutenberg-University in Mainz (D77)

Dekan

Erster Berichterstatter :

Zweiter Berichterstatter :

Tag der mündlichen Prüfung: 09.12.2015

“I’m not young enough to know everything.”  
- Oscar Wilde

I acknowledge the Material Science in Mainz graduate School for providing me a PhD scholarship.

## Scientific Publications

### Reflected in the thesis:

**Khalavka, Y.**; Becker, J.; Sonnichsen, C. *Journal of the American Chemical Society* **2009**, *131*, 1871

*Synthesis of Rod-Shaped Gold Nanorattles with Improved Plasmon Sensitivity and Catalytic Activity.*

**Khalavka, Y.**; Sonnichsen, C. *Advanced Materials* **2008**, *20*, 588

*Growth of gold tips onto hyperbranched CdTe nanostructures.*

Becker, J.; Zins, I.; Jakab, A.; **Khalavka, Y.**; Schubert, O.; Sonnichsen, C. *Nano Letters* **2008**, *8*, 1719

*Plasmonic focusing reduces ensemble linewidth of silver-coated gold nanorods.*

Carbone, L.; Jakab, A.; **Khalavka, Y.**; Sonnichsen, C. *Nano Letters* **2009**, *9*, 3710

*Light-Controlled One-Sided Growth of Large Plasmonic Gold Domains on Quantum Rods Observed on the Single Particle Level.*

Carbone, L.; Jakab, A.; **Khalavka, Y.**; Sonnichsen, C. SPIE: San Francisco, California, USA, 2010; Vol. 7575, pp 757505.

*Light-Controlled One-Sided Growth of Large Plasmonic Gold Domains on Quantum Rods Observed on the Single Particle Level.*

### Parts of this thesis are in preparation for scientific publication:

**Yuriy Khalavka**, Sebastian Harms, Andreas Henkel, Malte Strozyk and Carsten Sönnichsen

*Synthesis of Au-CdS@CdSe Hybrid Nanoparticles with Highly Reactive Gold Domain*  
Submitted to Chemistry of Materials

### Additional scientific publications during PhD (not related to the subject of this thesis directly):

**Khalavka, Y.**; Ohm, C.; Sun, L.; Banhart, F.; Sonnichsen, C. *J. Phys. Chem. C* **2007**, *111*, 12886

*Enhanced thermal stability of gold and silver nanorods by thin surface layers.*

Jakab, A.; Rosman, C.; **Khalavka, Y.**; Becker, J.; Trugler, A.; Hohenester, U.; Sonnichsen, C. *Acs Nano* **2011**, *5*, 6880

*Highly Sensitive Plasmonic Silver Nanorods.*

Schubert, O.; Becker, J.; Carbone, L.; **Khalavka, Y.**; Provalska, T.; Zins, I.; Sonnichsen, C. *Nano Letters* **2008**, *8*, 2345

*Mapping the polarization pattern of plasmon modes reveals nanoparticle symmetry.*

Wang, C. H.; Basit, L.; **Khalavka, Y.**; Guo, Y. Z.; Casper, F.; Gasi, T.; Ksenofontov, V.; Balke, B.; Fecher, G. H.; Sonnichsen, C.; Hwu, Y. K.; Lee, J. J.; Felser, C. *Chem. Mat.* **2010**, *22*, 6575

*Probing the Size Effect of Co(2)FeGa-SiO(2)@C Nanocomposite Particles Prepared by a Chemical Approach.*

Zorn, M.; Meuer, S.; Tahir, M. N.; **Khalavka, Y.**; Sonnichsen, C.; Tremel, W.; Zentel, R. *Journal of Materials Chemistry* **2008**, *18*, 3050

*Liquid crystalline phases from polymer functionalised semiconducting nanorods.*

## Abstract

Energy, the environment and health have emerged as strategic priorities in all aspects of our lives. Hybrid materials have already demonstrated good promise in addressing and offering solutions in each of these priority areas. Particularly hybrid nanomaterials containing metal and semiconductor parts are prospective materials for the optoelectronics, photocatalysis and other applications at the nanoscale. Development of new approaches to create such materials is very important direction in nanotechnology.

In this thesis I report several different heterostructures synthesized by means of heterogeneous nucleation. Theoretical aspects of the growth strategies leading to heterostructured nanocrystals are explained together with the descriptions of common characterization techniques.

Approaches to obtain hollow gold nanostructures based on nanorods and gold-tipped CdTe and CdS hybrid materials are described in experimental chapters. These materials demonstrate high catalytic activity, sensitivity to refractive index changes and unusual optical properties as an ensemble and as single particles.

## Table of contents

1	Introduction .....	10
2	Colloidal heterostructured nanocrystals .....	12
	2.1 Homogeneous and Heterogeneous Nucleation in Crystal Growth .....	14
	2.2. Shape Selection and Symmetry Breaking during Nanostructure Growth .....	17
	2.3. Kirkendall effect at nanoscale .....	23
3	Instruments and Techniques .....	27
	Intro .....	27
	3.1. Transmission electron microscopy .....	27
	3.2. Scanning electron microscopy.....	28
	3.3. Energy dispersive X-ray analysis .....	29
	3. 4 TEM-tomography .....	30
	3.4. Ensemble optical measurements.....	31
	3.5 Single particle scattering and fluorescence spectroscopy.....	32
4	Synthesis of rodshaped metal nanorattles.....	34
	4.1. Synthesis of rod-like nanorattles .....	35
	4.2. Sensing properties of the rodshaped nanorattles .....	39
	4.3. Increased Catalytic activity of nanorattles.....	44
	Conclusions .....	48
5	Selective gold deposition on CdTe hyperbranched nanomaterials.....	49
	5.1. Sacrificial growth of Gold on CdTe .....	50
	5.2. Characterization of hybrid structures .....	55
	Conclusions .....	59
6	Photoreduction of Au on rodshaped semiconductor in Chloroform.....	60
	6.1. Photo-induced Au reduction on semiconductor rods. ....	62
	Conclusions .....	73
7	Photoreduction of Gold In Aqueous Media – alternative synthesis of the Au-CdS@CdSe Matchstick Hybrid Nanoparticles.....	75
	Growth of the hybrid nanoparticles .....	76
	Gold domains as reaction centers .....	81
	Catalytic reduction of 4-nitrophenol.....	82
	Shape control of the gold domain.....	84
	Conclusion.....	87

Summary .....	88
References .....	90
Appendix A Synthesis of substrate structures .....	101
Synthesis of gold nanorods.....	101
Nanorattles synthesis.....	101
Synthesis of CdTe hyperbranched and rod-shaped nanoparticles .....	102
Synthesis of rodshaped CdS and CdSe/CdS semiconductor nanorods.....	104
Synthesis of CdSe nanoseeds. ....	104
Synthesis of CdSe/CdS nanorods. ....	105
Transfer of CdSe/CdS to the water phase.....	105
Photo-induced Au reduction on semiconductor rods .....	106
Some Control Experiments.....	106
Acknowledgements .....	112
Curriculum vitae.....	114

## Table of figures

Figure 2.1. Plots of different contributions to the overall free energy.	15
Figure 2.2. Wetting angle.	17
Figure 2.3. Schematic illustration of continuous growth and layer-by-layer growth.	20
Figure 2.4. Schematic illustration of thermodynamically controlled shapes (equilibrium shapes) and kinetically controlled shapes.	20
Figure 2.5. Morphology diagrams illustrating pH and temperature regimes	22
Figure 2.6. Variation of chemical free energy change with the reduction potential	22
Figure 2.7 The positions of the shell/solvent and shell/core interfaces as a function of time.	25
Figure 3.1. TEM Column sketch and images of TEM's used.	28
Figure 3.2. SEM column scheme and the picture of FEI NovaNano 630 SEM	30
Figure 3.3. Electron transitions caused by kicking away electron from the atom.	31
Figure 3.4. TEM-tomography workflow chart.	32
Figure 3.5. Principal scheme of Ocean Optics	33
Figure 3.6. Schematics of the FastSPS dark-field microscope setup.	34
Figure 4.1. Steps of nanorattle creation and corresponding TEM images	36
Figure 4.2. Optical spectra of Rods, thin Ag shell and	37
Figure 4.3. High resolution TEM image of a silver coated gold nanorod.	38
Figure 4.4. Estimation of the increase of surface area in nanorattles compared to nanorods.	39
Figure 4.5. TEM image of the Pd-rattles with gold core	40
Figure 4.6. Plasmon shift of the longitudinal peak of nanorattles by changing of surrounding refractive index.	41
Figure 4.7. Position of the longitudinal plasmon resonance peak vs. refractive index of the surrounding medium for gold nanorods, silver-coated nanorods and nanorattles and overview of the sensitivity IO of different gold nanostructures	42
Figure 4.8. Dependence of the figures of merit (FOM) from the plasmon resonance wavelength for the solutions of gold nanorods and rattles	43
Figure 4.9. Schematics of the dark-field microscope setup.	44
Figure 4.9. Stability of silver-coated particles, closed and porous nanorattles in aqueous media.	46
Figure 4.10. Catalytic properties of Gold Nanorattles	47
Figure 4.9. Normalized absorption at the peak position of para-nitrophenol-NaBH <sub>4</sub> as a function of time after adding different amounts of catalyst.	48
Figure 5.1. TEM images showing growth of gold onto the tips of hyperbranched particles.	51
Figure 5.2. HRTEM image of a gold coated tip of a CdTe branch.	53
Figure 5.3. EDX measurements of hybrid structures, the original CdTe particles and pure TEM substrate.	55
Figure 5.4. TEM image of CdTe particles with a small degree of branching used to measure substrate etching on gold deposition	57
Figure 5.5. TEM image showing gold tips grown on CdTe nanorods.	57

Figure 5.6. TEM Images showing small gold colloids near hybrid gold-CdTe particles.	58
Figure 5.7. TEM images and 3-dimensional reconstructions of the original CdTe nanoparticles before the reaction (left column) and of the gold-CdTe hybrid structures after reaction (right column).	59
Figure 6.1. Sketch of the mechanism for photo-induced growth of large gold domains on semiconductor CdS nanorods.	62
Figure 6.2. The strategy of depositing gold with light driven reduction	65
Figure 6.3. Representative HR-TEM image of the Au-CdS hybrid particle displaying a five-fold symmetry of the gold domain nucleated on one nanorod tip.	68
Figure 6.4. Gold domain diameter extracted from TEM images	70
Figure 6.5. Light driven growth of the gold on TEM-grid substrate.	72
Figure 6.6. Spectral position of the plasmon extinction maximum $\lambda_p$ and its absolute extinction value $I_p$ over time.	73
Figure 6.7. Fusion of the gold domain under prolonged irradiation with UV-light in chloroform.	75
Figure 7.1. Schematics presenting proposed strategy of the nanohybrid synthesis in water solution.	77
Figure 7.2. Au-CdS nanohybrids isolated from the growth solution after 10 (a), 20(b) and 30 (c) minutes of irradiation.	78
Figure 7.3 Aggregation of the hybrid particles	80
Figure 7.4. Berg plot of the plasmon scattering	81
Figure 7.6. Experiments demonstrating accessibility of gold surface to further modification.	82
Figure 7.7. Absorbtion spectra of p-nitrophenol – sodium borohydride before and after the addition of hybrid nanoparticles	83
Figure 7.8. Intensity changes at denoted wavelengths in course of the photoreduction and after addition of surface blocking agent (MUA)	84
Figure 7.9. Hybrid structures produced with different reaction driving forces	86
Figure 7.10. Phase diagrams for the gold reduced at different conditions	87
Figure 7.11. High resolution electron microscopy images of “shovel”-like hybrid nanoparticles,	88
Figure A1. TEM images related to the control experiments.	109

## 1 Introduction

Large-scale production of nanoparticles by chemical synthesis allows the use of the unique properties of nanoscale materials for a variety of new materials, devices, and as a research tool.*[Alivisatos, 1996;Anker, 2008]*

Inorganic nanoheterostructures in which domains of different materials are attached via permanent bonding interfaces in complex architectures are attractive for many fields of contemporary material science. Current achievements in nanochemistry allow precise control on the shape, size and surface coverage of the single-material crystalline nanoparticles,*[Burda, 2005]* but production of the multifunctional structures constructed from single blocs is still under development. I have focused my study on the heterostructures including metal nanoparticles with controllable absorption and scattering resonances resulting from surface plasmon (SP) excitations*[Lee, 2006]* and low-dimensional semiconductor nanocrystals (quantum dots and rods) with tunable electronic levels that can give rise to highly efficient emission and absorption of photons.*[Manna, 2000;Rogach, 2007]*

The advantages of hybrid nanomaterials are not limited to controllable optical properties of single components but extend to the unique possibilities to combine different nanomaterials into composite structures. Such materials often demonstrate properties of two components and potentially synergistic properties caused by interactions between the constituents.*[Subramanian, 2004;Steiner, 2005;Steiner, 2008;Sheldon, 2009;Shaviv, 2010]* Interactions between the constituents can be very strong as both the building blocks and the separation between the components have nanoscale dimensions. The number of possible hybrid materials that can be built from existing

nanostructures is almost unlimited; therefore, the potential for creating highly functional hybrid materials that enable, modify, and control energy processes is very promising.

My thesis is dedicated to the development of new synthetic routes to hybrid and multifunctional metal-semiconductor and metal nanoheterostructures via direct growth of the desired components on the surface of each other, investigation of their properties and tests for possible applications. The thesis is organized as follows:

Theoretical aspects of the growth strategies leading to heterostructured nanocrystals are explained in the second chapter.

Descriptions of the characterization techniques for hybrid materials are given in the third chapter.

Next chapters are about synthesis and properties of following heteronanostructures: rodshaped nanorattles (Chapter 4), gold tipped CdTe hyperbranched nanomaterials (Chapter 5) and asymmetric gold-CdS rodshaped particles (Chapters 6 and 7)

## 2 Colloidal heterostructured nanocrystals

Colloidal nanocrystals (NCs) are inorganic particles made of a few hundred up to a few million atoms, which are synthesized in solution. When particles have this size, the wavefunctions of their electrons are confined by the physical dimensions of the particle, therefore the electronic level structure and the resultant structure, optical, and magnetic properties are greatly modified. Moreover they can be tuned by varying the physical size of the crystal, leading to new phenomena, such as superparamagnetism of magnetic NCs, surface plasmon resonance in Au and Ag nanoparticles, and the size-dependent band gap of semiconductor NCs. [*Burda, 2005*]

Over the past years, a high level of control over morphology was archived in the chemical synthesis of nanoparticles by manipulating the growth kinetics of various crystal phases.[*Yin, 2005*] An important step towards more complex structures was the introduction of branching by switching between two crystal structures within one nanocrystal.[*Manna, 2000*] It is now possible to produce semiconductor, metal and magnetic structures of a large variety of different shapes and of different chemical composition: spheres, rods, tetrapods, tripods, stars and more elaborate shapes of different materials.[*Bunge, 2003;Manna, 2003;Dick, 2004;Milliron, 2004;Kanaras, 2005;Carbone, 2006;Kuno, 2006;Zhu, 2007*]

The next step to the development of functional nanomaterials is to create structures where two or more properties are combined in a desired way. The fabrication of bi-functional or multifunctional NCs has received a great attention in recent years because of their various biomedical, energy conversion and catalytic applications. Hybrid inorganic NCs are emerging as useful probes for magnetic-based targeting, delivery, cell separation, MRI, and fluorescence-based biolabeling applications. [*Carbone, 2011;Buck, 2012*]

To combine different materials in one nanostructure one can choose from one of two approaches. The first is to sequentially grow different domains in one particle. The second is to link separately synthesized nanoparticles with the help of molecular linkers [Lee, 2005; Lee, 2006] [Caswell, 2003] or continuous polymer [Howes, 2010; Lim, 2010] or amorphous silica shell [Liong, 2009]. Both approaches have their features, summarized in table 1.

Table 1.1. Comparison of two approaches to hybrid nanoparticles

<b>Properties</b>	<b>Directly grown domains</b>	<b>Linked domains</b>
<b>Type of connection</b>	Epitaxial or nonepitaxial	Through the molecular linker (covalent bonds)
<b>Size</b>	Sum of the domain sizes	Domain+linker+domain
<b>Thermal stability</b>	high (limited by the diffusion of atoms)	low (limited by thermal stability of the linker and its surface affinity)
<b>Chemical stability</b>	Limited to reactivity of the domains	Limited to the stability of linker-domain bond.
<b>Charge (energy) transfer between domains</b>	Easy (depends on energy band structure of the domain)	Difficult (depends on the size of the linker)
<b>Synthesis steps</b>	2 (substrate and then second phase)	3 (each components and then linkage)
<b>Yield of the hybrids</b>	Almost 100 % due to advantages of heterogeneous nucleation	Limited to the yield of coupling reaction

The assembly can be useful for obtaining well-defined hybrid structures that are a prerequisite for a detailed study of interdomainal interactions. Location, mutual

orientation, size and number of semiconductor and metal components in this case is well-defined and controllable, but for numerous reasons (Table 1.1.) I focused my research on the direct growth of hybrid structures.

Recently, a new type of metal–semiconductor nanostructures has been developed by heterogeneous nucleation that incorporates the metallic and semiconductor (or magnetic) materials into a single unit with various architectures including core/shell, dumbbells, dot-on-rod, and so forth.[*Elmalem, 2008; Costi, 2010; Carbone, 2011*]

This approach has a great potential because the resulting hybrid nanostructures are usually structurally very stable and interactions between domains are enhanced. This is because of the absence of spacer molecules between metal and semiconductor entities, even so for certain applications, for example, luminescence enhancement, dielectric spacer is required to avoid nonradiative energy transfer.

Besides a fundamental interest in the properties of exciton–plasmon interactions, metal–semiconductor nanostructures have also attracted attention for their potential use in applications including optical sensing, light emitters, photovoltaic systems, and quantum information and communication applications.

My efforts were focused on the direct growth approach, applied to the creation of gold–semiconductor hybrid particles starting with hyperbranched CdTe and rodshaped CdS nanocrystals as well as rodshaped Au nanorattles.

## 2.1 Homogeneous and Heterogeneous Nucleation in Crystal Growth

Single-material colloidal NCs are synthesized upon reaction of molecular precursors in a liquid solution that may contain coordinating solvents and some stabilizing agents, such as ligands, polymers, surfactants, or soft templates (e.g.,

micelles). At a suitable temperature, the highly reactive species that are generated or injected, commonly called “monomers” or precursors, induce the nucleation of NCs and sustain their subsequent enlargement. The organic ligands, surfactants or coordinating agents play several key roles along the course of NC formation. They can regulate the solution supersaturation degree upon forming complexes with the monomers and participate in an adsorption–desorption equilibrium at the surface of the growing clusters, preventing irreversible aggregation and ensuring steady growth.

There is a simple theory for the size of a critical nucleus from macroscopic thermodynamic quantities: interfacial surface tension  $\gamma_{1,2}$  (energy/area), and free energy change per unit volume nucleus  $\Delta g$  (energy/volume). For a spherical isotropic nucleus of radius  $R$ , the total free energy is:

$$\Delta G(R) = \frac{4}{3}\pi R^3 \Delta g + 4\pi R^2 \gamma_{1,2} \quad (2.1.)$$

Schematic plot of this function is drawn in Figure 2.1.

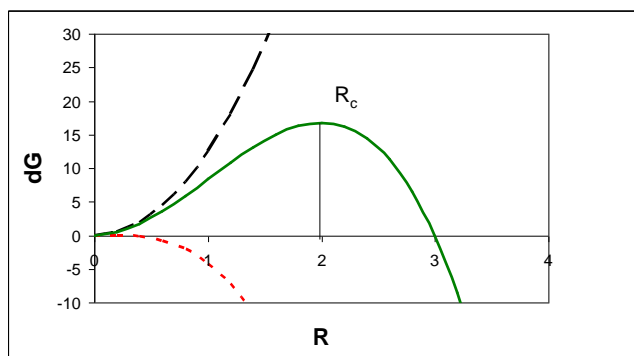


**Figure 2.1.** Plots of different contributions to the overall free energy  $\Delta G$  with arbitrary parameters  $\Delta g = -1$  and  $\gamma = 1$ . Critical radius in this case is about 2 units.

The maximum value of  $\Delta G$  can be considered as an energy barrier that the system must overcome in order to trigger nucleation, while the size corresponding to such value of  $\Delta G$  is referred to as the critical radius.

Suppose nuclei are formed by random fluctuations and a distribution of nuclei sizes  $R$  develops. Any one of the nuclei having a radius  $R_c$  can decrease its free energy continuously by growing (i.e., increasing its radius); all other nuclei cannot grow continuously, but may grow by improbable events such as random attachment of add-atoms or aggregation. The critical radius can be obtained by setting the derivative of the equation (2.1) equal to zero:

$$R_c = -\frac{2\gamma_{1,2}}{\Delta G} \quad (2.2)$$

So, energy barrier that must be overcome by a nucleation process equals:

$$\Delta G_c^* = -\frac{16\pi\gamma_{1,2}}{(3\Delta G)^2} \quad (2.3)$$

Typical synthesis of a colloid should be designed in such a way that the concentration of precursors increases rapidly rising above the threshold value, when a short burst of nucleation (discussed above) occurs with the formation of a large number of nuclei in a short period of time. These particles grow rapidly and lower the monomer concentration below the nucleation threshold, allowing the further growth of these particles.

When a new phase is formed on a surface of the other material, the process is called heterogeneous nucleation (Figure 2.2). At the beginning growth species form nucleus with a cap shape on the relatively flat surface. In this case critical radius of nuclei depends on contact angle ( $\theta$ ) and its size can be expressed as:

$$R_c = \frac{2\pi\gamma_{1,2}}{\Delta G} \left\{ \frac{\sin^2\theta \cdot \cos\theta + 2\cos\theta - 2}{2 - 3\cos\theta + \cos^3\theta} \right\} \quad (2.4)$$

$$\Delta G_c = \left\{ \frac{16\pi\gamma_{1,2}}{(3\Delta G)^2} \right\} \left\{ \frac{2 - 3\cos\theta + \cos^3\theta}{4} \right\} \quad (2.5)$$

Comparing this equation with Eq. (1.3), one can distinguish the first multiplier factor as critical energy barrier for homogeneous nucleation and the second is “wetting factor”.

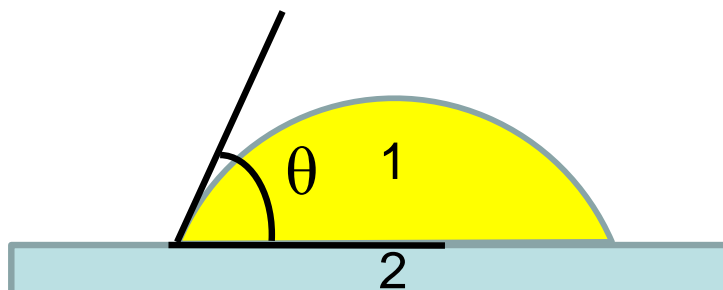


**Figure 2.2.** Wetting angle of the phase 1 on the surface of phase 2.

When  $\theta = 180^\circ$ , i.e. a new phase does not wet on substrate at all, wetting factor is 1 and the critical energy barrier is the same as for homogeneous nucleation. In the case of the contact angle less than  $180^\circ$  the energy barrier is always smaller, which favors nucleation of the new phase on the already existing one. This is especially valid for materials with similar chemical properties and lattice parameters. When the contact angle is  $0^\circ$  – there is no energy barrier for the formation of a new phase on the surface. A good example of this case is the deposition of the same material in the seeded growth approach where separately synthesized seeds from the same or very similar material are used to produce high-quality rodshaped nanoparticles made of gold and CdS [Nikoobakht, 2003;Carbone, 2007].

Several synthetic strategies having been used for hybrid nanoparticles by different growth mechanisms were recently summarized in two insightful reviews [Costi, 2010;Carbone, 2011].

## 2.2. Shape Selection and Symmetry Breaking during Nanostructure Growth

The control of shape and size of the building blocks of hybrid structures dictates their properties and also influences their collective behavior. For instance, the

plasmonic behavior of noble metal nanostructures, the catalytic behavior of Pt-based nanostructures, and the magnetic behavior of nanoparticles depend on the particle size and shape, and hence there have been extensive efforts to develop rational methods for shape- and size-controlled synthesis for a variety of applications.[*Cortie, 2011*]

Surface energy, defined as the energy to create a surface of unit area, is independent of orientation for isotropic phases such as liquids while it depends on the orientation in the case of crystals. The surface with the highest coordination in the plane (close packed surface, for instance) tends to have the lowest surface energy owing to the least number of unsatisfied/broken bonds per unit area. For example, in face centered cubic (fcc) materials, the coordination number (CN) of different crystalline surfaces decreases in the order  $CN(111) > CN(100) > CN(110)$ , which corresponds to an increase in the number of out-of-plane bonds, and correspondingly the surface energy of the 111 is lowest and increases as  $\gamma_{111} < \gamma_{100} < \gamma_{110}$ . Crystal typically adopts a shape that combines several different crystallographic facets to achieve the minimum total surface energy.

Conventional theories of crystal growth typically deal with the formation of the crystalline phase from a supersaturated vapor/liquid or from melts. The mechanism of growth under such situations has been related to the undercooling or the supersaturation ratio. These parameters can be directly related to the driving force available for the motion of the interface. [*Viswanath, 2009*] Crystal growth proceeds by nucleation and a growth mechanism with the driving force given by the associated volume free energy change. A quantitative analysis of the driving force and its relation to the mechanism of crystal growth was provided by Cahn.[*Cahn, 1960*] For the growth of crystals by solidification in a one-component system, the degree of

undercooling quantifies the driving force. Two distinct growth regimes can be identified, and the schematic is shown in Figure 1.4.

A continuous growth by interface motion normal to itself can take place at large driving forces. However, at low driving forces, growth has to proceed by the formation of steps and lateral motion of steps on the surface. The critical driving force for continuous 3-dimensional growth to take place is given as

$$-\Delta G > \pi\sigma g/a \quad (2.6)$$

where  $\sigma$  is the interfacial/surface free energy depending on the growth medium,  $g$  is an interface diffuseness parameter (=1 for sharp interfaces), and  $a$  is the monatomic surface step height. Also for

$$-\Delta G < \sigma g/a, \quad (2.7)$$

growth has to proceed by the layer-by-layer growth involving lateral motion of steps.

The range of

$$\pi\sigma g/a < -\Delta G < \sigma g/a \quad (2.8)$$

corresponds to the transition regime where layer-by-layer growth takes place at lower driving forces with a gradual transition to continuous growth at larger driving forces. The critical driving force for any facet scales with its interfacial energy and is inversely proportional to the step height, and thus the lowest energy facet on which the step height is high (the 111 facet for fcc, for instance) will be the one to advance when the available driving force is low.

The authors of [Viswanath, 2009] assume that the critical values of driving forces are independent of the exact reaction that leads to the formation of the crystal. Thus, the appropriate reaction conditions which ensure that the driving force is lower than the critical value for layer-by-layer growth can be chosen to induce such a growth and form plate-shaped structures.

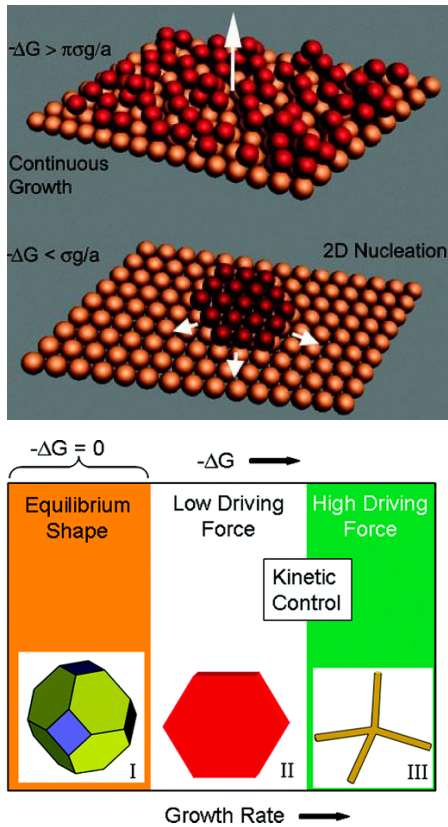


Figure 2.3. Schematic illustration of continuous growth and layer-by-layer growth as related to Cahn's theory for interface motion. [Viswanath, 2009]

Figure 2.4. Schematic illustration of thermodynamically controlled shapes (equilibrium shapes) and kinetically controlled shapes. In the literature kinetic control is used under two different contexts with apparently different meanings. These regimes can be related by considering the driving force ( $-\Delta G$ ) available for the formation of the product. [Viswanath, 2009]

For redox reactions, using the Nernst equation:

$$E = E^\circ - (RT/nF) \ln K, \quad (2.9)$$

it follows that the formal reduction potential  $E$  of a redox couple is dependent on the temperature  $T$ , and the equilibrium constant  $K$ , which consists of the concentration of the involved species. Since nanoparticle syntheses usually conducted in dilute solutions one could equate activity to concentration. Assuming that  $E^\circ$  denoting the standard reduction potential and  $n$  representing the number of electron changes are fixed for a particular system.  $R$  is the universal gas constant and its value is taken as  $8.314 \text{ J mol}^{-1} \text{ K}^{-1}$ , and  $F$  is  $96\,500 \text{ C}$ .

The free energy change is related to the total electromotive force of the reaction by the equation

$$\Delta G_r = -nFE \quad (2.10)$$

and

$$\Delta G_r = -nF (E^\circ - (RT/nF) \ln K) \quad (2.11)$$

As an example, consider the reduction of gold ions by water molecules, it looks like:



$$E^\circ = E^\circ_r(\text{Au}) - E^\circ_r(\text{H}_2\text{O}) = -0.228 \text{ V}$$

One can derive the equation for  $\Delta G_r$  as function of pH and temperature:

$$\Delta G_r (\text{kJ/mol}) = 66.006 - 0.0574(\text{pH})T - 0.1262T \quad (2.12)$$

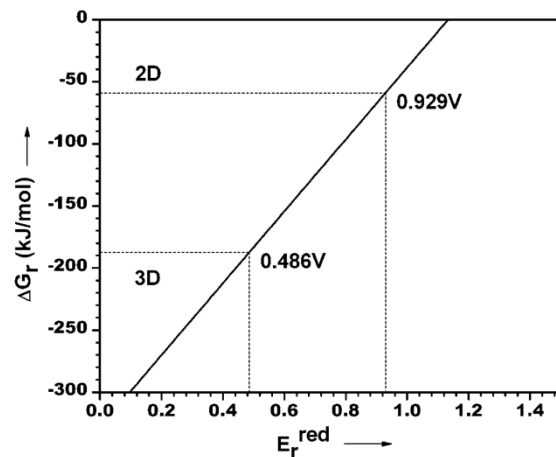
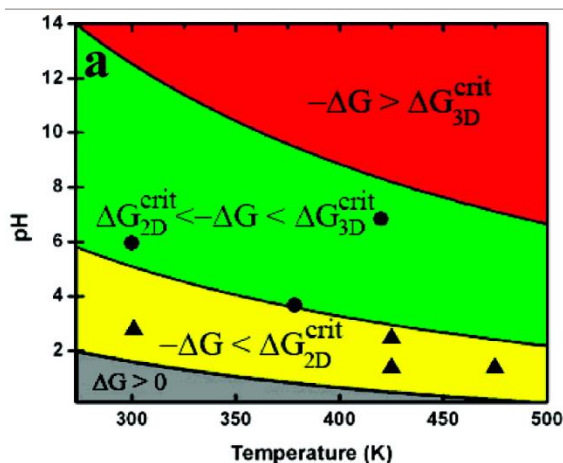


Figure 2.5. Morphology diagrams illustrating pH and temperature regimes where the layer-by-layer growth mechanism (yellow) and continuous growth (red) is operative for (a) Au. The calculations are based on metal ion concentrations of 1 mM for Au. The experiments carried out at different pHs and temperatures to obtain plate-shaped and equiaxed nanostructures are marked as triangles ( $\blacktriangle$ ) and circles ( $\bullet$ ), respectively. [Viswanath, 2009]

Figure 2.6. Variation of chemical free energy change with the reduction potential of any arbitrary reductant at temperature  $T = 300$  K, for Au with 1 mM concentration of the  $\text{AuCl}_4^-$  ion. Dotted horizontal lines are drawn to delineate the layer-by-layer growth and continuous growth regimes, and the vertical dotted lines indicate the critical potential values. [Viswanath, 2009]

Critical driving force below which layer-by-layer growth takes place on 111 planes ( $-\Delta G_{2D}$ ) and above which the interfaces advance by the continuous growth mechanism ( $-\Delta G_{3D}$ ), calculated using this theory is  $-60$  kJ/mol and  $-188$  kJ/mol respectively. (Table 2.1.)

Figure 2.6 represents the case for Au with  $\text{AuCl}_4^-$  as the starting precursor. the line for Au lies in the positive potential zone, which suggests that even a weaker reducing agent such as water or EG can cause reduction. In case of Au, the critical driving force for layer-by-layer growth mechanism is  $-60$  kJ/mol with the corresponding potential ranging from 0.929 to 1.13 V as indicated by the vertical lines in Figure 2.5. As the reduction potential of water ranges from 1.23 to 0.4 V under the conditions of pH and temperature employed even water can be used to reduce  $\text{HAuCl}_4$  to form Au platelets.[Viswanath, 2009]

**Table 2.2.** Values of interfacial energies and monatomic step heights on the surface that have been used to calculate the critical driving forces for 2D nucleation and continuous growth. [Viswanath, 2008]

System	Interfacial energy ( $\text{mJ m}^{-2}$ )	Monatomic step height ( $\text{\AA}^\circ$ )	$\Delta G_{crit 2D}$ ( $\text{kJ mol}^{-1}$ )	$\Delta G_{crit 3D}$ ( $\text{kJ mol}^{-1}$ )

Au (111)	1.39	2.3	-60	-188
Ag (111)	1.09	2.36	-46	-144
Pt (111)	2.20	2.26	-97	-304
Pd (111)	1.74	2.24	-78	-245

With an increase in the reduction potential of the reducing agent, the driving force also increases. Similarly, an increasing pH and/or temperature also increase driving force of the reaction in both redox and precipitation reactions as is seen from the morphology diagrams. However, the influence of concentration is more complicated and could cause either an increase or a decrease in the driving force depending upon how it affects the equilibrium constant of the reaction.

Another important factor of symmetry breaking is surfactant molecules. Interacting with the surface they can selectively decrease free energy of certain facets and therefore define final shape of the crystal leading to variety of shapes like: sphere; spheroid; cube; cuboctahedron; octahedron; tetrahedron; right bipyramid; decahedron; icosahedron; thin plate with a triangular, hexagonal, or circular profile; and rod or wire with a circular, square, rectangular, pentagonal, or octagonal cross-section.[Xia, 2009]

### 2.3. Kirkendall effect at nanoscale

An interesting phenomenon happens when heterogeneous growth occurs under conditions when atoms of each phase can interdiffuse fast, particularly when silver or silver-coated nanoparticles react with gold salts in galvanic replacement reaction. This phenomenon is called Kirkendall effect in tribute to O.E. Kirkendall who found in his interdiffusion experiment with contacting Cu and alpha-brass plates that displacement of one part of diffusion couple relative to another one was

accompanied by a pore formation, which was a reliable evidence of the vacancy diffusion mechanism [Kirkendall, 1942]. If the temperature is high enough for vacancies injected into the core region to sample a fraction of the core volume, a significant fraction of the vacancies should end up coalescing into a single large void.

Alivisatos group has published simple theoretical model of this effect applicable to nanoscale materials.[Yin, 2006] They dealt with the kinetics of the flux and derived the criteria and timescales for the formation of hollow nanospheres.

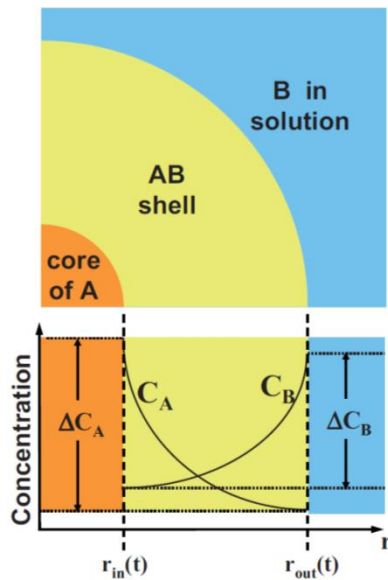


**Figure 2.7** The positions of the shell/solvent and shell/core interfaces are measured radially and are a function of time.  $r_{in}$ ,  $r_{out}$ : radial positions of the inner and outer boundaries of the  $A_mB_n$  shell at time  $t$ .  $C_A$ ,  $C_B$ : concentrations of species A and B. [Yin, 2006]

This treatment was based on a steady-state diffusion (i.e., a concentration profile of the vacancies within the product shell is constant with time), which is governed by Fick's first law. This means that the diffusion of mass, as well as the vacancies, is induced by the difference in atom concentration. The position of the inner boundary of the growing  $A_mB_n$  shell at time  $t$  is denoted  $r_{in(t)}$  and the position of the outer boundary (the  $A_mB_n$ /solution interface) at time  $t$  is denoted  $r_{out(t)}$ . The magnitude of the flux for species  $i$ ,  $J_i$ , at radial position  $r$  is defined by the steady-state diffusion equation at time  $t$  and has the form:

$$|J_i| = \frac{D_i \Delta C_i}{r^2} \times \frac{r_{\text{in}}(t) r_{\text{out}}(t)}{r_{\text{out}}(t) - r_{\text{in}}(t)} \quad (2.13)$$

where  $D_i$  refers to the diffusion coefficient for the transport of either species A or species B through the AB phase and  $\Delta C_i$  refers to the concentration drop for that species across the AB shell.

Assuming that inward growth rate of the shell should be proportional to the flux of B at  $r = r_{\text{in}}(t)$  and outward growth of the shell should be proportional to the flux of A at  $r = r_{\text{out}}(t)$  leads to the ratio of the inward and outward growth rate:

$$\left| \frac{dr_{\text{out}}}{dt} / \frac{dr_{\text{in}}}{dt} \right| = - \frac{n \cdot D_A |\Delta C_A|}{m \cdot D_B |\Delta C_B|} \times \left[ \frac{r_{\text{in}}(t)}{r_{\text{out}}(t)} \right]^2 \quad (2.14)$$

where  $D_A$ ,  $\Delta C_A$ , and  $n_A$  denote the diffusivity, concentration difference, and volume density of A in the product layer, respectively. The prerequisite for formation of hollow structures is derived to be as follows:

$$\frac{n \cdot D_A |\Delta C_A|}{m \cdot D_B |\Delta C_B|} > (V_{\text{AB}} - 1) \quad (2.15)$$

Here  $V_{\text{AB}}$  is the volume of compound AB produced per volume of initial starting material A.

The suggested model allows also a prediction of the conditions required to produce stable hollow particles. To avoid shrinking of the void under the Gibbs pressure, reaction time should be much higher than:

$$t_{\text{shrink}} \approx \frac{L^3 kT}{10\gamma D\Omega} \quad (2.16)$$

with  $\gamma$  and  $\Omega$  denoting the surface energy of the shell material and the volume of a vacancy, respectively, and  $L$  corresponding to initial size of the void. If the time of the synthesis is limited by the slowest component B it can be expressed as

$$t_{\text{synth}} \approx \frac{d^2 V_{\text{AB}}^{2/3}}{6D_A \Delta C_A} \quad (2.17)$$

In this expression, concentration  $C_A$  refers to the local volume fraction of A in the compound AB.

In a hollow shell of compound AB, relaxation of the shell is limited by the diffusivity of the slower species, assumed here to be species B, so it is can be written:

$$\frac{t_{\text{shrink}}}{t_{\text{synth}}} = \frac{3}{5} \times \frac{\Delta C_A}{V_{\text{AB}}^{2/3}} \times \frac{kT_{\text{synth}} d}{\gamma \Omega} \times \frac{D_A}{D_B} \quad (2.18)$$

This suggests that higher temperature makes formation of stable hollow structure favorable.

I have utilized Kirkendall effect to the production of the nanorattles – hollow nanoparticles with solid nanorods inside with enhanced sensitivity to environment refractive index and catalytical properties.

### 3 Instruments and Techniques

#### Intro

It is very important to use reliable, appropriate tools to characterize materials that are produced in the experiments in nanochemistry. In this chapter I briefly describe basic principles of employed instruments.

#### 3.1. Transmission electron microscopy

Transmission electron microscopy (TEM) has been the main characterization technique used to determine the size and shape of the produced nanoparticles. TEM uses a particle beam of electrons to illuminate the specimen and produce a magnified image. It has greater resolving power than a light-powered optical microscope, because electrons have wavelengths about 100,000 times shorter than visible light (photons). Typical construction of the TEM is demonstrated in Figure 3.1

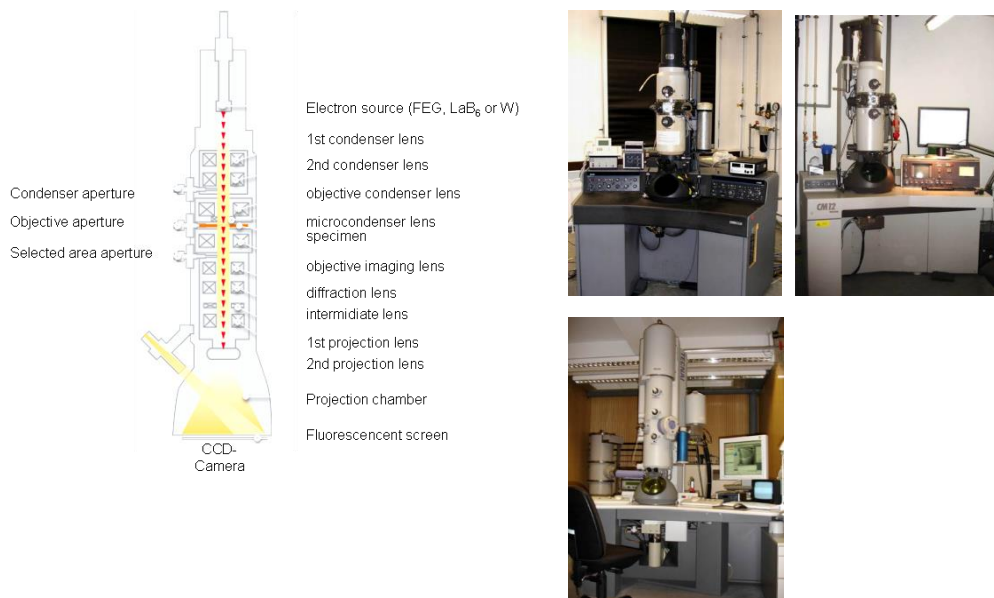


Figure 3.1. TEM Column sketch (Modified Image of FEI) and images of TEM's used.

Electrons emitted from the source are passing several electromagnetic lenses. In transmission, the electron beam is first diffracted by the specimen, and then, the lenses re-focus the beam into a Fourier-transformed image of the diffraction pattern for the selected area of investigation.

Images produced by the TEM are visible on the fluorescent screen or can be digitized by charged-coupled device (CCD) camera and processed with imaging software Digital Micrograph and saved in .dm3 or .tiff formats.

Low-magnification TEM imaging was performed on a Philips CM12 (Slow-scan 2K CCD camera, LaB6 gun), EM-420 (1K CCD camera, LaB6 gun) electron microscopes operating at 120 kV. High-resolution (HR)-TEM images are acquired in a FEI Tecnai-F30 microscope operating at 300 kV (2 slow-scan 1K CCD cameras, 1 TV-rate CCD camera and Field emission gun).

TEM samples were prepared by drop-casting diluted and cleaned solutions of nanocrystals onto carbon or carbon-formvar coated copper grids from the company «PLANO». Afterwards, the deposited samples are allowed to completely dry at 60°C before examination.

### **3.2. Scanning electron microscopy**

Scanning electron microscope produces images by probing the specimen with a focused electron beam that is scanned across an area of the specimen (raster scanning). At each point on the specimen the incident electron beam loses some energy, which is converted into the signal by the variety of detectors. The types of signals produced by an SEM include secondary electrons (SE), back-scattered electrons (BSE), characteristic X-rays (EDX), light (cathodoluminescence), specimen current and transmitted (STEM) electrons. The resulting image is calculated from the signals from each scanned point of the sample by the software.

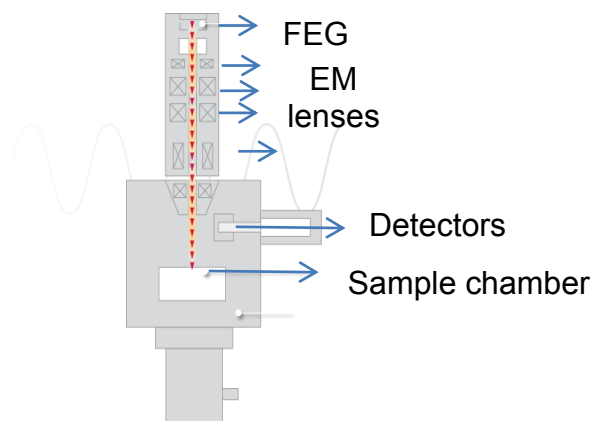


**Figure 3.2.** SEM column scheme (left panel) and the picture of FEI NovaNano 630 SEM used by the author.

High resolution FEI NovaNano 630 SEM with the range of acceleration voltages: 50V-30kV, equipped with field emission gun (FEG), low-vacuum mode and variety of the detectors (Everhart-Thornley detector (ETD), through the lens detector (TLD), low-vacuum and high contrast detector (vCD), retractable STEM detector and EDX) was used to perform scanning electron images.

This instrument allowed me to investigate hybrid nanoparticles directly on the flow-cell surface, to evaluate number of aggregates and single particles in the field of view.

### 3.3. Energy dispersive X-ray analysis

Energy dispersive x-ray analysis is a technique based on energy of X-rays generated by atoms being hit with electrons. The incident beam excites an electron in an inner shell, kicking it out from the shell while creating a hole where the electron was. (Figure 3.3)

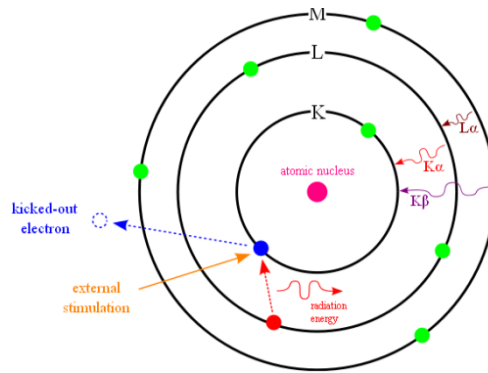


**Figure 3.3.** Electron transitions caused by kicking away electron from the in the atom. (Wikipedia)

An electron from an outer, higher-energy shell then fills the hole, and the difference in energy between the higher-energy shell and the lower energy shell leads to the emission of X-rays. As the energies of the X-rays are characteristic of the difference in energy between the two shells, and of the atomic structure of the element from which they were emitted, this allows the elemental composition of the specimen with nanometer accuracy to be measured.

EDX detectors from EDAX-company attached to both transmission and scanning electron microscopes where used to study chemical composition of the heteronanostructures at single particle level, as well as elemental mapping and line-scanning plots.

### 3. 4 TEM-tomography

We used TEM-tomography to reveal 3D structure of studied materials. This technique requires several steps. (Figure 3.4)

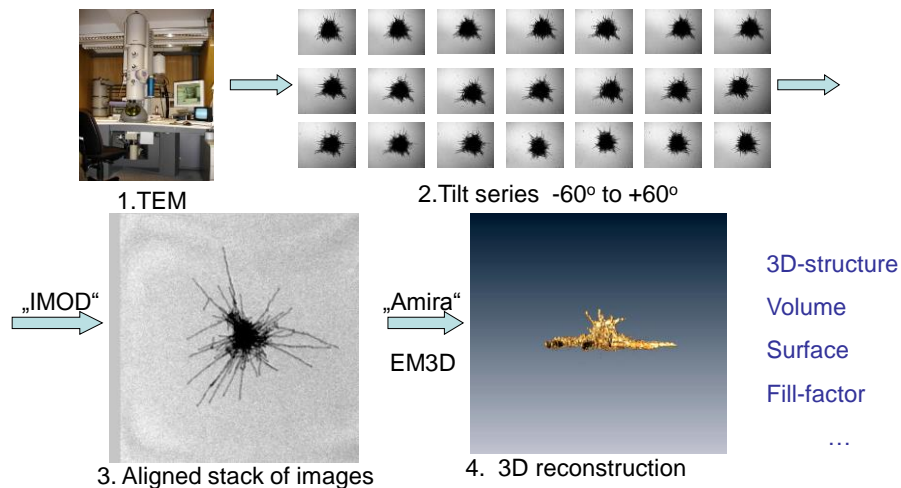


**Figure 3.4.** TEM-tomography workflow chart.

First, series of TEM images are acquired in the manual or in automated way. Images are taken at different angles, usually from  $-60^\circ$  to  $+60^\circ$  with a step of  $2^\circ$  or  $5^\circ$ . Special specimen holder from «Gatan» have been used for this operation. Then all images are aligned in stack, and using the complex mathematical algorithms are converted into a stack of slices – tomogram. It can be used to create 3D-model of the object via process called “volume rendering”, and also to estimate some important measures like surface area, volume and so on. It is also frequently used to study assembly of different nanomaterials in 3-dimensional structures. [Hungria, 2008]

I have used “EM3D” [Ress, 2004], “Amira”. and “IMOD ETOMO” [Kremer, 1996] software packages to create 3D reconstructions and obtain parameters of the investigated nanoparticles.

### 3.4. Ensemble optical measurements

Optical properties like UV-Vis of nanoparticles are important criteria for their possible applications. There is a strong relationship between the size and shape of the particles – they are widely used to monitor nanoparticle formation, growth and aggregation.

Absorption and fluorescence spectroscopy of nanoparticles in solutions was performed with fiber array spectrophotometers (USB-2000 and USB-4000, Ocean Optics ) (Figure 3.5) with halogen lamp or white light diode as a source of the white light.

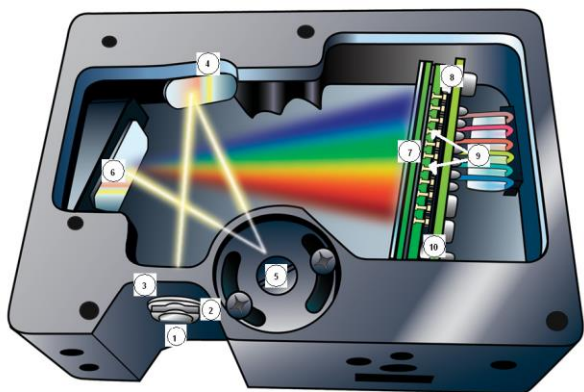


**Figure 3.5.** Principal scheme of Ocean Optics 1 - SMA 905 Connector, 2 - Slit, 3 - Filter, 4 - Collimating Mirror, 5 - Grating, 6 - Focusing Mirror, 7 - L4 Detector Collection Lens. 8 - Detector (UV or VIS). 9 - Variable Longpass Order-sorting Filters; 10 - Detector window USB4000 Fiber Optic Spectrometer, Installation and Operation Manual, Document Number 211-00000-000-02-0908)

Those spectrometers allow time acquisition of the full spectra with high speed in the range 380 – 1000 nm. Analysis of the spectral data was done with supplied software OOI Base or with the script called «Spectralyzer», developed in the Nanobiotechnology group of professor Soennichsen (Uni-Mainz).

To measure fluorescence spectra UV-lamp from CarlRoth (excitation wavelength 366 nm) was used as an excitation source. It was mounted under the quvette filled with diluted solution of nanoparticles, positioned in front of the spectrometer slit. Integration time was adjusted to achieve stable fluorescent signal.

### 3.5 Single particle scattering and fluorescence spectroscopy

«FastSPS» setup built by Jan Becker and Plasmoscope (built by Arpad Jakab) were used to measure single particle spectra. Their schematics are drawn below:

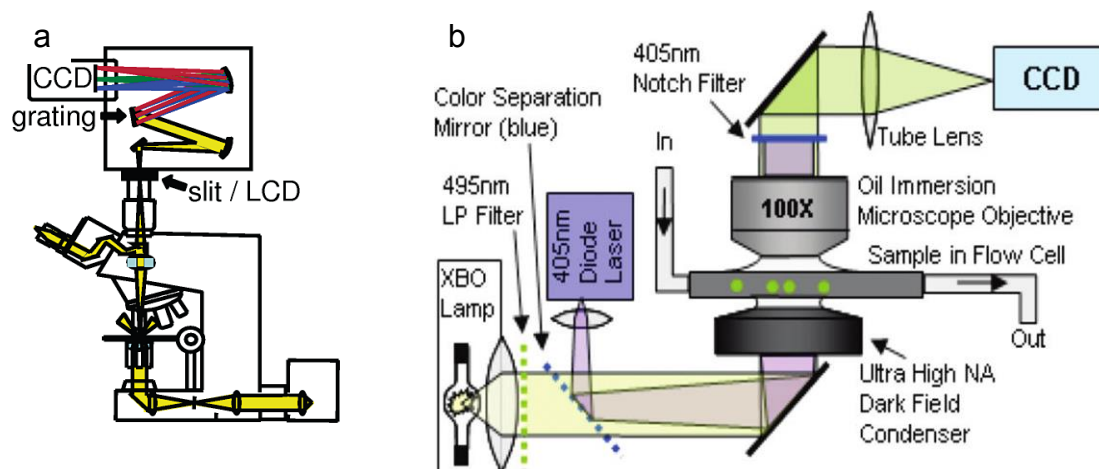


Figure 3.6. a) Schematics of the FastSPS dark-field microscope setup. The scattered light is directed either to the ocular or to an imaging spectrometer, where the light is dispersed and the resulting spectrum captured by a CCD camera. [Becker, 2007] (b) “Plasmoscope” setup with a 405 nm laser diode for photoexcitation of the semiconductor nanorods and white light darkfield contrast for the observation of gold domains. A 495 nm long pass (LP) filter prevents nanorod excitation by the white light. The laser is coupled-in by a dichroic mirror and blocked out after the objective by a notch filter [Carbone, 2009].

The setups allow for the recording of scattering intensities and single particle spectra with an imaging spectrometer. FastSPS uses a spatially addressable electronic shutter based on a liquid crystal device to investigate particles randomly deposited on a substrate, orders of magnitude faster than other techniques, while advantages of “Plasmoscope” are possibility to couple laser and lamp illumination, precise positioning and high tunability of the device.

## 4 Synthesis of rodshaped metal nanorattles\*

Since ancient times, the vivid colors of plasmonic nanoparticles have been used for decorative purposes.[*Mulvaney, 1996*] Recently, the extraordinary strong polarizability at the plasmon frequency enables new applications in optical sensing, imaging, and therapy.[*Cozzoli, 2004;Perez-Juste, 2005;Rosi, 2005;Eustis, 2006*] The plasmon frequency depends on the refractive index of the immediate environment,[*Murphy, 2008*] which forms the basis of many sensing schemes.[*Anker, 2008*] The sensitivity of plasmonic sensors for the detection of changes in the environment varies greatly and depends on the particle material and its morphology (shape and size).[*Lee, 2006*] The first single particle ‘attoliter’ plasmonic sensors were realized with spherical gold and silver nanoparticles with relatively low sensitivity.[*McFarland, 2003;Mock, 2003;Raschke, 2003*] The sensitivity has been improved using gold nanoshells,[*Sun, 2002;Raschke, 2004*] rod-shaped[*Baciu, 2008;Nusz, 2008*] or bipyramid-shaped nanoparticles.[*Dmitriev, 2008*] The reason for using non-spherical particles is the desire to shift the plasmon resonance to lower frequencies – away from competing interband transitions – to decrease the plasmon linewidth.[*Sönnichsen, 2002*] Some materials such as silver show smaller plasmon damping than gold but are chemically less stable and more difficult to prepare in the form of nanocrystals with narrow size distribution and without defects.

In principle, candidates for very sensitive plasmonic sensors should have a large part of the plasmon field penetrating the accessible dielectric environment. This favors hollow structures (cages, boxes) or nanoparticle filled cages (rattles).

---

\* A version of this chapter was published as **Khalavka, Y.;** Becker, J.; Sönnichsen, C. *Synthesis of Rod-Shaped Gold Nanorattles with Improved Plasmon Sensitivity and Catalytic Activity* *Journal of the American Chemical Society* **2009**, *131*, 1871

So far, only a few examples of nanorattles with both core and shell made of metals were reported. Xia and co-workers synthesized spherical nanorattles consisting of Au/Ag alloy cores and shells by means of an electroless galvanic replacement reaction. [Sun, 2004] More recently, a promising synthesis of nanorattles with spherical Au core and Pt/Ag shell has been reported by Yang *et al.*, [Yang, 2006] but data on their chemical stability and plasmon sensitivity are lacking.

I developed a strategy for the preparation of rod-shaped gold nanorattles, i.e. hollow gold nanostructures with a solid nanorod inside (Figure 4. 1). Furthermore, I demonstrated that the rattles exhibited higher catalytic activity compared to gold rods due to the increased surface to volume ratio while preserving high plasmon sensitivity.

#### 4.1. Synthesis of rod-like nanorattles

Rod-shaped gold nanorattles combine the advantages of rods (low plasmon resonance frequency, high polarizability, and small plasmon linewidth) with the high surface area of hollow structures and show improved optical sensitivity compared to gold nanorods, spheres, and hollow spheres in the visible range of light. In contrast to the spherical Au/Ag nanorattles reported by Xia *et al.*, [Sun, 2004] rod-shaped nanorattles presented here consist entirely of pure gold, which makes them chemically stable in aqueous environments.

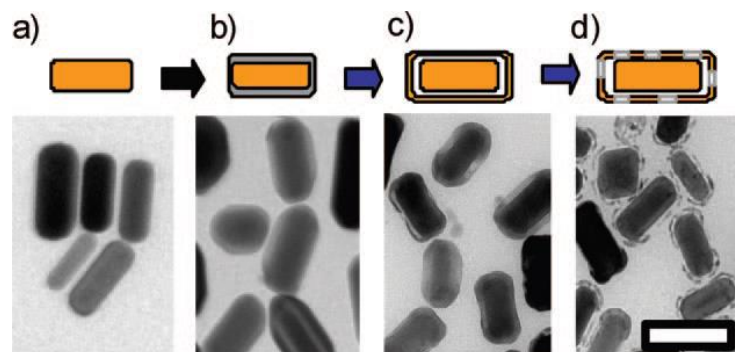
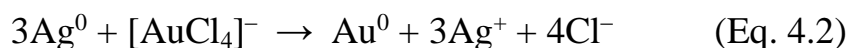


**Figure 4.1.** Steps of nanorattle creation (above) and corresponding TEM images (below)

The strategy of rod-shaped nanorattle synthesis closely follows the general procedure used by Xia *et al.* [Sun, 2004] to form spherical nanorattles with Au-Ag core. I started with preformed gold nanorods and coat them with a thin silver layer via reduction with ascorbic acid (Asc):



In a second step, this silver layer is replaced by gold:



This leads to the formation of a closed Ag-Au shell (Figure 1c). Further addition of  $\text{HAuCl}_4$  produces a porous Au cage around the rods (Figure 1d). The silver layer produced by the reduction of silver with ascorbic acid in the presence of poly(vinylpyrrolidone) (PVP) grows epitaxially on the cetyl-trimethylammonium-bromide (CTAB) coated gold nanorod surface in contrast to citrate stabilized spheres. [Liu, 2004; Baciu, 2008]

I used two thicknesses of silver shells in this study: 3 and 6 nm as estimated from the difference in the mean diameter between coated and bare rods measured on TEM images. The silver shell leads to the characteristic blue shift of the plasmon resonance wavelength (Figure 4.2).

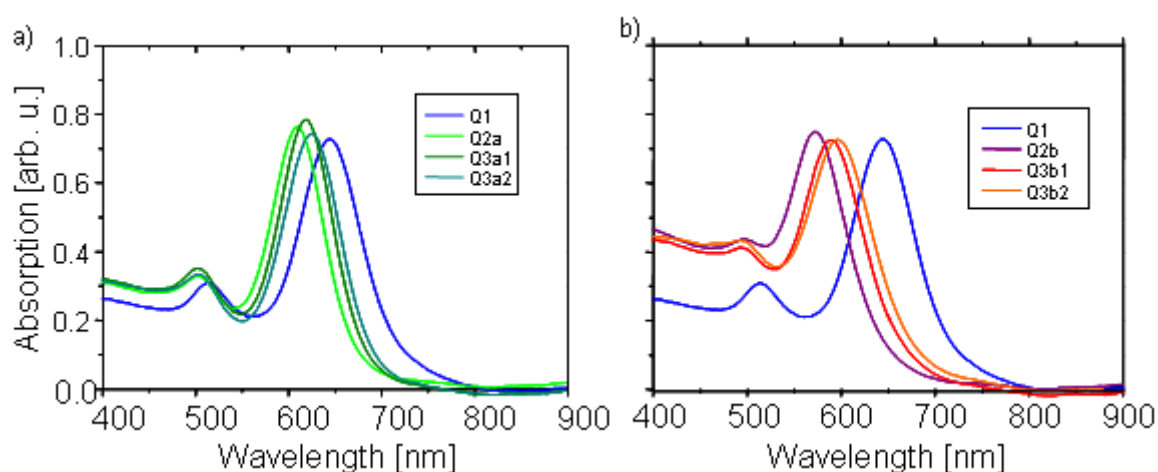


**Figure 4.2.** Optical spectra of a) Rods (Q1), thin Ag shell (Q2a) and rattles (Q3a1 and Q3a2) made of them, b) Rods with thick Ag shell (Q2b) and rattles (Q3b1 and Q3b2) made of them.

While the silver coating leads to a blue shift of the resonance wavelength, the replacement of the silver shell with a gold cage redshifts the resonance wavelength.

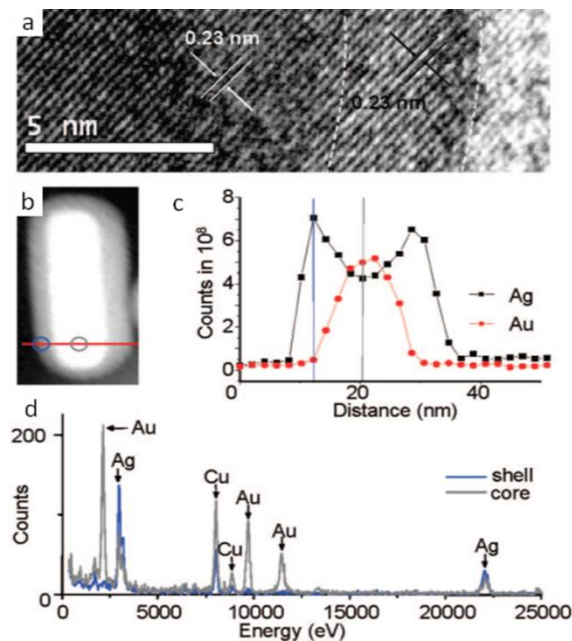


**Figure 4.3.** a) High resolution TEM image of a silver coated gold nanorod. Dashed lines indicate the borders of the silver shell.

Equal lattice spacing (0.23 nm) in the Au core and the Ag shell confirms epitaxial growth ([111] planes). b) STEM image of the silver coated gold nanorod with the position of the EDX linescan (red line) c) Profile of the Au and Ag elemental distribution. d) Two representative EDX spectra (at the positions indicated with circles in b).

The second step is a galvanic replacement reaction between the silver shell and an aqueous  $\text{HAuCl}_4$  solution.

Silver coated particles solutions were heated to  $100^\circ\text{C}$  with stirring. Then either  $60\ \mu\text{L}$  or  $120\ \mu\text{L}$  of  $1\ \text{mM}$   $\text{HAuCl}_4$  (Aldrich) were added to rods with  $3\ \text{nm}$  silver coating, either  $120\ \mu\text{L}$  or  $240\ \mu\text{L}$  of gold solution were added to rods with  $6\ \text{nm}$  silver coating. In case of Pd–nanorattles,  $320\ \mu\text{L}$  of  $1\ \text{mM}$   $\text{Pd}(\text{NO}_3)_2$  (Aldrich) was added instead of the gold solution to rods with  $6\ \text{nm}$  silver coating. The addition of these metal salt solutions was performed dropwise over  $10\ \text{min}$  with the help of a syringe pump. Afterwards the vial was rapidly cooled down in a waterbath.

Xia et al. performed this step at  $100^\circ\text{C}$  to avoid  $\text{AgCl}$  co-precipitation during the galvanic replacement reaction.<sup>[Sun, 2004]</sup> We keep the concentrations of silver and chlorine ions low enough that the solubility product of  $\text{AgCl}$  is not reached even at room temperature. Since the reaction at room temperature leads to non-uniform cages, we heat it to  $100^\circ\text{C}$  in order to improve the quality of the

outer shell. Hollow rattles form instead of a simple gold shell on a gold core due to the nano-scale Kirkendall effect.[Kirkendall, 1942;Yin, 2004;Yin, 2006;Fan, 2007] The higher diffusion rate of silver compared to gold and the imbalance of the material flow (see Eq. 4.2) leads to an accumulation of vacancies on the inner silver-gold interface.[Meyer, 1969] Rattles grown from silver-coated rods with the 6 nm shell are more uniform compared to those grown from the 3 nm shell. Depending on the amount of gold added in the second step, rattles with closed and porous outer shells were synthesized.

Geometrical calculations based on TEM measurements give data presented in Figure 4.4.

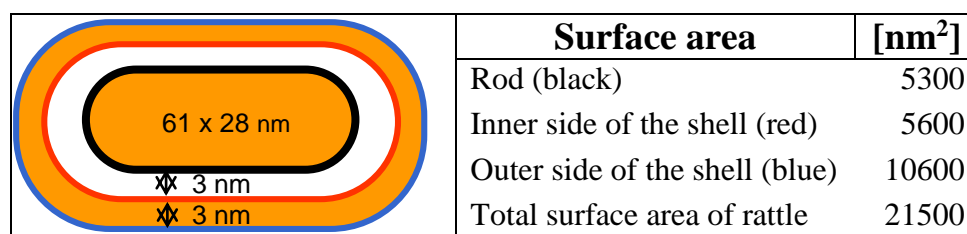


**Figure 4.4.** Estimation of the increase of surface area in nanorattles compared to nanorods. Dimensions of the rattle used for the calculations are shown. Total surface area of the nanorattle (21500 nm<sup>2</sup>) is approximately 4 times bigger than that of the initial rod (5300 nm<sup>2</sup>).

With set silver shell volume of about 10200 nm<sup>3</sup> and cage volume of 14300 nm<sup>3</sup> (giving  $V(AB) = 1.3$ ) ratio between diffusion constants for silver and gold, calculated with equation 2.15 should be larger than 0.9. Assuming this ratio independent from the temperature we can compare this criteria with known value which is 2,26 as determined by R. O. Meyer for the bulk materials[Meyer, 1967]. This means that our results fit and further validate proposed theory of the formation of the hollow structures via nanoscale Kirkendall effect. Replacing the H<sub>2</sub>AuCl<sub>4</sub> in the cage growth reaction with Pd(NO<sub>3</sub>)<sub>2</sub> leads to a Pd shell around the solid gold nanorod (Figure 4.5)

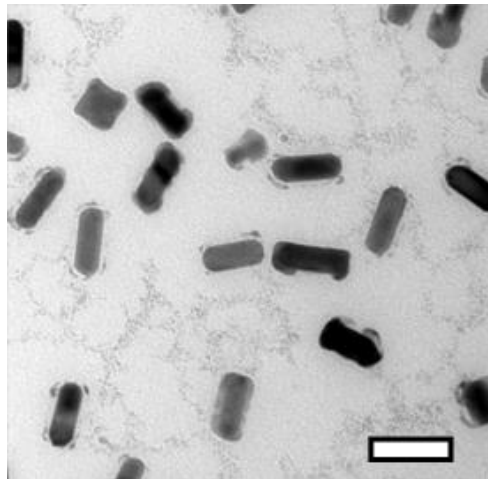


**Figure 4.5.** TEM image of the Pd-rattles with gold core used for the catalytic activity measurements. Scalebar is 60 nm.

#### **4.2. Sensing properties of the rodshaped nanorattles**

The maximum of the extinction spectra corresponding to the longitudinal plasmon mode of the nanorattles is in-between the maxima for the initial gold nanorods and the silver-coated particles (Figure 4.2). The distance between the shell and the particle is small enough to lead to an effective plasmon coupling creating a mode similar to that of a completely filled nanoparticle with the same outer dimensions. Since the nanorattles have a lower overall aspect ratio than the initial rods, the resonance wavelength is shifted slightly to the blue compared to the initial rods.

In order to test the plasmon sensitivity to changes in the dielectric environment, we systematically varied the refractive index of the aqueous surrounding by adding sugar, ethylene glycol, or glycerin to suspensions of gold particles. The refractive index  $n$  of the solutions was measured with a digital refractometer (Refracto 30PX) and the position of the plasmon resonance peak  $\lambda_{\text{res}}$  was determined from an extinction spectrum (Figure 4.6).

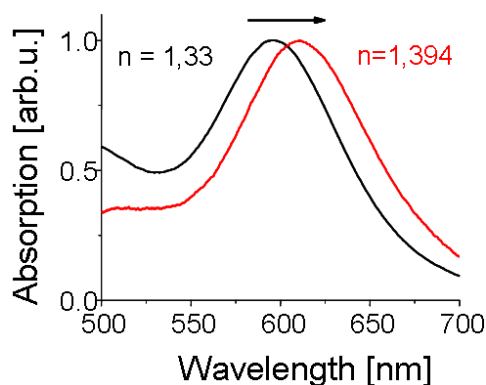


**Figure 4.6.** Plasmon shift of the longitudinal peak of nanorattles by changing of surrounding refractive index.

The plasmon resonance shifts linearly to higher wavelength with increasing refractive index  $n$  of the surrounding environment (Figure 4.7). [Murphy, 2008] In our group we use the constant of proportionality  $\text{IO}$  (Cyrillic ‘Yu’), in units of nanometers per refractive index unit (nm/RIU) as a measure for the plasmonic sensitivity.

$$\text{IO} = \Delta\lambda_{\text{res}} / \Delta n \quad (4.1)$$

In general, the plasmon sensitivity is expected to increase for rods with more red or infrared resonances due to their large polarizability [Lee, 2006] – a trend observed in these measurements on solid gold nanorods with different resonance wavelength. The sensitivity of gold nanorods is in the range of  $\text{IO}=150\text{--}263$  nm/RIU, which is much larger than the values for solid gold spheres ( $\text{IO}=44$  nm/RIU), [Dmitriev, 2008] gold cubes ( $\text{IO}=83$  nm/RIU) [Dmitriev, 2008] and even larger than the value for spherical hollow gold nanoshells ( $\text{IO}=125$  nm/RIU). [Raschke, 2004] Indeed, we observe sensitivity values for rod-shaped gold nanorattles of up to  $\text{IO}=285$  nm/RIU (Figure 2b), which is also slightly higher compared to recently reported values for gold nanodisks supported on dielectric pillars. [Dmitriev, 2008]

The rod-shaped gold nanorattles produced combine both effects: a shell structure for high surface area and a rod-like shape for efficient light coupling. For some sensing application, not the plasmonic sensitivity, is important, but the

sensitivity in relationship to the plasmon linewidth (FWHM) – the figure of merit (FOM):

$$\text{FOM} = \text{IO} / \text{FWHM} \quad (4.2)$$

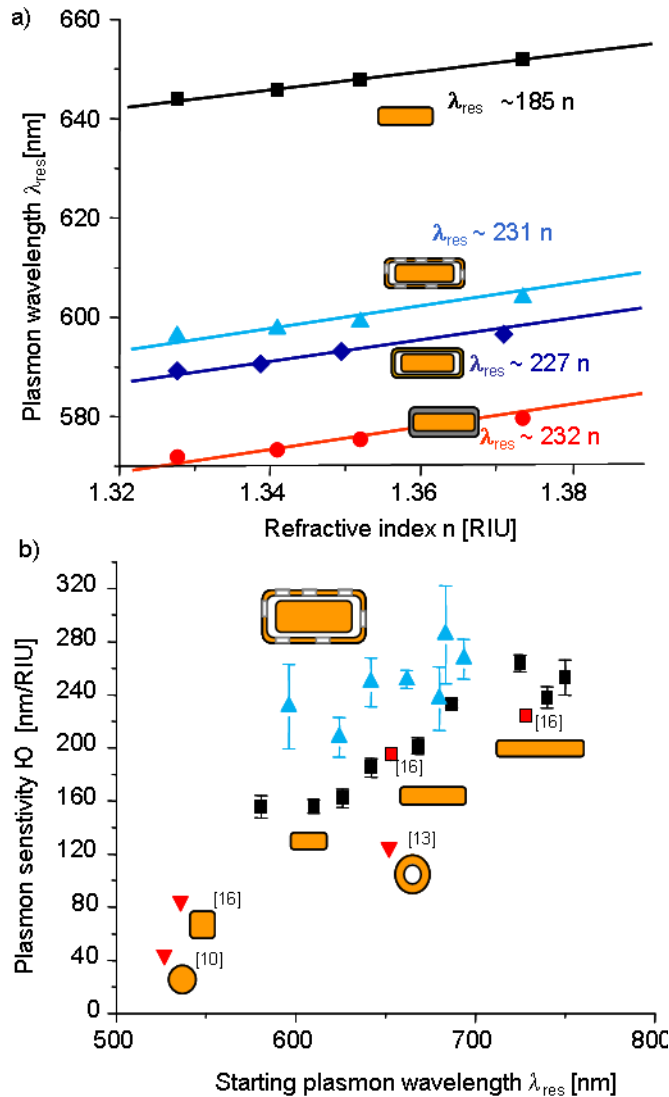


**Figure 4.7.** (a) Position of the longitudinal plasmon resonance peak vs. refractive index of the surrounding medium for gold nanorods, silver-coated nanorods and nanorattles (as indicated). The slope shows the different sensitivity towards changes in the dielectric environment, and we have indicated the proportionality constants  $\text{IO} = d\lambda_{\text{res}}/dn$  for these structures (b) Overview of the sensitivity IO of different gold nanostructures: spheres, cubes, rods, shells, and rod-shaped nanorattles. Since the sensitivity depends not only on shape but also on the position of the resonance wavelength, we show the sensitivity values as a function of the plasmon wavelength in water. The values for spheres, cubes, shells, and some rod samples are taken from the literature (reference numbers as indicated, red labels). Our data for ensemble measurements on different samples of solid gold nanorods (black labels) show lower IO values than rod-shaped gold nanorattles, produced from these rods (blue labels).

The FOM is an important parameter to characterize plasmon sensors if the resolution to detect plasmonic resonance shifts is limited by the resonance linewidth. We find the FOM values for the rod-shaped nanorattles in the range of 2.1 – 3.0 compared to 1.2 - 2.4 for the solid rods used for their synthesis (Figure

4.8 (a)). This increase in the FOM for the nanorattles reflects the increase in plasmonic sensitivity  $\text{IO}$  and almost unchanged plasmon linewidth of the sample after the hollow shell growth.

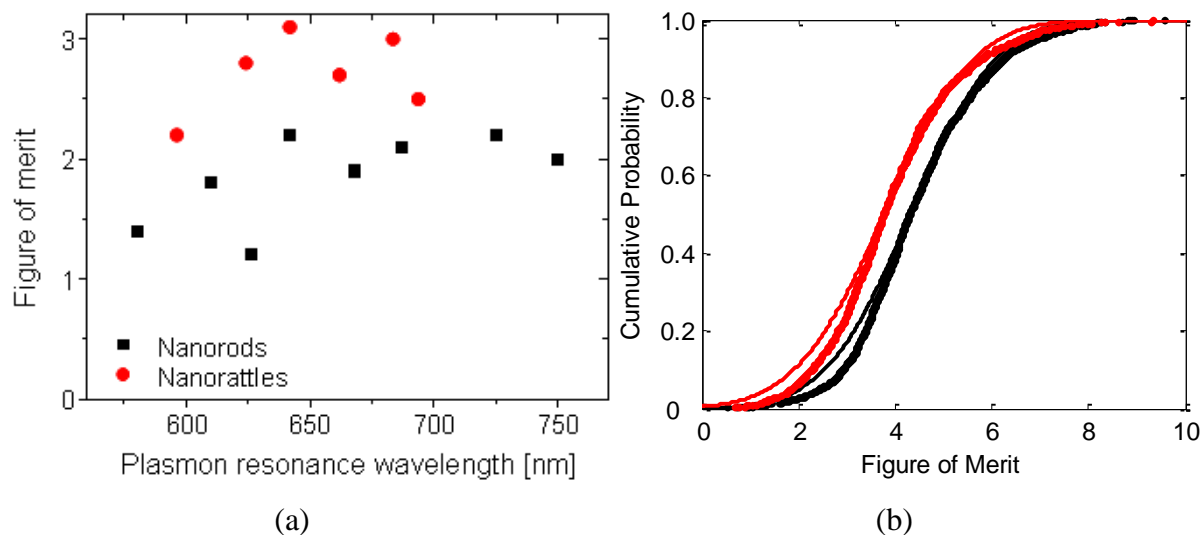


**Figure 4.8.** (a) Dependence of the figures of merit (FOM) from the plasmon resonance wavelength for the solutions of gold nanorods and rattles as indicated. (b) Cumulative probability distribution of the figure of merit derived from measuring single particle spectra of 1567 nanorods and 803 nanorattles. The median value is  $\text{FOM} = 4.3 \pm 1.4$  and  $\text{FOM} = 3.8 \pm 1.5$  for the rods (black) and cages (red), respectively. Although the rattles have a higher  $\lambda_{\text{res}}$  value compared to the rods (see Fig. 4.5), they show a smaller FOM value due to the larger FWHM as a result of the stronger plasmon damping in rattles, which increases the FWHM.

For practical use of nanorattles in plasmonic sensors, the sensitivity in a single particle sensor arrangement is of great importance, where the particles are supported by a substrate, which forms part of a microfluidic flow cell (Figure 4.9a).

The particles were immobilized on a glass substrate by rinsing a diluted solution for 2 min. through a flow-cell consisting of a thin, flat glass capillary (0.1 mm x 2 mm x 100 mm) connected to PET tubing. Particles attach randomly to the glass surface. When enough particles are in the field of view, their light scattering spectra are collected by fastSPS. [Becker, 2007]

The light scattered by single particles is then visualized in a dark-field microscope, where the particles appear as bright colored spots when illuminated by a white light source (Figure 4.6b). Single particle spectra are recorded by fast single particle spectroscopy (fastSPS)[*Becker, 2007*] based on a spatially addressable liquid crystal display used as an entrance to an imaging spectrometer. The fastSPS setup automatically records the spectra of about 50 – 100 single particles per measurement, which are initially immersed in distilled water. To measure the nanoparticle's sensitivity towards changes in the dielectric environment, we rinse it with solutions of different refractive indexes (sucrose ( $n=1.378$ ), ethylene-glycol ( $n=1.427$ ), or dimethylsulfoxide ( $n=1.4785$ )) and record the spectra of the previously investigated particles again. In several dozen experiments with different solvents, we investigate a total of 1567 solid gold nanorods and 803 nanorattles. The median sensitivity IO of solid gold rods was  $IO_{\text{rods}} = 169 \pm 51 \text{ nm/RIU}$  and for nanorattles  $IO_{\text{rattles}} = 199 \pm 70 \text{ nm/RIU}$  (Figure 4.9c).

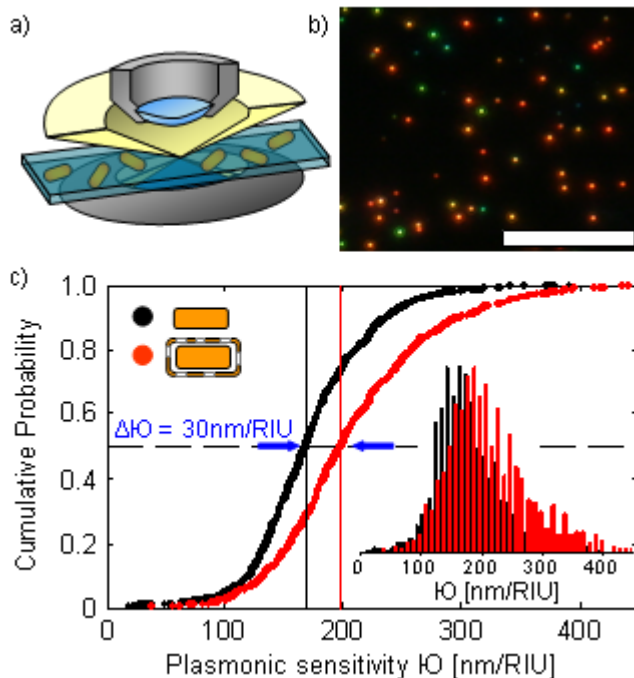


**Figure 4.9.** (a) Schematics of the dark-field microscope setup. The illumination passes by the objective, while only the scattered light of the particles is collected and directed to an imaging spectrometer, where the spectrum is captured by a CCD camera. (b) Real color dark-field image of nano-rattles, each bright spot represents one single particle (scalebar 25  $\mu\text{m}$ ) (c) Cumulative probability distribution of the plasmon sensitivities derived from measuring single particle spectra of 1567 nanorods and 803 nanorattles. The median plasmon sensitivity is  $IO = 167 \pm 51 \text{ nm/RIU}$  and  $IO = 199 \pm 70 \text{ nm/RIU}$  for the rods (black) and cages (red), respectively. The inset shows the corresponding normalized histograms.

The relatively large standard deviations in those values are caused both by large interparticle deviations within the same experiment as well as systematic deviations between subsequent experiments with new flow cells, particles and solvents. Whereas the deviations between particles is expected from the polydispersity of the particles and points towards further chances for improvements, the large deviations in-between subsequent experimental runs is puzzling. We have not identified the factor causing these deviations but collected sufficiently high statistics to report precise mean sensitivities (Student's t-test proves significantly higher plasmon sensitivity of nanorattles compared to solid nanorods with >99.999% probability). However, previous reports for plasmonic sensitivity with fewer statistics have probably overlooked this variation and should be regarded with some caution. Further study of these unexplained variations in plasmonic sensitivity, which is independent of the type of particle under investigation, is clearly required but may require ultra-clean working environments. The single particle measurements yielded slightly higher FOM for the solid rods ( $4.3 \pm 1.4$ ) compared to the rattles ( $3.8 \pm 1.5$ ) (Figure 4.8b.), caused by the slightly stronger plasmon damping in rattles which increases the linewidth.

### **4.3. Increased Catalytic activity of nanorattles**

The rod-shaped gold nanorattles have two more beneficial properties for applications: chemical stability and enhanced catalytic activity due to their large surface area. The chemical stability against dissolution and oxidation in aqueous environment is required for plasmonic sensing applications for biological species. Silver-coated gold nanorods, for example, show similar plasmonic sensitivity values at visible wavelength (Figure 4.5 a ) but are not stable in aqueous environment over timescales of days (Figure 4.9).

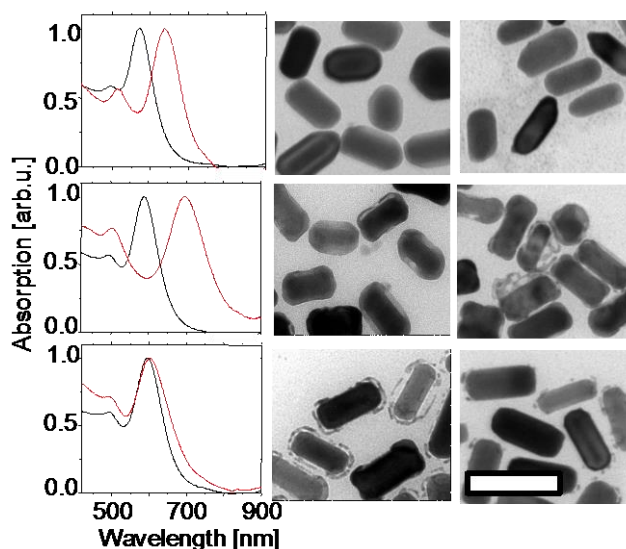
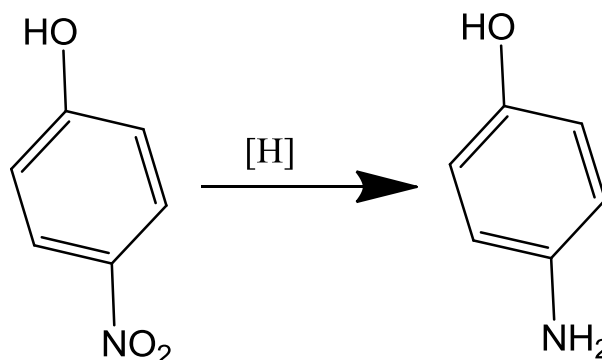


**Figure 4.9.** Stability of silver-coated particles, closed and porous nanorattles in aqueous media. Spectra (left column) and TEM images of freshly prepared (middle) and aged particles (right). Black plots - the freshly prepared particles and red – particles after aging for 21 days. Silver coated rods (upper row), nanorattles with closed outer shell (middle row), and the porous gold nanorattles (bottom row). It is clear that porous nanorattles maintain their resonance wavelength better than closed ones and silver coated rods. Scalebar is 50 nm.

The large surface area of nanorattles, which makes them very sensitive to changes in the dielectric environment, should also enhance their catalytic activity compared to solid gold nanorods.

To demonstrate this enhanced catalytic activity, we use the reduction of para-nitrophenol to para-aminophenol by sodium borohydride.



Typically 9 mL of  $3.7 \cdot 10^{-4}$  M *p*-nitrophenol (spectrophotometric grade, Sigma) was added to 1 mL of 1.2 M  $\text{NaBH}_4$  (99%, Aldrich) aqueous solution, and

the mixture was stirred for 10 min at room temperature. 40  $\mu\text{L}$  of an aqueous particle suspension (gold nanorods, Au or Pd nanorattles, concentrations appr.  $3 \cdot 10^{10}$  particles/ml) was added to the mixture. The reaction progress was being checked continuously (every 10 s) by recording optical absorption spectra with a fiber spectrometer until the deep yellow solution became colorless.

It is known that this reaction is catalyzed by some metals including gold [Lee, 2008] and an absorption peak at 420 nm provides an easy way to monitor the reaction spectroscopically. Indeed, we observe a very slow decrease of the nitrophenol absorption for the control experiment without addition of nanoparticles (Figure 4.10).

Adding solid gold nanorods increases the reaction significantly and all nitrophenol is reduced in about 2000 sec. Adding the same number of rod-shaped gold nanorattles further increases the reaction speed by a factor of 3 - 4. Simple geometrical estimation using average dimension parameters determined from TEM images yields a four times increase in surface area (Figure 4.4)., which agrees well with kinetic rate increase (Figure 4.10).

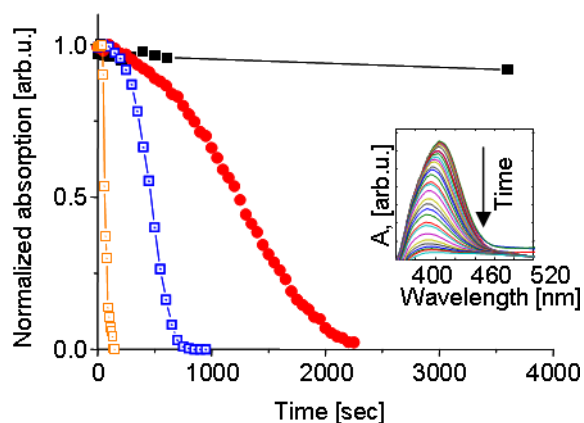


**Figure 4.10.** a) Normalized absorption at the peak position of para-nitrophenol as a function of time after the addition of sodium borohydride (black curve). The concentration of para-nitrophenol decreases only slowly over time. The presence of metal nanoparticles acting as catalysts significantly increases the reaction rate. The same number of Au-rattles (blue) is more active than nanorods (red). Replacing the outer gold shell in the nanorattles with a thin Pd shell

further increases the catalytic activity (orange). The development of the absorption spectra over time is shown in the inset.

Rattles with palladium cage increase the reaction speed by another factor of 4 due to the well known larger catalytic activity of Pd versus Au in studied reaction.[*Esumi, 2004*]

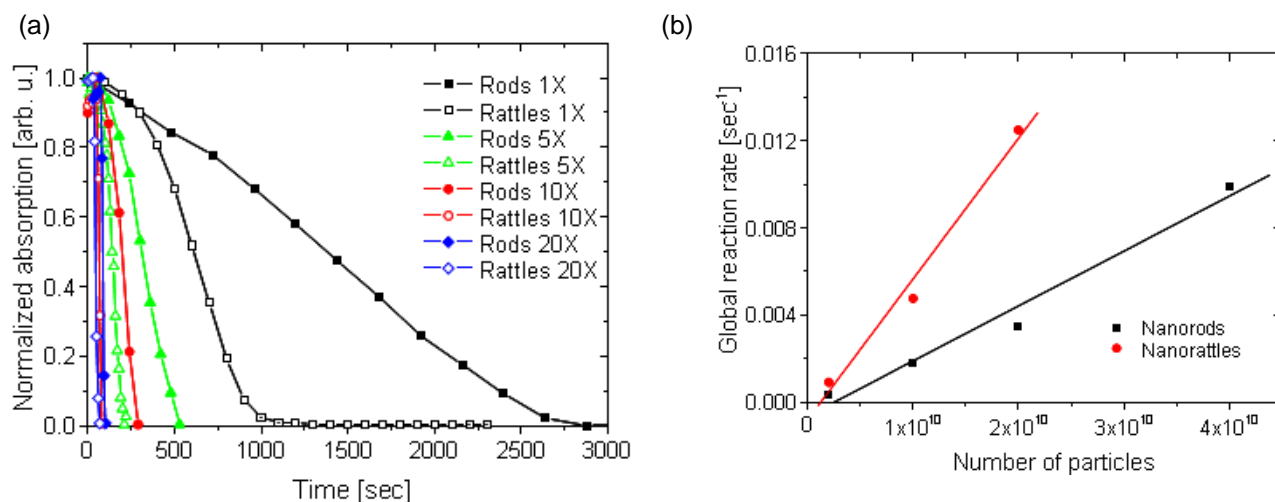


Figure 4.9. (a) Normalized absorption at the peak position of para-nitrophenol- $\text{NaBH}_4$  as a function of time after adding different amounts of catalyst. The number of particles shown here as 1X is approx.  $2 \cdot 10^9$ . Z-shape of kinetic curve caused likely by the consecutive nature of this reaction: first sodium borohydride is decomposed on the surface of nanoparticles producing H-atoms, which then react with p-nitrophenol-molecules. (b) Dependence of catalytic activity of gold nanorods and nanorattles on the number of particles added to the reaction mixture. Lines are linear fits. The increase of the reaction rate is in good agreement with an Eley-Rideal mechanism for heterogeneous reactions. This mechanism proposes that only one of the reactants (in our case H-atoms) adsorbs on the surface of the catalyst, and the global reaction rate depends linearly on the total number of active sites or particle concentration.

The shape of the catalytic reduction curve has three regions. At the beginning, the reaction is slow because first sodium borohydride has to be decomposed on the surface of nanoparticles producing H-atoms, which are then available to p-nitrophenol-molecules. When the concentration of hydrogen on the surface is maximal, the reaction reaches its highest rate and slows down only when reactants are consumed at the end of the reaction. We find a linear increase

of the reaction rate with particle concentration (Figure 4.9 b). The Eley-Rideal mechanism of heterogeneous reactions, which assumes that only one of the reactants (in our case hydrogen) adsorbs on the surface of the catalyst, can explain the observed reaction rate dependencies.

### **Conclusions**

The rod-shaped gold nanorattles show beneficial properties when compared to solid gold nanorods: their plasmon resonance shows greater sensitivity to changes in the dielectric environment and they show larger catalytic activity than solid gold nanorods. Furthermore, these particles are stable in aqueous solution for days, in contrast to silver-coated gold nanorods. They are therefore promising candidates for optimized plasmonic binding sensors, detecting changes in the local dielectric environment and for applications requiring the combination of catalytic activity and plasmonic sensing.

## 5 Selective gold deposition on CdTe hyperbranched nanomaterials\*

Hyperbranched CdTe nanoparticles are among the structures with the most complex three-dimensional shapes – varying from very delicate spider-net like networks to very compact urchin like particles.[*Kanaras, 2005*] Similar particles have already found application in organic-inorganic blend materials for solar cells.[*Gur, 2007*] Creating devices from inorganic nanocrystals often requires to assemble them in well-defined geometries and orientations at specific locations on surfaces, as well as arranging different types of nanocrystals into unique hybrid structures.[*Cozzoli, 2005*] The creation of hybrid metal-semiconductor nanostructures is an important next step towards such self-assembled functional structures.[*Cozzoli, 2006*] Recently, there has been success in growing metal tips on tetrapods and on one or both tips of rod-shaped CdSe and CdS particles, mainly by the Banin group[*Mokari, 2004;Mokari, 2005;Steiner, 2005;Mokari, 2006;Saunders, 2006*]. They demonstrated the possibility to use these metal tips as direct electrical contacts point and as assembling and reaction centers.[*Steiner, 2005;Carbone, 2006;Carbone, 2006;Salant, 2006*] There is also a considerable interplay between the optical and electronic behavior of the components of such hybrid materials, potentially leading to enhanced or new properties. For instance, enhanced conductivity has been recently demonstrated for such structures.[*Sheldon, 2009*]

---

\* A version of this chapter was published as **Khalavka, Y.**; Sonnichsen, C. *Advanced Materials* **2008**, *20*, 588 *Growth of gold tips onto hyperbranched CdTe nanostructures.* and highlighted in Nature

### 5.1. Sacrificial growth of Gold on CdTe

Hyperbranched CdTe nanostructures were synthesized according to the procedure described in Appendix A. The metal tips were added to the hyperbranched particles at room temperature (in the open air) by mixing with a gold growth solution containing  $\text{HAuCl}_4$ , dodecylamine (DDA) and didodecyldiamine-ammonium bromide (DDAB) in toluene – the tips of the hyperbranched particles acting as nucleation centers for the gold growth. The molar ratio between the gold growth solution and the CdTe hyperbranched particles controls the amount of gold deposited on the substrates. Our choice of solvent is essential for the success of the reaction.

The growth of gold onto the hyperbranched CdTe particles by transmission electron microscopy (TEM) before and after addition of the gold growth solution (Figure 5.1) was analyzed by me. Figure 5.1a shows an image of the original CdTe hyperbranched nanoparticles which were used as substrates. They have an average branch thickness of  $5.3 \pm 1.1$  nm. After the addition of the gold growth solution, metallic gold appeared selectively at the tips of the hyperbranched CdTe-particles. The gold is well distinguished from the semiconductor material by the higher contrast and appears as a local increasing of diameter of the ‘blobs’. (Figure.5.1 b-d).

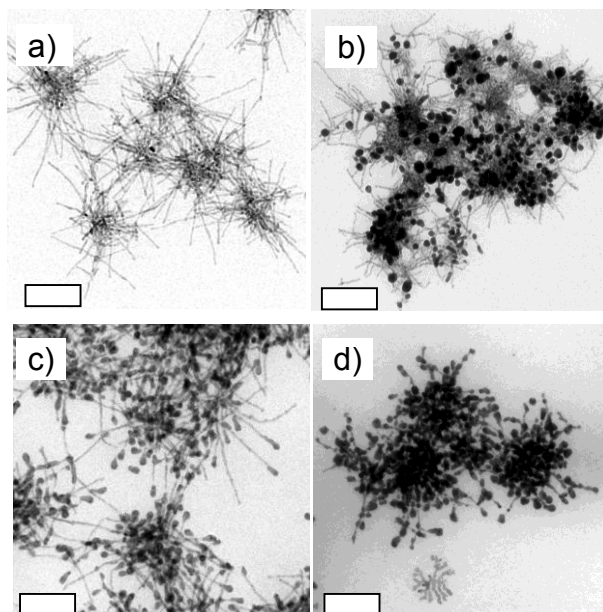


**Figure 5.1.** TEM images showing growth of gold onto the tips of hyperbranched particles. (a) CdTe hyperbranched nanoparticles as prepared. (b-d) hybrid (gold on CdTe) structures grown on the particles in (a) with molar ratios of the CdTe:gold of (b) 1:0.5, (c) 1:1 and (d) 1:2. Changes from some tips covered by gold (b) to nonselective growth (d) are visible. (Scalebars 100 nm)

Increasing the volume of gold growth solution added to a fixed volume of CdTe particle suspension leads to an increase in the number of tips showing gold coating (Fig 1b, c) and eventually to gold growing also on defects at the sides of the branches (Fig 1d). The gold tips have a narrow size distribution (average diameter of  $12.7 \pm 2.5$  nm).

The CdTe branches keep their average thickness after the reaction. In contrast to the finding for CdSe rods [Mokari, 2004], there seems to be no significant etching of the CdTe material in presence of DDAB and DDA mixture, at least during applied reaction times.

The reaction rate (13 nm gold in 5 min) is much faster than what Saunders *et al* [Saunders, 2006] observed for gold grown on CdS rods (2.3 nm in 90 min). The reason is probably the higher reactivity of CdTe nanoparticles due to the lower reduction potential of  $\text{Te}^{2-}$  ion (-1,14 V), in comparison to  $\text{S}^{2-}$  (-0,48 V) and  $\text{Se}^{2-}$  (-0,92 V) [Lide, 2004]. High-resolution electron microscopy (HREM) reveals a non-epitaxial growth of gold and the formation of a multigrain structure in the gold tips (Figure 5.2). The latter is likely due to the high rate of Au deposition and the strain from the lattice mismatch.

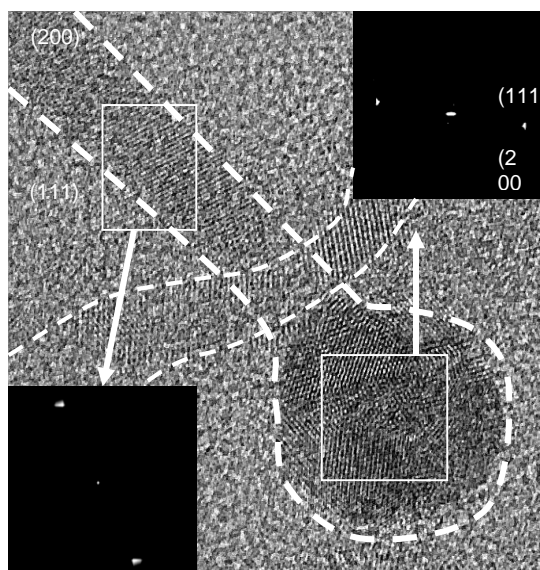
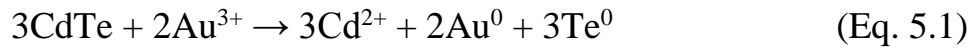


**Figure 5.2.** HRTEM image of a gold coated tip of a CdTe branch. The white lines are guide to the eye outlining the branch (and a crossing CdTe branch). Insets show the Fourier transformation of the areas indicated. The CdTe lattice along the branch corresponds to the (110) planes of CdTe. The multigrain-structure of the gold tip leads to a smearing out of the Fourier transformed image, but peaks corresponding to the Au (111) and (200) plane can be identified. Scalebar is 10 nm

Deposition of gold contacts on the semiconductors like CdTe is well known and widely used procedure for bulk samples. But the mechanism of metallic Au deposition on semi-conducting particles has not been explained fully. Without the surfactant DDA, gold is still deposited but there is a fast precipitation of nanocrystals[Carbone, 2006;Carbone, 2006]. Hence, the amine group is not needed as reducing agent but probably slows the reaction by formation of a complex with Au(I), which is more stable to reduction than pure Au(I) in solution[Gomez, 2000]. Replacing DDAB with cetyl-trimethyl-ammonium bromide (CTAB), which is widely used for stabilizing gold nanoparticles[Perez-Juste, 2005], leads to uncontrolled growth of gold and destruction of the substrate. We found that pure gold growth solution, without adding CdTe particles, forms small gold colloids with an average diameter less than 5 nm. Here, the mechanism is likely a reduction of gold salt to an Au(I) complex with toluene, and then the slow decomposition of this complex to metallic gold under open-air conditions.[Gomez, 2000] However, the considerably larger diameters of gold tips on CdTe particles hints at a strong role of CdTe in the reduction process and follows probably a route similar to that proposed by Carbone et al.[Carbone, 2006]:



The reduced Au atoms deposit on the tips at the ends of CdTe branches. The oxidation of CdTe produces  $\text{Te}^0$  atoms forming a layer on the surface of the CdTe particles, and  $\text{Cd}^{2+}$  ions, which may go into solution. Elemental analysis using energy dispersive X-ray spectroscopy (EDX) confirmed this mechanism by finding a significantly higher Te: Cd ratio after the reaction than before (Table 5.1).

EDX was performed in STEM mode with spatial resolution of about 10 nm and has the unique advantage to give local composition information (in contrast to ensemble techniques such as ICP-MS). Since we often have a mixture of unreacted substrate, gold-tipped particles and pure gold particles in the solution, the local composition analysis gives valuable information. Before the reaction, the Te: Cd ratio is 1:1.4 throughout the particles – in agreement with some surface enrichment with Cd atoms [Carbone, 2006]. After the reaction, we find more Te than Cd on the particles as expected from (1). It is also evident from the data shown in Table 5. 1 that the tips consist of pure gold.

Table 5.1. Elemental composition of the CdTe particles before the reaction and after the reaction as determined by local EDX measured at the center (core) of the hybrid particle and at the tip. Values are averages of 20 separate particles.

(in at. %)	Cd	Te	Au
Initial	58±3	42±3	-
Hybrid:	10±6	21±6	67±3
	1±.3	3±2	96±3

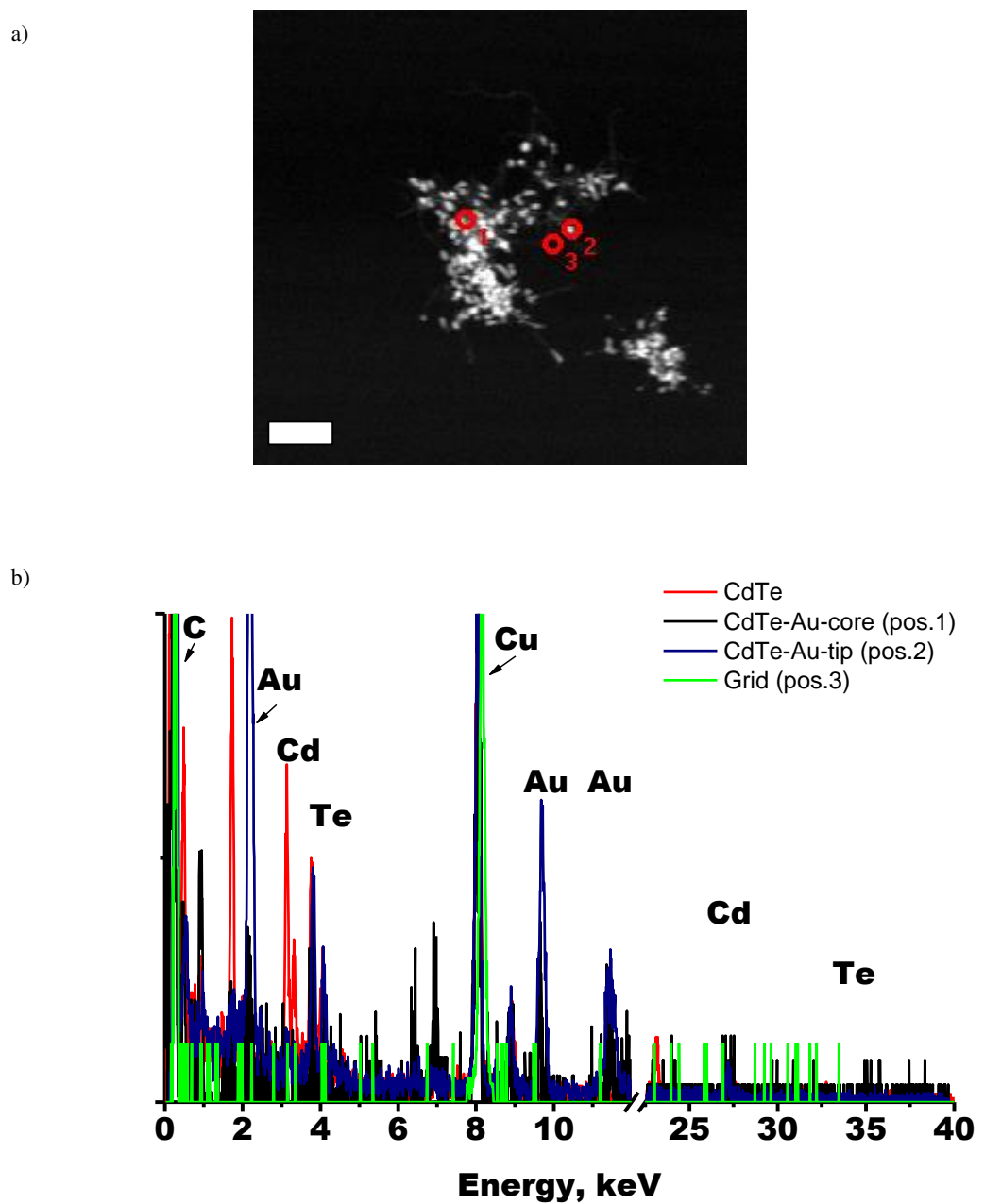


**Figure 5.3.** (a) Scanning TEM image showing location of EDX measurements. Scalebar is 100 nm. (b) Comparison of EDX spectra of hybrid structures, the original CdTe particles and pure TEM substrate (carbon coated copper grid). The Au peaks is clearly visible for hybrid particles.

## 5.2. Characterization of hybrid structures

The gold reduction mechanism proposed above uses up material of the particle and should lead to a measurable reduction of the CdTe particle volume. We checked this expected shortening of the branches in a control experiment on hyperbranched particles with very few long branches, which lay flat on the TEM substrate and allow for straight forward length estimation (Fig. 5.4a). Indeed, we observe a decrease of the mean length of the CdTe branches (thickness  $9.9 \pm 2.4$  nm) from  $182 \pm 29$  nm to  $104 \pm 42$  nm (Fig 5.4c). Using the bulk densities, we estimate the number of Te atoms  $n_{\text{Te}}$  in the volume of CdTe material lost to  $n_{\text{Te}} = (9 \pm 6) \times 10^5$ . This is roughly  $2/3$  of the number of gold atoms  $n_{\text{Au}}$  per tip expected from (Eq. 5.1), which we estimate from the tip size ( $14.7 \pm 2.38$  nm) to  $n_{\text{Au}} = (9 \pm 3) \times 10^5$ .

This also explains why it is difficult to control the growth of the gold. The reason for this is usually high reactivity of CdTe with gold solutions. If the reaction is performed at high concentrations of gold acid or in any other uncontrolled way it leads to the total decomposition of the CdTe. Indeed, when I have used CdTe rods long enough and this reaction protocol, it was also possible to synthesize also hybrid nanostructures of match-stick geometry. (Figure 5.5).

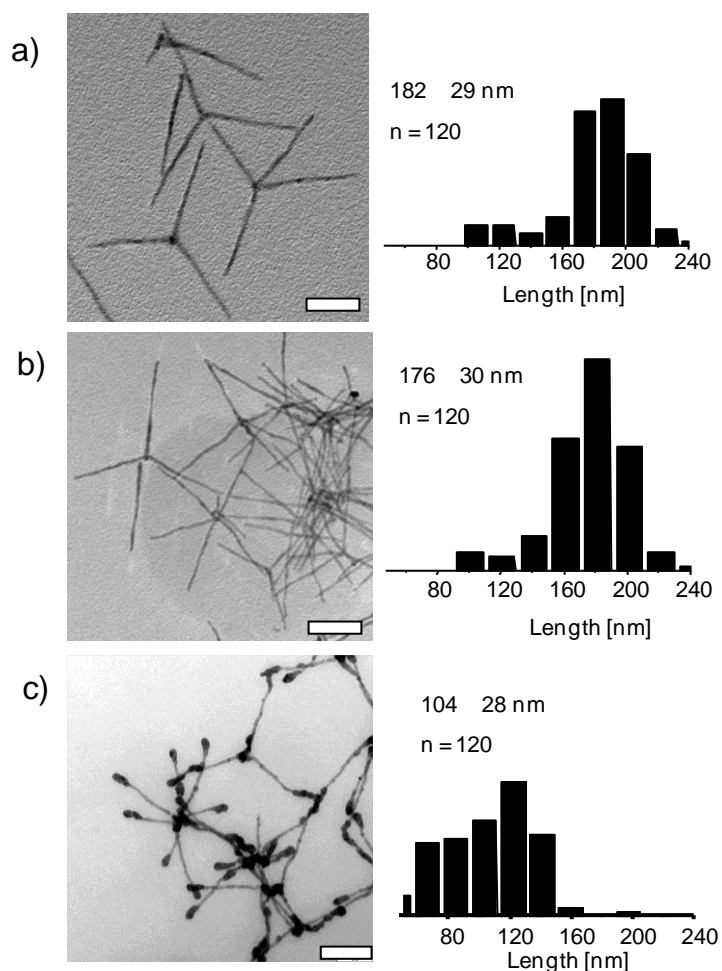


**Figure 5.4.** (a) TEM image of CdTe particles with a small degree of branching used to measure substrate etching on gold deposition – together with a histogram of arm length counted on 120 particles. (b) Particles of the same batch, 5 min after addition of DDA and DDAB showing virtually no etching. (c) Particles after growth of gold on the tip, where the mean branch length is significantly shorter (all scalebars are 100 nm).

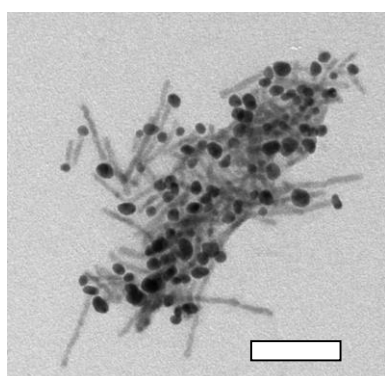


**Figure 5.5.** TEM image showing gold tips grown on CdTe nanorods. Scale bar is 50 nm.

The reduction of gold by DDA and toluene seems to occur in parallel to the mechanism discussed above since I also found small gold colloids similar

to those obtained from CdTe-free solutions in some of samples of hybrid particles (Figure 5.6.). However, the clear and almost quantitative CdTe particle dissolution, the reaction kinetics and the local EDX measurements together confirm the gold reduction by CdTe oxidation as the predominant mechanism. From experiments in different solvents it is evident that the kinetic balance is critical. Only choice of chloroform for the CdTe particles and toluene for the gold growth solution leads to intact hybrid structures.

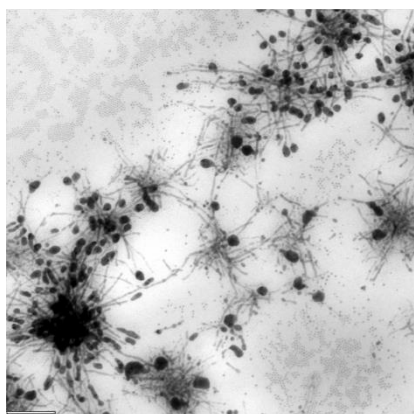


**Figure 5.6.** TEM Images showing small gold colloids near hybrid gold-CdTe particles. This observation confirms that the two reduction processes discussed in the text are both occurring in parallel. Scalebars are 100 nm

The etching of CdTe also leads to a significant flattening of the three-dimensional structure of the hyperbranched particles after reaction with the gold solution and deposition on the TEM substrates. We use the method of TEM tomography to reconstruct the 3-dimensional particle shape from a tilt series of TEM images (Figure 5.7.).

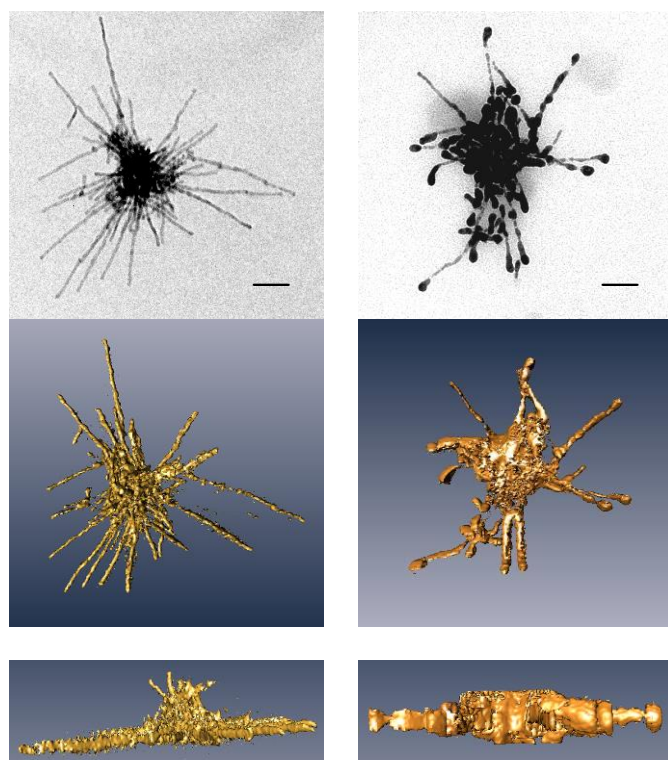


**Figure 5.7.** TEM images (scalebars 100 nm) and 3-dimensional reconstructions of the original CdTe nanoparticles before the reaction (left column) and of the gold-CdTe hybrid structures after reaction (right column). The central row shows the three-dimensional reconstruction from a top-view in the same orientation than the TEM image in the top row. The bottom row shows the three-dimensional reconstruction from a side view. A considerable flattening of the overall structures after reaction is clearly visible.

The capillary forces acting on the particles as the solvent evaporates considerably flatten the presumably more or less spherical hyperbranched particles. Before the reaction with gold, the particles still show tips pointing upwards, but after gold is deposited on the tips, the structures are almost entirely flat after drying. Since the weight of the gold tips is clearly not enough to bend the arms, the observed flattening is due to a weakening of the particle structure due to the above-mentioned etching process. The 3D reconstructions also allow estimating the volume filling factors of the hyperbranched particles, which are in the order of 0.1–1%.

## Conclusions

In conclusion, I have prepared and analyzed a novel type of hybrid metal-semiconductor Au-CdTe nanostructures with complex shapes, enormously large surface to volume ratio and well defined evenly sized gold anchor points at the tips. The importance of reaction of CdTe with gold salt was proven. The proposed procedure may give rise to a new class of multifunctional materials, in particular in combination with organic molecules, with possible application for example in energy conversion devices, bio-functionalized materials, and infrared emitting/detecting devices.

## 6 Photoreduction of Au on rodshaped semiconductor in Chloroform\*

Metal-semiconductor hybrid nanocrystals offer potential opportunities for solar energy conversion [Kamat, 2008] and photo-catalysis. [Subramanian, 2004] Their nanoscopic dimension alters the electronic and optical properties via the quantum confinement effect in the semiconducting part (leading to a size tunable band-gap [Alivisatos, 1996]) and via the electrodynamic confinement ('plasmon') in the metal part (leading to a very high polarizability at the plasmon frequency [Eustis, 2006]). Potentially, the plasmonic 'antenna-effect' could amplify the excitation or radiative decay of excitons in the semiconductor. [Buonsanti, 2006; Fedutik, 2007] Charges generated by the excitation of the semiconducting part can be transferred to the metal part shifting the plasmon frequency [Wood, 2001; Hirakawa, 2004] [Mulvaney, 1996] and/or promoting redox reactions. [Subramanian, 2004; Costi, 2008; Elmaleh, 2008]

Until now, it has not been possible to control the metal size in those systems. The gold domains were typically in the order of  $\leq 2.0$  nm in diameter when reacting with CdS nanorods in anaerobic condition and eventually just overcame 10 nm when ripened for 3 days in the presence of oxygen for nanorods longer than 50 nm. [Saunders, 2006] Since plasmons in gold nanoparticles are strongly damped for particle diameters below 10-20 nm by surface scattering [Pinchuk, 2004; Hu, 2008] and the size dependent d-band-Fermi-level offset [Phala, 2007],

---

\* The results described in this chapter were published as Carbone, L.; Jakab, A.; **Khalavka, Y.**; Sonnichsen, C. *Nano Letters* **2009**, 9, 3710  
*Light-Controlled One-Sided Growth of Large Plasmonic Gold Domains on Quantum Rods Observed on the Single Particle Level.* and  
Carbone, L.; Jakab, A.; **Khalavka, Y.**; Sonnichsen, C. SPIE: San Francisco, California, USA, 2010; Vol. 7575, pp 757505.

the poorly understood interaction between plasmons and excitons could not be studied in detail in such hybrid particles.

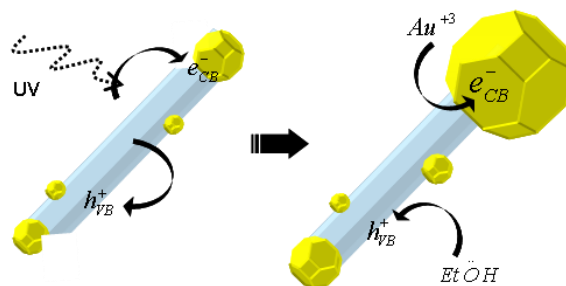


**Figure 6.1.** Sketch of the mechanism for photo-induced growth of large gold domains (yellow) on semiconductor CdS nanorods (light blue).

In recent years, great advances have been made toward designing the controlled growth of small Au crystals selectively on the tips of CdSe and CdS rod-shaped nanocrystals, where the metal is in direct crystallographic contact with the semiconductor part.[*Cozzoli, 2006;Saunders, 2006*] These structures underwent a change from two-sided (dumbbells) to one-sided (matchstick) growth attributed to intra-particle electrochemical Ostwald-ripening where the smaller metal domains are dissolved in favor of the larger tip.[*Mokari, 2005;Mokari, 2006*] The gold tips on the semiconductor rods can both serve as anchoring points for self-assembly[*Salant, 2006;Figuerola, 2009;Figuerola, 2010*] and accumulate electrons photogenerated in the semiconductor to drive redox reactions.[*Cozzoli, 2005;Costi, 2008*]

In this chapter a strategy for creating large gold domains of controlled size (up to 15 nm) on CdS or CdSe/CdS quantum rods through the photo-reduction of gold ions is described. The metal deposition is promoted and controlled by UV light irradiation under anaerobic conditions. The large gold domain supports efficient plasmon oscillations with a light scattering cross section large enough to

visualize single hybrid particles in a dark-field microscope during the particle growth in real time (see Figure 6.1).

Most of the results described in this chapter are result of experiments performed together with Dr. Luigi Carbone. My part was TEM-characterization, tomography and growth monitoring in situ with optical absorption measurements. Single particle measurements where performed with Dr. Arpad Jakab.

### **6.1. Photo-induced Au reduction on semiconductor rods.**

The photocatalysis experiments are performed under Ar atmosphere (glovebox) using dry solvents. A volume of 1 ml of a chloroform based solution of the substrate particle sample is added to a glass vial at a concentration of  $2.5 \cdot 10^{-7}$  M. We use either CdS/CdS rods, CdSe/CdS rods, or Au-CdSe/CdS-Au nanodumbbells as substrates. Afterwards, 400  $\mu$ L of dry EtOH is slowly added (for a final ratio of 10:90 v/v to chloroform). Keeping the ethanol concentration below 10% prevents precipitation of the hydrophobic nanoparticles. Finally, we inject (dropwise) 3 ml of a chloroform based Au solution (9 mg  $\text{HAuCl}_4 \cdot 3\text{H}_2\text{O}$ ) containing the surfactants DDA (70 mg) and DDABr (42 mg). Afterward every semiconductor solution is UV irradiated using an ordinary UV-lamp (wavelength 366 nm, 2-3  $\text{mW}/\text{cm}^2$ ) in the darkness while stirring. The sample is allowed to grow under UV irradiation for up to 120 min with aliquots withdrawn at scheduled times. Finally, the growth reaction is stopped by interrupting the irradiation, precipitating the sample with acetone, applying 10 min of centrifugation at 1300 g, drying, and re-suspending the precipitate in chloroform. Depending on the dilution, the final sample appears dark or pale violet. In order to rule out any light absorbance of the glass vial for the UV irradiation (366 nm), a few control experiments with identical results were performed in a quartz cuvette. The resulting gold-tipped nanorods are shown in Figure 6.2d-f together with the

starting material (CdS/CdS rods, CdSe/CdS rods, or Au-CdSe/CdS-Au nanodumbbells Figure 6.2a-c) and the resulting nanoparticles in a parallel control experiment without UV irradiation Figure 6.2g-i. Without UV irradiation, only small domains form, with particles often sharing one gold domain and creating network-like structures in the case of nanodumbbells as starting material.

First, CdS and CdSe(core)/CdS(shell) nanorods were prepared using the seeded growth method (Figure 6.2a,b respectively). This method produces rods with narrow size distribution. In addition, gold tipped CdSe/CdS dumbbells were grown (see Figure 6.2c) using the CdSe(core)/CdS(shell) nanorods depicted in Figure 6.2b as starting material. Large gold domains form selectively on one side of each semiconductor rod exclusively under UV irradiation (Figure 6.2d-f). There is only one large gold domain per semiconductor rod regardless whether a CdSe seed is present in the CdS rods or whether there are preformed gold domains on *both* tips (Figure 6.2). Control experiments without UV light (Figure 2g-i), without EtOH (Figure 6.3a), without semiconductor rods (Figure 3c), or with UV irradiation before Au injection (Figure 6.3b) showed no large gold domain formation confirming the importance of each component and reaction step.

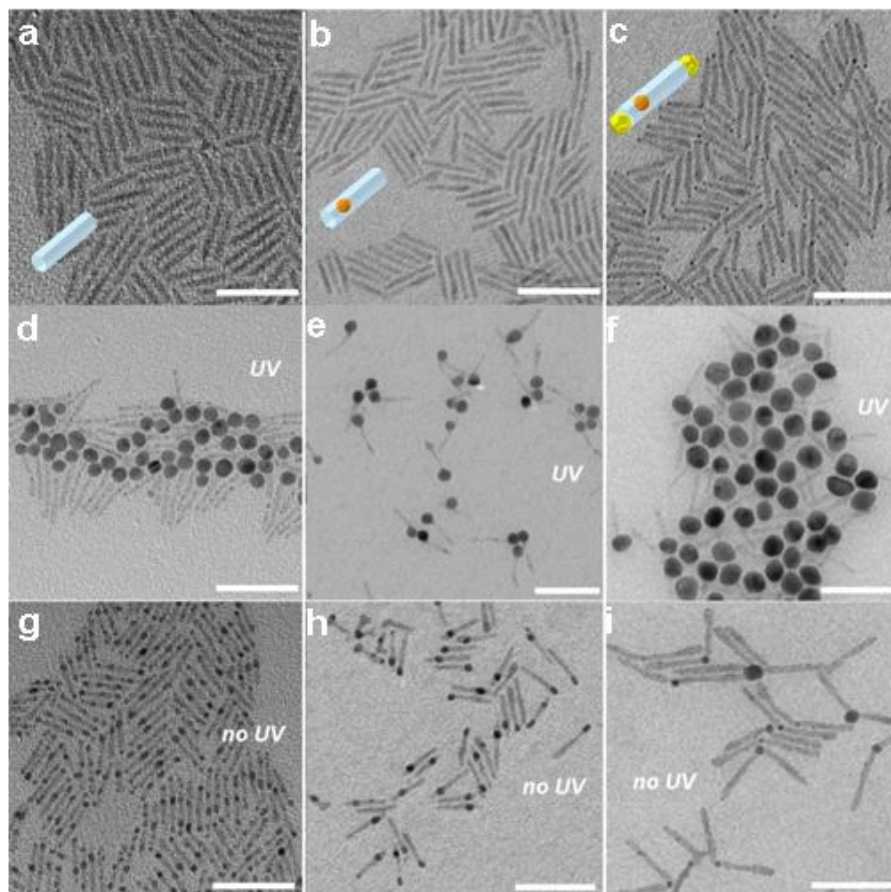


**Figure 6.2.** The strategy of depositing gold with light driven reduction works just as well for all investigated starting materials (a-c): pure CdS rods (length  $32.9 \pm 4.8$  nm; diameter  $4.0 \pm 0.5$  nm) (left column), CdSe(seed)/CdS(shell) (length  $28 \pm 2$  nm; diameter  $3.8 \pm 0.4$  nm) rods (middle column), and Au-CdSe/CdS-Au dumbbells (right column). After 60 min of UV irradiation, each particle forms exactly one large gold domain at one end, irrespective of the starting material (d-f). After the same amount of time without UV irradiation, only small gold islands form (g-i). (All scale bars 50 nm)

We propose a model based on the mechanism shown in Figure 1 to explain the observed gold domain formation. After a few drops of  $\text{Au}^{+3}$  ions are injected, small gold domains form instantly on the sides and at the tips of the semiconductor rods without need of UV light excitation. Since the photocatalysed one-sided growth also occurs on preformed dumbbells (Figure 6.2c), they are likely an

intermediate structure at this point. Upon UV stimulation, the electron ( $e^-$ ) created in the semiconductor migrates preferentially to one metal tip reducing further  $Au^{+3}$  ions, whereas the correlated hole ( $h^+$ ) is reduced by the solvent. The efficiency of carrier separation is further improved by organic electron donors present in the reaction mixture like EtOH,  $CHCl_3$  and even  $Br^-$  which can (in de-aerated systems) scavenge the valence band holes. Supporting the proposed mechanism, we find no large gold domain growth when exciting pure CdS rods with an energy smaller than the band-gap of CdS (2.21 eV or 562 nm, Figure 6.2d and f). It is interesting to observe that no gold domain formation when CdSe/CdS nanorods are excited at 562 nm (enough to excite the CdSe core) indicating that the electrons created within the CdSe core remain confined and are not able to transfer to the gold domain (Figure 6.2d-e).

The model above explains the photo-induced gold-domain formation, but it does not explain why only one out of several initially formed small gold domains grows larger. An earlier explanation for one-sided Au growth (observed in experiments without light excitation over long time periods) proposed an electrochemical ripening process: a gold atom returns to the solution as a positive ion, the remaining electron transfers via the semiconductor rod to another gold domain where it is able to reduce a gold ion. The electron transfer along the particle greatly enhances the ripening speed.

However, the switch from two-sided to one-sided gold domains is much faster in our case than the previously observed ripening process that took place over the course of days. There is also no evidence for the dissolution of small gold domains. We believe a different mechanism is in place in our case: one of the initially formed gold domains, usually at the tip, attracts the vast majority of the photo-electrons reducing gold ions from solution. Since the selective drift of

electrons to one domain does not involve any oxidation of gold atoms, our mechanism is not a ripening process. The question is, how does one gold domain attract all the electrons or majority of gold reduction? It could be due to a lower barrier to the semiconductor (less passivated interface), a lower surface tension, a higher electrical capacity, or a combination of these factors. Another force driving electrons mainly in one direction might be the influence of the intrinsic electrical dipole moment of the binary II-VI nanocrystals or a preferential crystal matching between gold and certain CdS facets. In our opinion it is favorable for the electrons to end up in the largest gold domain due to its higher electrical capacity but this point should be subject to further investigation.

Electron microscopy provides extra details of the growth process. High resolution TEM images show the crystalline nature of the entire hybrid particle (Figure 6.3a). The CdS wurtzite lattice is preserved and the large gold domain typically shows pentagonal twinning (Figure 6.3a). There are very small gold domains at irregular intervals and at the second tip (Figure 6.3c) which form at rod surface defects or defects in the surfactant layer.

We also observe a non-symmetric attachment of the gold domains to the CdS rod on TEM tomographic reconstructions from low-resolution TEM images (Figure 6.3b). The particles do not actually resemble nano-‘matchsticks’ but rather nano-‘smoking pipes’. The asymmetry could result from a preferential crystallographic interface between the (111) facets of the penta-twinned gold crystal and the (101) facet of the CdS rod. The asymmetric attachment of the gold domain slightly shortens the apparent semiconductor rod length under some viewing angles, which may be wrongly ascribed to a rod etching. In this context, UV-induced growth experiments carried out on very short nanorods showed no significant etching of the semiconductor (images not shown).

As an example, a statistical analysis of the gold domain diameters deduced from TEM images shows a mean diameter of 15.7 nm with a polydispersity of 30% in 120 min of growth (Figure 6.3d). The domains are therefore large enough to support a strong plasmon oscillation where the bulk dielectric function of gold describes the optical properties well.

To learn more about the growth kinetics, we carefully analyzed the evolution of particle size gradually using three methods: TEM analysis of aliquots taken at regular time intervals, real-time optical extinction monitoring during growth, and single particle spectroscopy of individual particles in a flow cell.

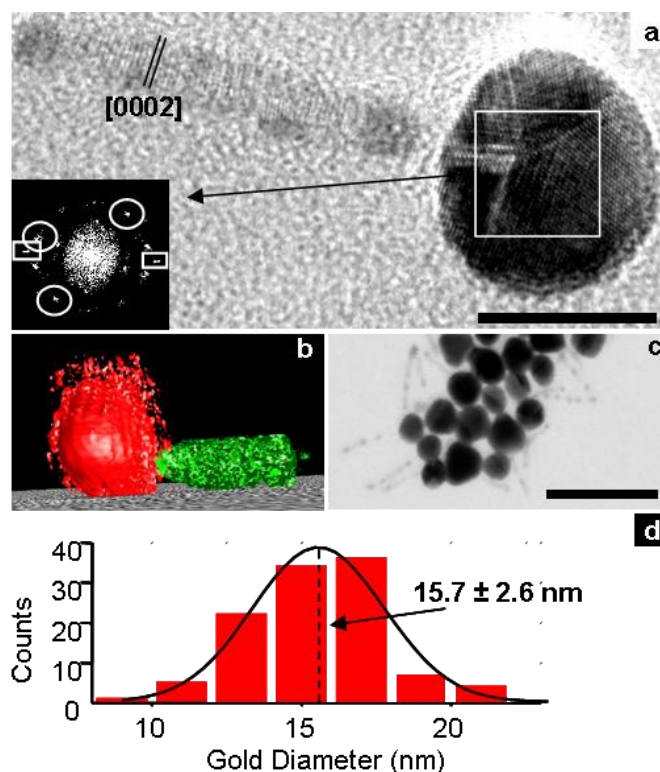


**Figure 6.3.** (a) Representative HR-TEM image of the Au-CdS hybrid particle displaying a five-fold symmetry of the gold domain nucleated on one nanorod tip. The inset shows a FFT-pattern of the gold domain region indicated by the white box. Circles and squares mark the 111 and 220 reflections, respectively. Visible on the lateral nanorods facets and on the opposite tip are

small gold islands (*scale bar 10 nm*). (b) Projection of the 3D particle model reconstructed from a tilt series (tomography) showing a non-centrosymmetric gold domain attachment. (c) High-resolution SEM image (*scale bar 50 nm*). (d) Gold domain size distribution of more than 100 particles for a generic sample irradiated for 120 minutes.

The results of the TEM analysis are shown in Figure 5. We measured the diameter of the gold domains of approximately 100 particles per sample on low-resolution TEM images after reaction times of 2, 5, 11, 30, 60, 90, and 120 min. Independent of the employed starting material (CdS, CdSe/CdS, dumbbells), the volume of the gold domain shows a linear increase over time at a rate of about  $0.24 \text{ nm}^3/\text{s}$  (14 atoms/s) as expected from a constant rate of electron generation in the semiconductor particle. Since the plasmon excitation ( $\approx 530 \text{ nm}$ ) does not overlap with the semiconductor rod absorption, simultaneous optical extinction measurements during the growth show a corresponding increase in the optical density around the plasmon resonance (Figure 6.4 inset). For irradiation times longer than 120 min, the particles start to aggregate and the gold domains fuse together.

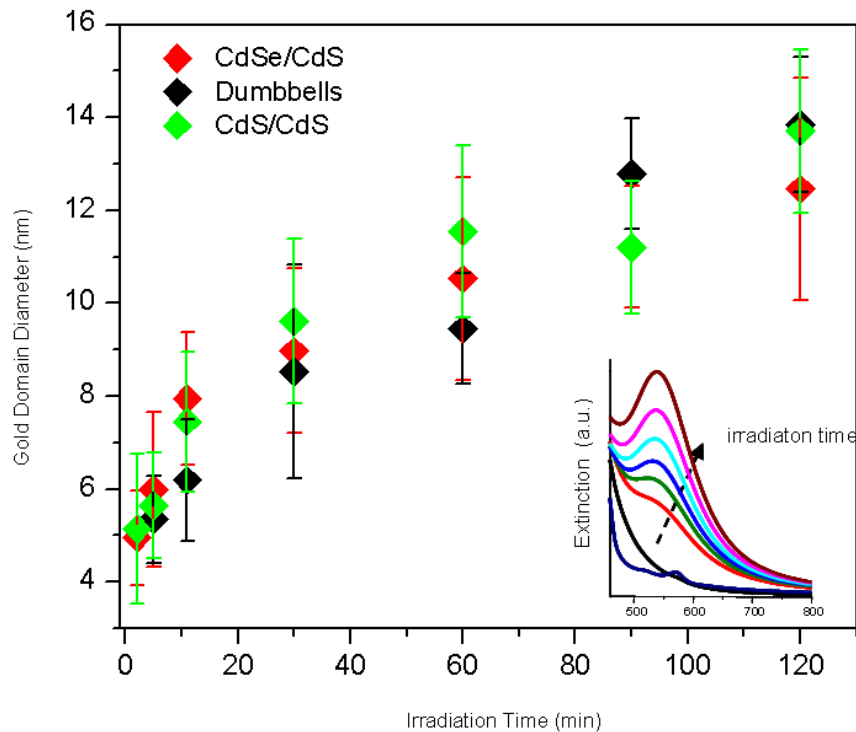


**Figure 6.4.** Gold domain diameter extracted from TEM images (100 nanoparticles per data point). The inset shows the optical extinction with increasing UV irradiation time. The plasmon peak at 536 nm grows over time.

From the measured absorbance and the particle concentration, we have estimated an absorption cross section of our CdS rods of  $4.46 \cdot 10^{-14} \text{ cm}^2$  at 366 nm, which means the generation of 166 photoelectrons/s per particle at our irradiation intensity ( $2 \text{ mW/cm}^2$ ). From this, we estimate that after 120 min, *circa* 50% of the injected gold ions have been reduced. Assuming all gold ions in the +3 oxidation state, we calculate an efficiency of approximately 25% for the photo-reduction process. The charge separation process in our metal-semiconductor hybrid particles is therefore very efficient and promising for light harvesting purposes.

With the aim to avoid particle aggregation and to monitor the metal growth in real time, we performed single particle measurements of nanorods immobilized in a glass flow cell. Details of the setup (Fig 6.5a), the flow cell and the

immobilization protocol can be found in the Appendix. At first, CdSe/CdS nanorods are fixed in the flow cell. Their location *before* the addition of gold is determined by looking at their fluorescent signal (blinking) on excitation at 405 nm. Then we change the medium to the gold growth solution (everything under anaerobic conditions) and keep a constant flow to avoid depletion of gold ions. A simultaneous white-light illumination through an ultra-high numerical aperture dark-field condenser allows the observation of light scattered by the growing gold domains at the places where previously fluorescence signal of immobilized CdSe/CdS nanorods was observed.

The fluorescent signal was completely quenched as soon as the gold ions are added but a growing light scattering signal  $I_{\text{sca}}$  of gold domains develops. After about 1 min of growth, the signal was clearly above noise level and gradually increases with time. (We analyzed the temporal evolution of the gold domain growth of several single particles here not shown, all cases showed gold domains diameter growing linearly in time). The intensity  $I_{\text{sca}}$  was converted to particle volume  $V$  by comparing with the intensity of 40 nm Au spherical particles and using the relation  $I_{\text{sca}} \sim V^2$ . We observed a linear increase of the gold domain diameter over time with 1.4 to 2.6 nm/min and no sign of saturation. The linear increase in diameter (not volume) with time indicates a diffusion controlled step as a limiting factor in the reaction not the amount of photo-electrons generated in the particle.

Control experiments without semiconductor rods show no significant gold particle formation under laser irradiation. Evidence of the gold growth on the semiconductor comes from experiments performed on the TEM-substrate. In these experiments, CdS rods are immobilized on the carbon grid. Then gold growth solution was dispensed dropwise onto the substrate. After illumination by

a 366 nm UV lamp for 5 min., the grid was rinsed with toluene, dried and TEM images were taken. (Figure 6.5b). Repetition of the growth step leads to further increase in gold domain size. (Figure 6.5)

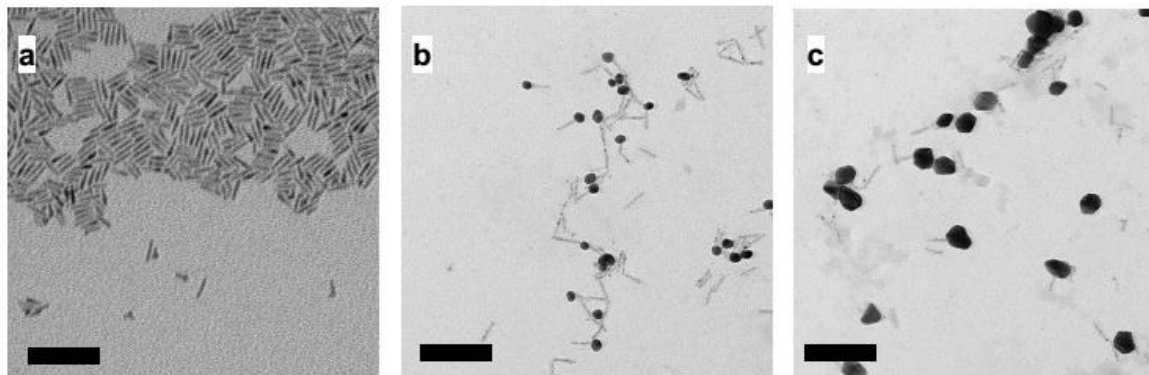


**Figure 6.5.** Light driven growth of the gold on TEM-grid substrate. a) initial CdS rods immobilized on the carbon grid. particles obtained after the first (b) and second exposure to UV light and gold growth solution. All scale bars are 100 nm.

Further insight confirming the light driven gold domain formation process shown in Figure 1 comes from a careful analysis of optical extinction measurements during particle growth. From spectra acquired every 30 sec, we extracted the spectral position of the plasmon extinction maximum  $\lambda_p$  (Figure 6.6a, left axis) and the corresponding ‘intensity’  $I_p$  – the extinction value at the maximum (Figure 6.6a, right axis).  $I_p$  allows monitoring the growth of the gold domain and plasmon resonance  $\lambda_p$  indicates the accumulated charge.

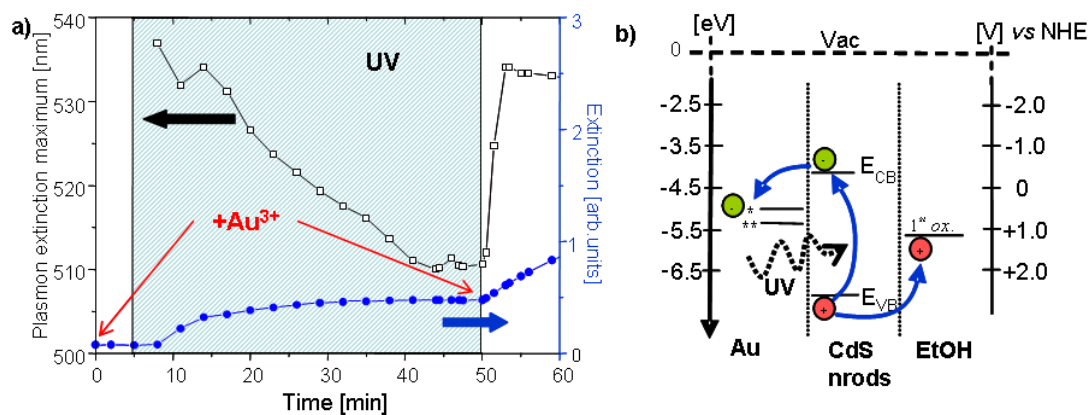


**Figure 6.6.** a) Spectral position of the plasmon extinction maximum  $\lambda_p$  and its absolute extinction value  $I_p$  over time. At time  $t = 0$ , a small amount of gold ions (ca. 6000 Au atoms per rod) were added to CdSe/CdS nanorods in a mixture of ethanol and chloroform (b) Diagram of the Fermi level of the gold domain (left), the conduction and valence band edges of CdS nanorods ( $E_{CB}$ ,  $E_{VB}$ , respectively) and the 1<sup>st</sup> oxidation level of ethanol before irradiation. The bulk Fermi-level of gold (\*) is slightly shifted in small gold domains (\*\*).

At the beginning an amount of gold ions insufficient to form the large gold domains was added. Under UV irradiation, the plasmon peak intensity  $I_p$  started to increase indicating Au growth. In about 30 min of UV irradiation, the plasmon intensity increase leveled off indicating the depletion of gold ions and arrest of growth. However, the plasmon peak-position  $\lambda_p$  shifted to the blue with a constant rate from its initial position at about  $\lambda_p = 535$  nm. Only in 40 min, we observed a sudden stop at 510 nm (25 nm blue shift). The blueshift is due to an accumulation of negative charges in the gold domain, increasing its electron density and plasmon frequency. The saturation indicates equilibrium of the metal's Fermi level and the semiconductor conduction band edge. The observed shift seems reasonable looking at the energy diagram (Figure 8b) and a previously measured plasmon shift of 29 nm per 1V in 2 nm gold spheres. After 50 min, we stop the UV irradiation and add more gold ions discharging the gold domains, thus rapidly

shifting back the plasmon resonance, and increasing again the plasmon intensity  $I_p$ .

## Conclusions

TEM data, optical extinction measurements, and the single particle growth data support the model of photo-induced one-sided gold domain formation on semiconductor rods. This model involves no ripening but rather a directed photo-electron drift towards the largest gold domain. The UV excitation leads to a growth of only one domain per semiconductor rod resulting in an anisotropic ‘smoking-pipe’ structure. Due to the large metal part the hybrid particles can be easily transferred to polar solvents after a proper functionalization (images not shown, see Methodology Section for details). The conversion of photo-generated electrons to reduced gold atoms is very efficient at early times. The single particle measurements demonstrate that gold domains can be arbitrarily large on supported particles in a flow cell. A careful analysis of the plasmon peak position during growth shows the buildup of electrons in the gold domain. We create *large* gold domains with only *one* domain per rod in contrast to other systems where photo-deposition of metals on semiconductors was observed (e.g. Ag, Au, Cu, Pt on ZnO or TiO<sub>2</sub>).

The light driven large gold domain formation on semiconductor nanorods allows for the controlled synthesis of nanocrystals supporting both plasmons and excitons with a light scattering cross section large enough to visualize single hybrid particles in a dark-field microscope. The only drawback of the proposed synthesis is that a prolonged reaction leads not to larger gold domain, but to the fusion of the domains together (Figure 6.8).

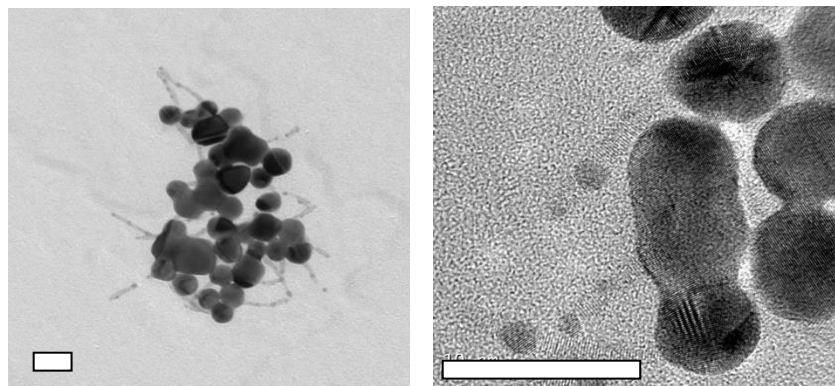


**Figure 6.7.** Fusion of the gold domain under prolonged irradiation with UV-light in chloroform. Scale bar is 20 nm.

## 7 Photoreduction of Gold In Aqueous Media – alternative synthesis of the Au-CdS@CdSe Matchstick Hybrid Nanoparticles\*

So far most of the developed cadmium chalcogenide – Au hybrids were synthesized in organic media (usually chloroform) in the presence of amines following the method of Uri Banin and co-workers.[*Mokari, 2004; Mokari, 2006; Khalavka, 2008; Menagen, 2008; Menagen, 2009; Sheldon, 2009; Figuerola, 2010*] This synthesis was further improved by the decreasing temperature in combination with optimal ligand selection and allowed production particles without “defect” gold decoration of semiconductor part.[*Menagen, 2009*] In such systems photocatalysis and enhanced electric conductivity are reported.[*Elmalem, 2008; Sheldon, 2009*] Recently light-induced growth was used to grow Pd and iron oxide on the preformed gold tips of the particles [*Li*] End-to-end and side-by-side [*Zhao, 2009*] assemblies open new possibilities for attractive applications like nanoelectronics and energy-harvesting materials.

Main limitation of the synthesis in organic phase is that after reaching certain limit of the gold domain (about 20 nm), particles form aggregates and finally welds through the gold parts. [*Carbone, 2009*] Therefore there is a demand in the development of alternative synthetic procedures of the gold growth leading to hybrid particles. For instance, thermally induced growth by the reduction of Au-oleate complexes has been recently developed by M. Zamkov [*Khon, 2010; Khon, 2011*] but achieved particles were rather polydisperse and size of the gold domain did not exceed 20 nm either.

---

\* A version of this chapter is submitted as **Yuriy Khalavka**, Sebastian Harms, Andreas Henkel, Malte Strozyk and Carsten Sönnichsen  
*Synthesis of Au-CdS@CdSe Hybrid Nanoparticles with Highly Reactive Gold Domain*

In this chapter I describe novel synthesis of the CdS@CdSe-Au nanoparticles in water which allows producing particles with basically unlimited size of the gold domain. Our approach leads to a particle where the gold domain is covered with loosely attached surfactant making it accessible to further modification. Idea, all experiments and data analysis I have made by myself. Single particle measurements were performed with Dr. Anderas Henkel. S.Harms and M.Strozhyk were involved in the control experiments.

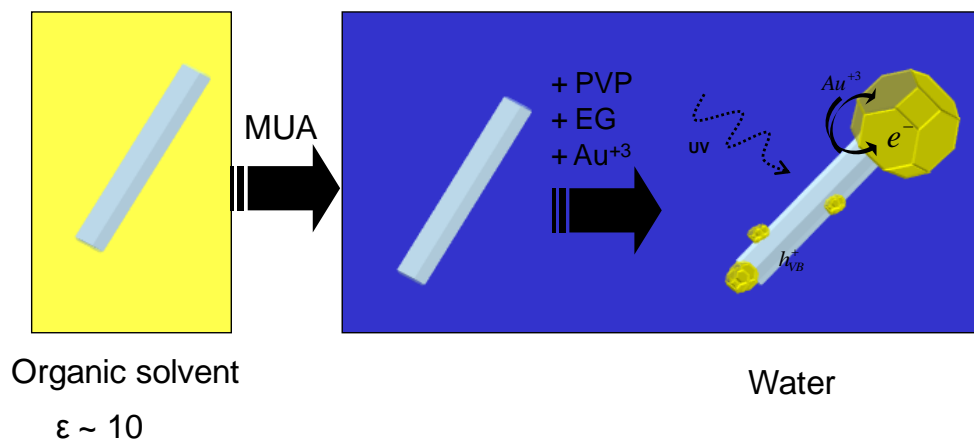


**Figure 7.1.** Schematics presenting proposed strategy of the nanohybrid synthesis in water solution.

### Growth of the hybrid nanoparticles

CdS nanorods (with dimensions 70 by 6 nm) used here as substrate material were synthesized from CdSe seeds according to the method reported earlier[Carbone, 2007] and were transferred to the aqueous phase using mercaptoundecanoic acid. Then UV irradiation was applied after addition of poly(vinyl pyrrolidone) (PVP) and ethylene glycol(EG) to selectively grow Au domain on one side of the rods. Diameter of gold can be tuned either by chosen Au/CdS ratio or\and irradiation time. We analyze the growth of gold onto semiconductor rods by transmission electron microscopy (TEM). Representative

electron microphotographs are shown on Figure 7.2. Relative size distribution of the gold domains does not exceed 40%.

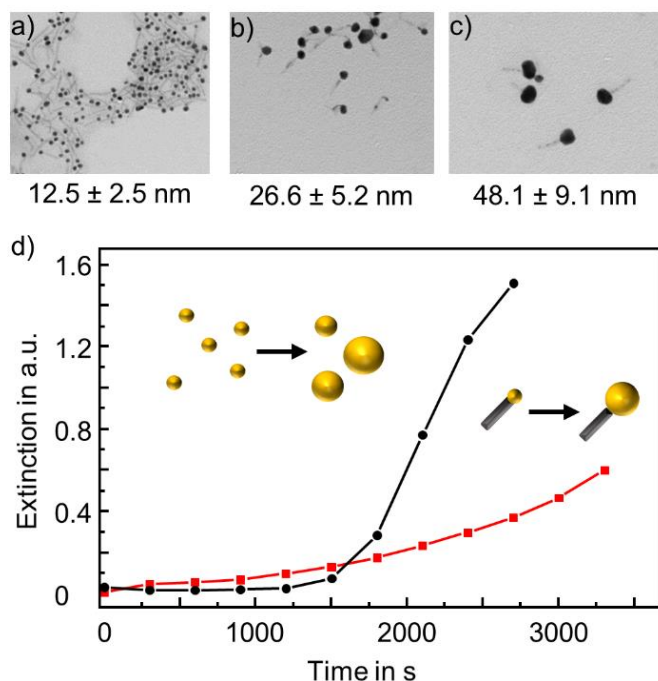


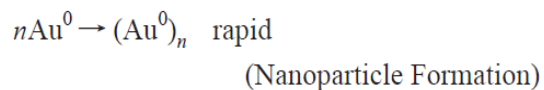
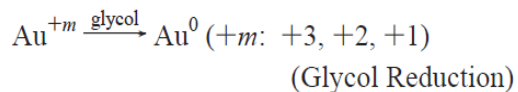
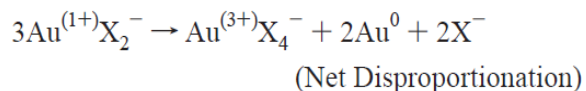
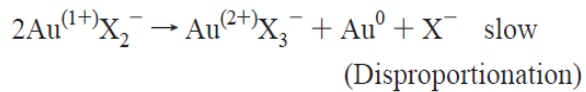
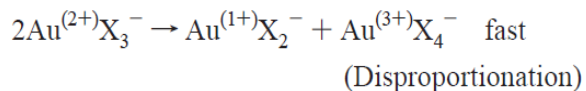
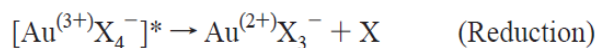
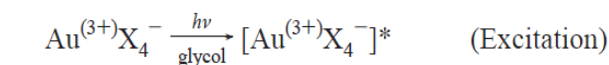
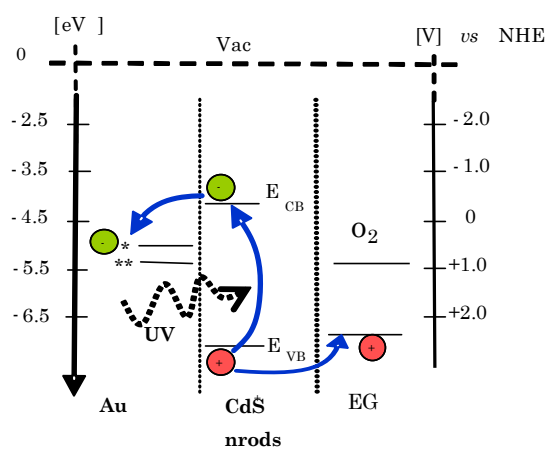
**Figure 7.2.** Au-CdS nanohybrids isolated from the growth solution after 10 (a), 20(b) and 30 (c) minutes of irradiation. (d) Growth of the intensity of the plasmon peak during the UV irradiation of the Au - Ethylen glycol-water solution, with and without CdS nanorods. Inset shows changes of the full spectra in time.

Growth of the gold domain can be monitored by the optical absorption method, which provides valuable information about its mechanism. During the UV irradiation the absorbance spectrum of CdS nanorods evolves into a spectrum with a well distinguishable peak at 540-560 nm which corresponds to the plasmon excitation in the gold sphere.

In agreement with the previous report of [Mokari, 2004] at an early step of the growth, several small domains of gold are deposited on the semiconductor nanorods. Then one of them, usually at the tip of the rod starts to grow faster. Shape transition from hemispherical shape of nuclei to more round shape of growing domain leads to a slight “blue” shift of the plasmon resonance wavelength [Sonnichsen, 2011] and following intensity increase proportionally to the size of the domain. We have not observed self nucleation of the gold particles, even at the highest studied  $\text{Au}^{3+}$  concentration. Control experiments carried

without CdS demonstrate that in this case induction period is longer as higher concentration of Au-monomers is required for the homogeneous nucleation than for the heterogeneous one.

Reduction of Au by the ethylene glycol in water has been studied in details by El-Sayed and co-workers. [Eustis, 2005; Eustis, 2006] According to them first  $\text{Au}^{3+}$  is excited by UV light and after several sequential steps reduced to  $\text{Au}^+$  which then disproportionate to  $\text{Au}^0$  and to  $\text{Au}^{3+}$ . This process (so called “dark phase”) also takes place when irradiation is switched off. (See scheme below)



In respect to this model I have to mention that despite EG does not absorb much light in the spectral range of applied UV-light, pre-irradiation of the solution for 10 min, before adding the gold significantly decreases of the “induction” period, but does not affect results of the synthesis.

It has to be mentioned that CdS itself provides redox potential strong enough to reduce Au ions by the photogenerated electrons. [Carbone, 2009] But in our case concentrations of gold-ions and molecules of EG are much higher than

CdS nanorods and therefore predominant pathway is when CdS-nanorods serve more as nucleation centers than reduction sites. High dielectric constant of water decreases Van-der-Vaals attraction of the gold domains and therefore prevents welding even after long reaction times.

When the size of the gold in hybrids is larger than 25 nm – it becomes possible to resolve full single particle spectrum by dark-field spectroscopy method. We use a flow cell made from a flat borosilicate glass capillary glued with epoxy to polyethylene tubing for single-particle optical characterization in an oxygen-free environment.

SEM examination of flowcell opened after the measurement with Correlative navigation software (figure 7.3), tells us that less than 20% of particles form aggregates during sample preparation.

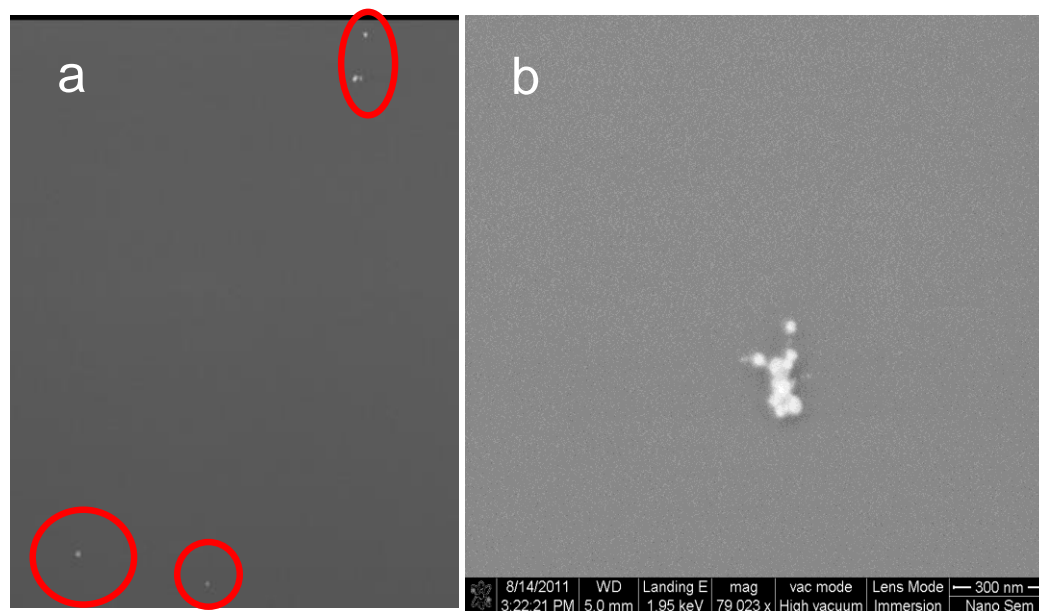


**Figure 7.3** Examples of low (a) and high (b) resolution scanning electron microscopy images, used to analyze aggregation of the hybrid particles in course of sample preparation for single particle measurements. High brightness of the gold domains allow to distinguish aggregates from single particles even at low resolution images.

Summarized statistics over more than 100 measured spectra shows resonance positions in the range of lower energies (2-2,1 eV) for hybrids than for pure gold nanospheres of the same diameter (range of 2,3 eV) because of attachment of semiconductor which increases average refractive index around the particle. (Figure 7.4)

A relatively slow process of growth allows precise tuning of the size of the gold domain, but, if necessary, reaction can be completely stopped via adding excess of water-soluble thiols i.e. thioglycolic acid due to the formation of strong Au-thiol complex and of the thiol monolayer on the surface of the gold.

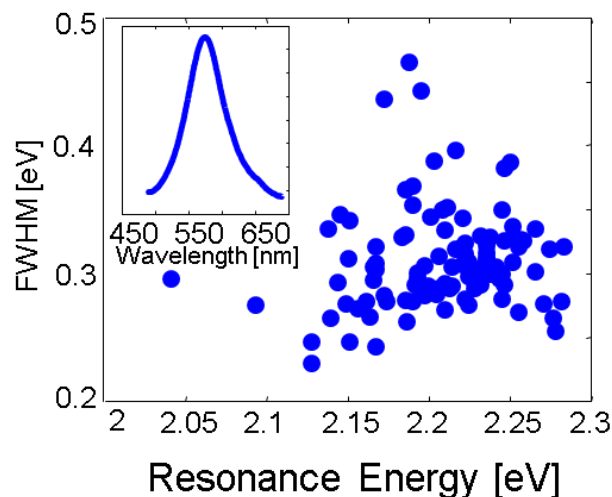


**Figure 7.4.** Berg plot of the plasmon scattering extracted from single particle measurements for the sample with particle size in the range of 30±6 nm. Example of full single particle spectrum is inserted.

## Gold domains as reaction centers

A lot of applications of hybrid nanomaterials for instance in catalysis require their transfer from the growth solution to the interface, to another solvent or selective functionalization. When synthesized in organic media they are usually transferred to the water by HS-PEG [Carbone, 2010] or mercaptoundecanoic acid. Consecutively transferred hybrid nanoparticles are difficult to be selectively functionalized due to similar affinity of the surfactant to both Au and CdS surfaces. We have selected PVP as a stabilizer of gold part not only to prevent aggregation and to slow down the reaction making heterogeneous nucleation more favorable. Its molecules also are attaching to the gold domain not so strongly as thiols and therefore metal surface can be accessed by other ions and molecules. [Tsukuda, 2009] The 11-mercaptoundecanoic acid monolayer raised the resistance to  $3 \times 10^4$  times in comparison to observed at a bare electrode [Komura, 2004], basically this annihilates the benefit of the gold decoration for the charge transfer observed by Sheldon et al [Sheldon, 2009].

We have done two experiments to support this idea. At first re-growth of gold domains is possible, after the synthesis was completely stopped and particles were purified by the centrifugation (Figure 4).

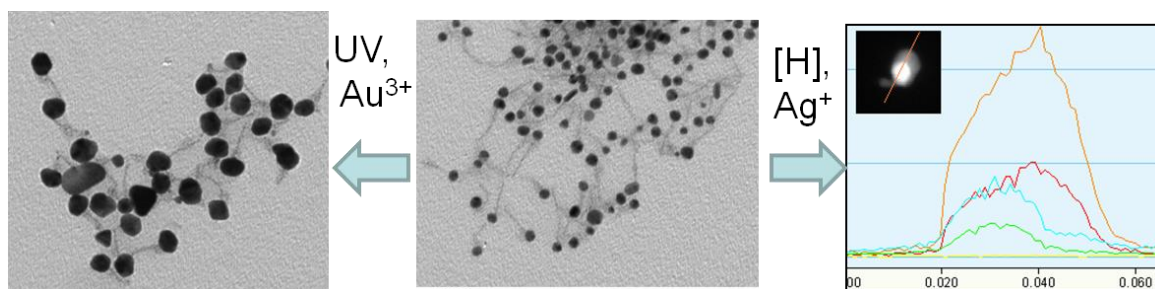


**Figure 7.6.** Results of experiments demonstrating accessibility of gold surface to further modification.

We were also able to cover gold domain with the silver shell using the procedure reported earlier. [Sonnichsen, 2008] Despite the degradation of semiconductor part gold domain is nicely covered by the silver shell.

### Catalytic reduction of 4-nitrophenol

As gold nanoparticles catalyze the 4-nitrophenol reduction by the sodium borohydride, we also tested our particles in this reaction. This reaction takes place at the gold surface and is known to be dependent on the surface coverage. It can be easily monitored by the UV-vis spectroscopy as a gradual decay of 4-nitrophenol absorption band at 430 nm. Comparison of the PVP-protected particles with those incubated with MUA and citrate-stabilized gold particles of the same diameter demonstrates clear faster reduction rate by the as-grown hybrids, than by the citrate coated gold and no remarkable reduction has been observed in the case of MUA-coated hybrids.

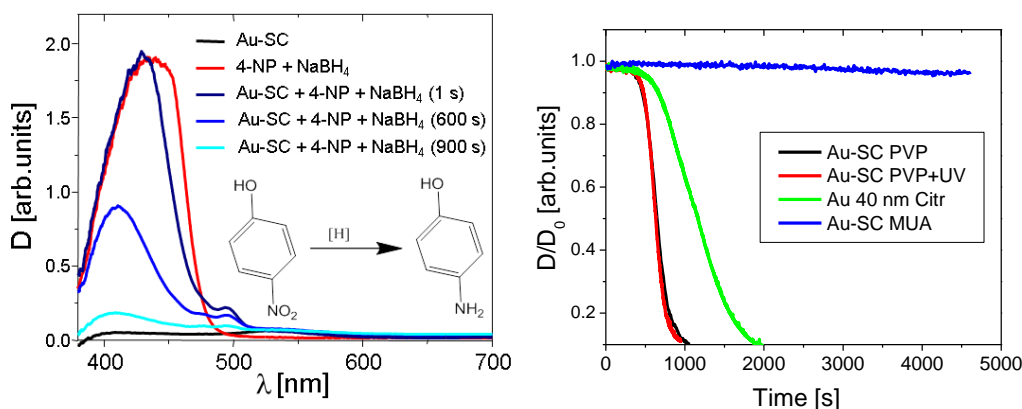


**Figure 7.7.** Absorption spectra of p-nitrophenol – sodium borohydride before and after the addition of hybrid nanoparticles (a), Changes of the optical density of the maximum of the p-nitrophenol absorption, in the presence of equal amount of hybrid nanoparticles (red curve), gold nanospheres stabilized with citric acid (green) and hybrids pre-incubated with mercaptoundecanoic acid (blue) (b).

Interesting effect confirming catalytic activity of the gold domain can be observed during this reaction. After the addition of reducing agent – the plasmon scattering of gold domain (barely noticeable in the absorption spectrum) increases and its energy shifts to the higher energy. Both of these effects occur due to the increase of electron density in the gold. They vanish immediately after the end of the reaction. While  $\text{NaBH}_4$  is in excess in the reaction vessel and charging of the gold domain should stay, this means that observable effect is dynamic and related to the catalytic activity of the gold. The importance of accessibility of the gold surface for this effect to happen is confirmed with following experiment. After the addition of the hybrid nanoparticles intensity of the plasmon scattering increases and stays constant during the reaction between the dye and reducing agent, but peak disappears immediately after injection of the sodium mercaptoundecanate. Intensity of the the p-nitrophenol stops to decrease, meaning that catalytic activity of the gold is gone, and reaction is not occurring anymore. (Figure. 7.8 )

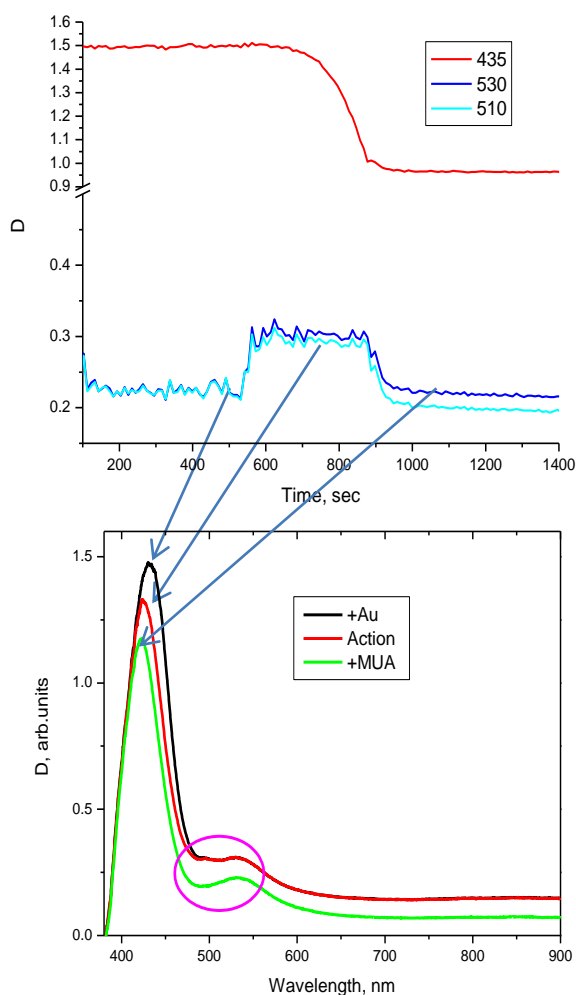


**Figure 7.8.** (a) Intensity changes at denoted wavelengths in course of the photoreduction and after addition of surface blocking agent (MUA) (b) Corresponding spectra to each of the steps

### Shape control of the gold domain

Studied synthesis procedure especially at high concentration of  $\text{HAuCl}_4$  leads to the gold domains sometimes (up to 20%) occurs in triangular shape (fig. 7.9). In accordance with the model of kinetically-controlled growth of the metal nanocrystals proposed by N. Ravishankar [Ravishankar, 2009] weak reduction agents like EG provide potentials at which symmetry breaking is likely to occur and therefore formation of the 2D structures of Au is favorable. Presence of the semiconductor further increases probability of the symmetry breaking. It leads to

shovel-like structure with very characteristic defects in the place of the gold-semiconductor interface.

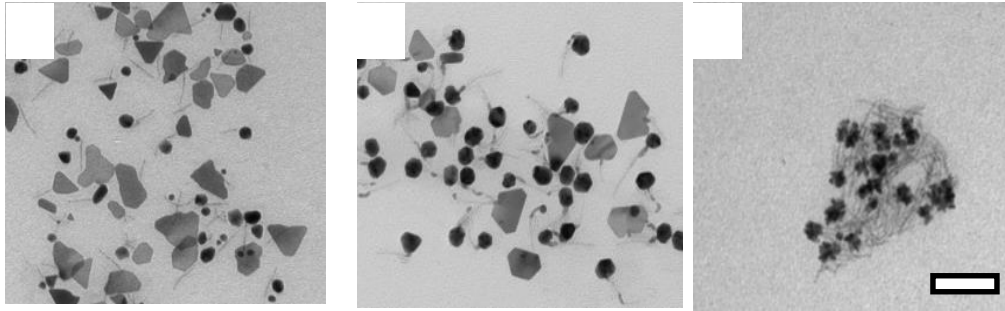
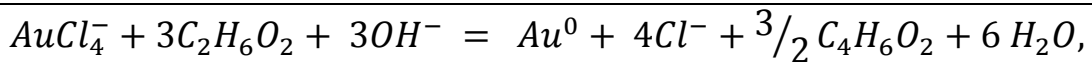
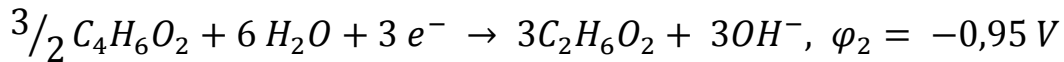
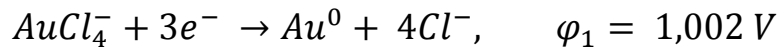


**Figure 7.9.** Hybrid structures produced with different reaction driving forces

At relatively low concentrations of stabilizer thermodynamic factors become more important. Using theory described in the chapter 2 and



$$E = -0,052 V - 0,000066138 (T) \log \frac{[Au][Cl^-]^4[C_4H_6O_2]^{3/2}}{[AuCl_4^-][C_2H_6O_2]^3[OH^-]^3} =$$

$$= -0,052 V - 0,000066138 (T) \log \frac{[Cl^-]^4[H^+]^3}{[AuCl_4^-][C_2H_6O_2]^3 \cdot 10^{-14}}$$

$$= -0,052 V - 0,000066138 (T) \log \frac{[Cl^-]^4[H^+]^3}{[AuCl_4^-][C_2H_6O_2]^3 \cdot 10^{-14}} =$$

$$= -0,052 V + 6,6138 \times$$

$$\times 10^{-5}(T)(3 \text{ pH} - 3 \log[AuCl_4^-] + 11,6 - 3 \log[C_2H_6O_2])$$

Diacetyl tends to be oxidized completely to  $H_2CO_3$ ,  $HCO_3^-$ , and  $CO_3^{2-}$  and I quite volatile to stay in the system and contribute to the equilibrium. Taking this into account I have plotted the thermodynamic diagrams (figure.7.10) for this particular reaction.

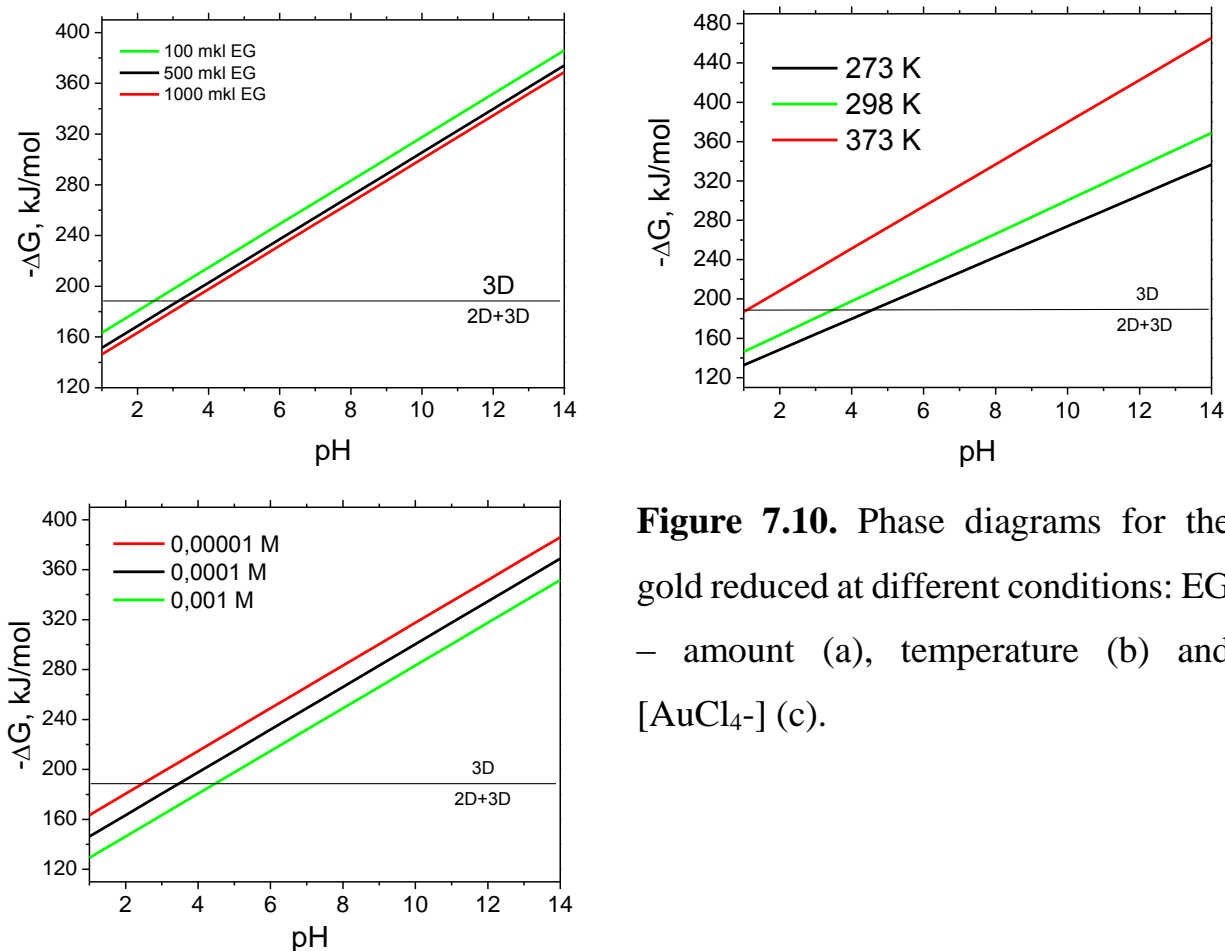


**Figure 7.10.** Phase diagrams for the gold reduced at different conditions: EG – amount (a), temperature (b) and  $[\text{AuCl}_4^-]$  (c).

This modeling estimates that increase of the concentration of Au-ions, and decrease of the pH should support 2D growth of the gold domains and this is what is observed in our case. Changes in the concentration of the ethylene glycol should not influence reaction so much, from discussed point of view, but the viscosity changes at high EG concentrations may have impact on the growth rate, or reaction mechanism as well.

Uprising the pH to 11 increases reduction potential of EG and lead to fast gold reduction and irregular shape (where several gold clusters are joined together) of tips even without UV-light. Both shovel- (see HR TEM images at the Figure 7.11) and flower-shaped hybrids are new in the pool of CdS-Au nanostructures and will be the object of our further studies.

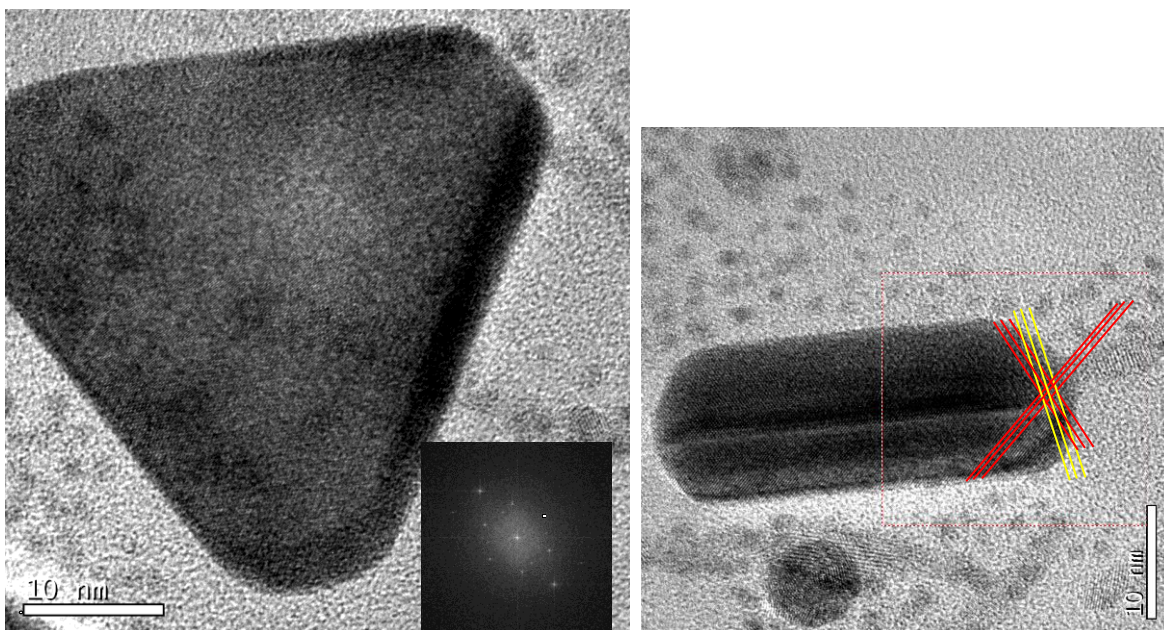


**Figure 7.11.** High resolution electron microscopy images of “shovel”-like hybrid nanoparticles, [111] surface and twin-plane can be distinguished to support growth mechanism discussed in chapter 2.

### Conclusion

This novel synthesis route for Au-CdS@CdSe hybrid nanoparticles, that enabled us to grow gold domains larger than 20 nm in diameter while retaining an active and accessible gold domain, provides a tunable system to observe plasmon-exciton interactions and photochemical charging effects.<sup>25-27</sup> The accessible gold domain provides exciting opportunities for self-assembling match-stick like inorganic particles into complex artificial structures and offers new possibilities to explore catalytic applications. I expect that particles produced by this new synthetic approach will allow to extend available shapes for metal-semiconductor nanoparticles and to understand exciton-plasmon interaction far more in details than it was done till now.

## Summary

In the course of my research several nanostructures important for the application in catalysis and energy conversion have been synthesized for the first time. They include rod-like gold nanorattles, hyperbranched CdTe nanoparticles covered with gold tips, and one-dimensional semiconductor-gold nanostructures. The produced structures are potential candidates to be active elements of a catalytic system and photovoltaic devices.

Porous gold nanorattles entrapping gold nanorod inside a gold cage have been described as the first system. Well known Kirkendall effect throughout the epitaxial silver deposition and its galvanic replacement by gold have been used to obtain such structures. Rodshaped nanorattles have demonstrated a promising refractive index of sensitivity and increased the catalytic activity due to the highly developed surface. They are also more stable than nanostructures made of silver.

The following chapters of the thesis are about hybrid gold-semiconductor nanoparticles and the ways how to make them. I have focused on CdTe and CdS nanoparticles as  $A^2B^6$  semiconductor nanomaterials which can be used for different optoelectronic devices, including solar cells and field-effect transistors. Three relevant approaches have been established to synthesize such structures, taking into account the reactivity of the semiconductor part. In case of highly reactive CdTe – gold can be deposited on the tips due to the sacrificial reaction, confirmed by elemental and structural analysis, making right concentration ratio between the semiconductor and gold being critical for the success of the process. CdS, however, is more stable towards the etching with the gold ions, therefore external stimuli for the mild reduction leading to the gold deposition were applied. UV light illumination in the presence of amines leads to the one-sided growth of the gold domain on the tip of seeded-grown CdS rods. The next step was to increase the size of the gold domain and to keep it chemically and electrically

active. To achieve this goal two-step approaches have been proposed – substrate semiconductor nanorods are transferred to the water phase via ligand exchange to mercapoundecanoic acid, and then gold domain is grown by UV-light illumination in the presence of polyvinylpyrrolidone. The particles which have been synthesized this way contain gold domain which is big enough to demonstrate strong light scattering, while its surface can be chemically modified ( being shown here by silver coating) or used to catalyze the reaction of 4-nitrophenol reduction by sodium borohydride in aqueous medium.

Though I have tried my best to improve synthetic procedures and to characterize the produced nanoparticles, there is still much to be done. Among further possible research activities I would list the following ones :

- Development of the reliable, high yield synthetic procedure for the hybrid nanomaterials with the gold domain of the shape other than spherical.
- Experimental studies (for instance, cyclic voltammetry) of band alignment in hybrid metal-semiconductor structures.
- Studies of the dynamics of electron accumulation in the gold domains.
- Theoretical and experimental studies of exciton-plasmon interaction in hybrid nanoparticles of different shapes (also at the single-particle level).
- Development of the methods to precisely control assembly of hybrid nanoparticles at the large scale..

## References

- Alivisatos, A. P. *Journal of Physical Chemistry* **1996**, *100*, 13226  
*Perspectives on the physical chemistry of semiconductor nanocrystals.*
- Anker, J. N.; Hall, W. P.; Lyandres, O.; Shah, N. C.; Zhao, J.; Van Duyne, R. P. *Nature Materials* **2008**, *7*, 442  
*Biosensing with plasmonic nanosensors.*
- Baciu, C. L.; Becker, J.; Janshoff, A.; Sönnichsen, C. *Nano Letters* **2008**, *8*, 1724  
*Protein-Membrane Interaction Probed by Single Plasmonic Nanoparticles.*
- Becker, J.; Schubert, O.; Sönnichsen, C. *Nano Lett.* **2007**, *7*, 1664  
*Gold Nanoparticle Growth Monitored in situ Using a Novel Fast Optical Single-Particle Spectroscopy Method.*
- Buck, M. R.; Bondi, J. F.; Schaak, R. E. *Nat. Chem.* **2012**, *4*, 37  
*A total-synthesis framework for the construction of high-order colloidal hybrid nanoparticles.*
- Bunge, S. D.; Krueger, K. M.; Boyle, T. J.; Rodriguez, M. A.; Headley, T. J.; Colvin, V. L. *Journal of Materials Chemistry* **2003**, *13*, 1705  
*Growth and morphology of cadmium chalcogenides: the synthesis of nanorods, tetrapods, and spheres from CdO and Cd(O<sub>2</sub>CCH<sub>3</sub>)<sub>2</sub>.*
- Buonsanti, R.; Grillo, V.; Carlino, E.; Giannini, C.; Curri, M. L.; Innocenti, C.; Sangregorio, C.; Achterhold, K.; Parak, F. G.; Agostiano, A.; Cozzoli, P. D. *Journal of the American Chemical Society* **2006**, *128*, 16953  
*Seeded Growth of Asymmetric Binary Nanocrystals Made of a Semiconductor TiO<sub>2</sub> Rodlike Section and a Magnetic  $\gamma$ -Fe<sub>2</sub>O<sub>3</sub> Spherical Domain.*
- Burda, C.; Chen, X. B.; Narayanan, R.; El-Sayed, M. A. *Chem. Rev.* **2005**, *105*, 1025  
*Chemistry and properties of nanocrystals of different shapes.*
- Cahn, J. W. *Acta Metall Mater* **1960**, *8*, 554  
*Theory of Crystal Growth and Interface Motion in Crystalline Materials.*
- Carbone, L.; Cozzoli, P. D. *Nano Today* **2011**, *5*, 449  
*Colloidal heterostructured nanocrystals: Synthesis and growth mechanisms.*
- Carbone, L.; Jakab, A.; Khalavka, Y.; Sönnichsen, C. *Nano Letters* **2009**, *9*, 3710

*Light-Controlled One-Sided Growth of Large Plasmonic Gold Domains on Quantum Rods Observed on the Single Particle Level.*

Carbone, L.; Jakab, A.; Khalavka, Y.; Sonnichsen, C. In *Colloidal Quantum Dots for Biomedical Applications V*; Osinski, M., Parak, W. J., Jovin, T. M., Yamamoto, K., Eds.; SPIE: San Francisco, California, USA, 2010; Vol. 7575, pp 757505.

Carbone, L.; Kudera, S.; Carlino, E.; Parak, W. J.; Giannini, C.; Cingolani, R.; Manna, L. *Journal of the American Chemical Society* **2006**, *128*, 748

*Multiple wurtzite twinning in CdTe nanocrystals induced by methylphosphonic acid.*

Carbone, L.; Kudera, S.; Giannini, C.; Ciccarella, G.; Cingolani, R.; Cozzoli, P. D.; Manna, L. *Journal of Materials Chemistry* **2006**, *16*, 3952

*Selective reactions on the tips of colloidal semiconductor nanorods.*

Carbone, L.; Nobile, C.; DeGiorgi, M.; Sala, F. D.; Morello, G.; Pompa, P.; Hytch, M.; Snoeck, E.; Fiore, A.; Franchini, I. R.; Nadasan, M.; Silvestre, A. F.; Chiodo, L.; Kudera, S.; Cingolani, R.; Krahne, R.; Manna, L. *Nano Lett.* **2007**, *7*, 2942

*Synthesis and Micrometer-Scale Assembly of Colloidal CdSe/CdS Nanorods Prepared by a Seeded Growth Approach.*

Caswell, K. K.; Wilson, J. N.; Bunz, U. H. F.; Murphy, C. J. *Journal of the American Chemical Society* **2003**, *125*, 13914

*Preferential End-to-End Assembly of Gold Nanorods by Biotin-Streptavidin Connectors.*

Cortie, M. B.; McDonagh, A. M. *Chem. Rev.* **2011**, *111*, 3713

*Synthesis and Optical Properties of Hybrid and Alloy Plasmonic Nanoparticles.*

Costi, R.; Saunders, A. E.; Banin, U. *Angew Chem Int Edit* **2010**, *49*, 4878

*Colloidal Hybrid Nanostructures: A New Type of Functional Materials.*

Costi, R.; Saunders, A. E.; Elmaleh, E.; Salant, A.; Banin, U. *Nano Letters* **2008**, *8*, 637

*Visible Light-Induced Charge Retention and Photocatalysis with Hybrid CdSe-Au Nanodumbbells.*

Cozzoli, P. D.; Comparelli, R.; Fanizza, E.; Curri, M. L.; Agostiano, A.; Laub, D. *Journal of the American Chemical Society* **2004**, *126*, 3868

*Photocatalytic Synthesis of Silver Nanoparticles Stabilized by TiO<sub>2</sub> Nanorods: A Semiconductor/Metal Nanocomposite in Homogeneous Nonpolar Solution.*

- Cozzoli, P. D.; Curri, M. L.; Agostiano, A. *Chemical Communications* **2005**, 3186  
*Efficient charge storage in photoexcited TiO<sub>2</sub> nanorod-noble metal nanoparticle composite systems.*
- Cozzoli, P. D.; Curri, M. L.; Giannini, C.; Agostiano, A. *Small* **2006**, 2, 413  
*Synthesis of TiO<sub>2</sub>-Au Composites by Titania-Nanorod-Assisted Generation of Gold Nanoparticles at Aqueous/Nonpolar Interfaces.*
- Cozzoli, P. D.; Manna, L. *Nature Materials* **2005**, 4, 801  
*Asymmetric nanoparticles - Tips on growing nanocrystals.*
- Cozzoli, P. D.; Pellegrino, T.; Manna, L. *Chemical Society Reviews* **2006**, 35, 1195  
*Synthesis, properties and perspectives of hybrid nanocrystal structures.*
- Dick, K. A.; Deppert, K.; Larsson, M. W.; Martensson, T.; Seifert, W.; Wallenberg, L. R.; Samuelson, L. *Nature Materials* **2004**, 3, 380  
*Synthesis of branched 'nanotrees' by controlled seeding of multiple branching events.*
- Dmitriev, A.; Hägglund, C.; Chen, S.; Fredriksson, H.; Pakizeh, T.; Käll, M.; Sutherland, D. S. *Nano Letters* **2008**, 8, 3893  
*Enhanced Nanoplasmonic Optical Sensors with Reduced Substrate Effect.*
- Elmalem, E.; Saunders, A. E.; Costi, R.; Salant, A.; Banin, U. *Advanced Materials* **2008**, 20, 4312  
*Growth of Photocatalytic CdSe-Pt Nanorods and Nanonets.*
- Esumi, K.; Isono, R.; Yoshimura, T. *Langmuir* **2004**, 20, 237  
*Preparation of PAMAM- and PPI-Metal (Silver, Platinum, and Palladium) Nanocomposites and Their Catalytic Activities for Reduction of 4-Nitrophenol.*
- Eustis, S.; El-Sayed, M. A. *Journal of Physical Chemistry B* **2006**, 110, 14014  
*Molecular mechanism of the photochemical generation of gold nanoparticles in ethylene glycol: Support for the disproportionation mechanism.*
- Eustis, S.; El-Sayed, M. A. *Chemical Society Reviews* **2006**, 35, 209  
*Why gold nanoparticles are more precious than pretty gold: Noble metal surface plasmon resonance and its enhancement of the radiative and nonradiative properties of nanocrystals of different shapes.*
- Eustis, S.; Hsu, H. Y.; El-Sayed, M. A. *Journal of Physical Chemistry B* **2005**, 109, 4811  
*Gold nanoparticle formation from photochemical reduction of Au<sup>3+</sup> by continuous excitation in colloidal solutions. A proposed molecular mechanism.*

- Fan, H. J.; Gösele, U.; Zacharias, M. *Small* **2007**, *3*, 1660  
*Formation of Nanotubes and Hollow Nanoparticles Based on Kirkendall and Diffusion Processes: A Review.*
- Fedutik, Y.; Temnov, V.; Woggon, U.; Ustinovich, E.; Artemyev, M. *Journal of the American Chemical Society* **2007**, *129*, 14939  
*Exciton-Plasmon Interaction in a Composite Metal-Insulator-Semiconductor Nanowire System.*
- Figuerola, A.; Franchini, I. R.; Fiore, A.; Mastria, R.; Falqui, A.; Bertoni, G.; Bals, S.; Van Tendeloo, G.; Kudera, S.; Cingolani, R.; Manna, L. *Advanced Materials* **2009**, *21*, 550  
*End-to-End Assembly of Shape-Controlled Nanocrystals via a Nanowelding Approach Mediated by Gold Domains.*
- Figuerola, A.; Huis, M. v.; Zanella, M.; Genovese, A.; Marras, S.; Falqui, A.; Zandbergen, H. W.; Cingolani, R.; Manna, L. *Nano Letters* **2010**, *10*, 3028  
*Epitaxial CdSe-Au Nanocrystal Heterostructures by Thermal Annealing.*
- Gomez, S.; Philippot, K.; Colliere, V.; Chaudret, B.; Senocq, F.; Lecante, P. *Chemical Communications* **2000**, 1945  
*Gold nanoparticles from self-assembled gold(I) amine precursors.*
- Gur, I.; Fromer, N. A.; Chen, C. P.; Kanaras, A. G.; Alivisatos, A. P. *Nano Letters* **2007**, *7*, 409  
*Hybrid solar cells with prescribed nanoscale morphologies based on hyperbranched semiconductor nanocrystals.*
- Hirakawa, T.; Kamat, P. V. *Langmuir* **2004**, *20*, 5645  
*Photoinduced Electron Storage and Surface Plasmon Modulation in Ag@TiO<sub>2</sub> Clusters.*
- Howes, P.; Green, M.; Bowers, A.; Parker, D.; Varma, G.; Kallumadil, M.; Hughes, M.; Warley, A.; Brain, A.; Botnar, R. *Journal of the American Chemical Society* **2010**, *132*, 9833  
*Magnetic Conjugated Polymer Nanoparticles as Bimodal Imaging Agents.*
- Hu, M.; Novo, C.; Funston, A.; Wang, H. N.; Staleva, H.; Zou, S. L.; Mulvaney, P.; Xia, Y. N.; Hartland, G. V. *Journal of Materials Chemistry* **2008**, *18*, 1949  
*Dark-field microscopy studies of single metal nanoparticles: understanding the factors that influence the linewidth of the localized surface plasmon resonance.*
- Hungria, A. B.; Juarez, B. H.; Klinke, C.; Weller, H.; Midgley, P. A. *Nano Res* **2008**, *1*, 89  
*3-D Characterization of CdSe Nanoparticles Attached to Carbon Nanotubes.*

- Kamat, P. V. *The Journal of Physical Chemistry C* **2008**, *112*, 18737  
*Quantum Dot Solar Cells. Semiconductor Nanocrystals as Light Harvesters.*
- Kanaras, A. G.; Sönnichsen, C.; Liu, H. T.; Alivisatos, A. P. *Nano Letters* **2005**, *5*, 2164  
*Controlled synthesis of hyperbranched inorganic nanocrystals with rich three-dimensional structures.*
- Khalavka, Y.; Sönnichsen, C. *Advanced Materials* **2008**, *20*, 588  
*Growth of gold tips onto hyperbranched CdTe nanostructures.*
- Khon, E.; Hewa-Kasakarage, N. N.; Nemitz, I.; Acharya, K.; Zamkov, M. *Chemistry of Materials* **2010**, *22*, 5929  
*Tuning the Morphology of Au/CdS Nanocomposites through Temperature-Controlled Reduction of Gold-Oleate Complexes.*
- Khon, E.; Mereshchenko, A.; Tarnovsky, A. N.; Acharya, K.; Klinkova, A.; Hewa-Kasakarage, N. N.; Nemitz, I.; Zamkov, M. *Nano Letters* **2011**, *11*, 1792  
*Suppression of the Plasmon Resonance in Au/CdS Colloidal Nanocomposites.*
- Kirkendall, E. O. *Trans. AIME* **1942**, *147*, 104  
*Diffusion of Zinc in Alpha Brass.*
- Komura, T.; Yamaguchi, T.; Shimatani, H.; Okushio, R. *Electrochim Acta* **2004**, *49*, 597  
*Interfacial charge-transfer resistance at ionizable thiol monolayer-modified gold electrodes as studied by impedance spectroscopy.*
- Kremer, J. R.; Mastrorade, D. N.; McIntosh, J. R. *Journal of Structural Biology* **1996**, *116*, 71  
*Computer visualization of three-dimensional image data using IMOD.*
- Kuno, M.; Ahmad, O.; Protasenko, V.; Bacinello, D.; Kosel, T. H. *Chem. Mat.* **2006**, *18*, 5722  
*Solution-based straight and branched CdTe nanowires.*
- Lee, J.; Govorov, A. O.; Kotov, N. A. *Angewandte Chemie* **2005**, *117*, 7605  
*Nanoparticle Assemblies with Molecular Springs: A Nanoscale Thermometer.*
- Lee, J.; Javed, T.; Skeini, T.; Govorov, A. O.; Bryant, G. W.; Kotov, N. A. *Angewandte Chemie International Edition* **2006**, *45*, 4819  
*Bioconjugated Ag Nanoparticles and CdTe Nanowires: Metamaterials with Field-Enhanced Light Absorption.*

- Lee, J.; Park, J. C.; Song, H. *Advanced Materials* **2008**, *20*, 1523  
*A nanoreactor framework of a Au@SiO<sub>2</sub> yolk/shell structure for catalytic reduction of p-nitrophenol.*
- Lee, K.-S.; El-Sayed, M. A. *J. Phys. Chem. B* **2006**, *110*, 19220  
*Gold and Silver Nanoparticles in Sensing and Imaging: Sensitivity of Plasmon Response to Size, Shape, and Metal Composition.*
- Li, X. H.; Lian, J.; Lin, M.; Chan, Y. T. *Journal of the American Chemical Society*, *133*, 672  
*Light-Induced Selective Deposition of Metals on Gold-Tipped CdSe-Seeded CdS Nanorods.*
- Lide, D. R., Ed. *CRC Handbook of Chemistry and Physics*; 85th ed.; CRC Press, 2004.
- Lim, J.; Lanni, C.; Evarts, E. R.; Lanni, F.; Tilton, R. D.; Majetich, S. A. *ACS Nano* **2010**, *5*, 217  
*Magnetophoresis of Nanoparticles.*
- Liong, M.; Angelos, S.; Choi, E.; Patel, K.; Stoddart, J. F.; Zink, J. I. *Journal of Materials Chemistry J. Mater. Chem.* **2009**, *19*, 6251  
*Mesostructured multifunctional nanoparticles for imaging and drug delivery.*
- Liu, M. Z.; Guyot-Sionnest, P. *J. Phys. Chem. B* **2004**, *108*, 5882  
*Synthesis and Optical Characterization of Au/Ag Core/Shell Nanorods.*
- Manna, L.; Milliron, D. J.; Meisel, A.; Scher, E. C.; Alivisatos, A. P. *Nature Materials* **2003**, *2*, 382  
*Controlled growth of tetrapod-branched inorganic nanocrystals.*
- Manna, L.; Scher, E. C.; Alivisatos, A. P. *Journal of the American Chemical Society* **2000**, *122*, 12700  
*Synthesis of soluble and processable rod-, arrow-, teardrop-, and tetrapod-shaped CdSe nanocrystals.*
- McFarland, A. D.; Van Duyne, R. P. *Nano Letters* **2003**, *3*, 1057  
*Single silver nanoparticles as real-time optical sensors with zeptomole sensitivity.*
- Menagen, G.; Macdonald, J. E.; Shemesh, Y.; Popov, I.; Banin, U. *Journal of the American Chemical Society* **2009**, *131*, 17406  
*Au Growth on Semiconductor Nanorods: Photoinduced versus Thermal Growth Mechanisms.*
- Menagen, G.; Mocatta, D.; Salant, A.; Popov, I.; Dorfs, D.; Banin, U. *Chemistry of Materials* **2008**, *20*, 6900

*Selective Gold Growth on CdSe Seeded CdS Nanorods.*

Meyer, R. O. *Phys. Rev. J1 - PR* **1967**, *163*, 641 LP

*Activity-Coefficient and Vacancy Flow Effects on Tracer Diffusion Coefficients in Silver-Gold Alloys.*

Meyer, R. O. *Phys. Rev. J1 - PR* **1969**, *181*, 1086

*Pressure and Vacancy-Flow Effects on Kirkendall Shift in Silver-Gold Alloys.*

Milliron, D. J.; Hughes, S. M.; Cui, Y.; Manna, L.; Li, J. B.; Wang, L. W.; Alivisatos, A. P. *Nature* **2004**, *430*, 190

*Colloidal nanocrystal heterostructures with linear and branched topology.*

Mock, J. J.; Smith, D. R.; Schultz, S. *Nano Letters* **2003**, *3*, 485

*Local refractive index dependence of plasmon resonance spectra from individual nanoparticles.*

Mokari, T.; Costi, R.; Sztrum, C. G.; Rabani, E.; Banin, U. *physica status solidi (b)* **2006**, *243*, 3952

*Formation of symmetric and asymmetric metal-semiconductor hybrid nanoparticles.*

Mokari, T.; Costi, R.; Sztrum, C. G.; Rabani, E.; Banin, U. *Physica Status Solidi B-Basic Solid State Physics* **2006**, *243*, 3952

*Formation of symmetric and asymmetric metal-semiconductor hybrid nanoparticles.*

Mokari, T.; Rothenberg, E.; Popov, I.; Costi, R.; Banin, U. *Science* **2004**, *304*, 1787

*Selective Growth of Metal Tips onto Semiconductor Quantum Rods and Tetrapods.*

Mokari, T.; Sztrum, C. G.; Salant, A.; Rabani, E.; Banin, U. *Nature Materials* **2005**, *4*, 855

*Formation of asymmetric one-sided metal-tipped semiconductor nanocrystal dots and rods.*

Mulvaney, P. *Langmuir* **1996**, *12*, 788

*Surface plasmon spectroscopy of nanosized metal particles.*

Murphy, C. J.; Gole, A. M.; Hunyadi, S. E.; Stone, J. W.; Sisco, P. N.; Alkilany, A.; Kinard, B. E.; Hankins, P. *Chemical Communications* **2008**, 544

*Chemical sensing and imaging with metallic nanorods.*

Nikoobakht, B.; El-Sayed, M. A. *Chem. Mat.* **2003**, *15*, 1957

*Preparation and growth mechanism of gold nanorods (NRs) using seed-mediated growth method.*

Nusz, G. J.; Marinakos, S. M.; Curry, A. C.; Dahlin, A.; Hook, F.; Wax, A.; Chilkoti, A. *Analytical Chemistry* **2008**, *80*, 984

*Label-free plasmonic detection of biomolecular binding by a single gold nanorod.*

Perez-Juste, J.; Pastoriza-Santos, I.; Liz-Marzan, L. M.; Mulvaney, P. *Coordination Chem Rev* **2005**, *249*, 1870

*Gold nanorods: Synthesis, characterization and applications.*

Phala, N. S.; van Steen, E. *Gold Bull* **2007**, *40*, 150

*Intrinsic reactivity of gold nanoparticles: Classical, semi-empirical and DFT studies.*

Pinchuk, A.; von Plessen, G.; Kreibig, U. *J Phys D Appl Phys* **2004**, *37*, 3133

*Influence of interband electronic transitions on the optical absorption in metallic nanoparticles.*

Raschke, G.; Brogl, S.; Susa, A. S.; Rogach, A. L.; Klar, T. A.; Feldmann, J.; Fieres, B.; Petkov, N.; Bein, T.; Nichtl, A.; Kürzinger, K. *Nano Letters* **2004**, *4*, 1853

*Gold nanoshells improve single nanoparticle molecular sensors.*

Raschke, G.; Kowarik, S.; Franzl, T.; Sönnichsen, C.; Klar, T. A.; Feldmann, J.; Nichtl, A.; Kürzinger, K. *Nano Letters* **2003**, *3*, 935

*Biomolecular recognition based on single gold nanoparticle light scattering.*

Ravishankar, N.; Viswanath, B.; Kundu, P.; Halder, A. *Journal of Physical Chemistry C* **2009**, *113*, 16866

*Mechanistic Aspects of Shape Selection and Symmetry Breaking during Nanostructure Growth by Wet Chemical Methods.*

Ress, D. B.; Harlow, M. L.; Marshall, R. M.; McMahan, U. J. *Structure* **2004**, *12*, 1763

*Methods for generating high-resolution structural models from electron microscope tomography data.*

Rogach, A. L.; Franzl, T.; Klar, T. A.; Feldmann, J.; Gaponik, N.; Lesnyak, V.; Shavel, A.; Eychmüller, A.; Rakovich, Y. P.; Donegan, J. F. *The Journal of Physical Chemistry C* **2007**, *111*, 14628

*Aqueous Synthesis of Thiol-Capped CdTe Nanocrystals: A State-of-the-Art.*

Rosi, N. L.; Mirkin, C. A. *Chem. Rev.* **2005**, *105*, 1547

*Nanostructures in biodiagnostics.*

Salant, A.; Amitay-Sadovskiy, E.; Banin, U. *Journal of the American Chemical Society* **2006**, *128*, 10006

*Directed self-assembly of gold-tipped CdSe nanorods.*

Saunders, A. E.; Popov, I.; Banin, U. *J Phys Chem B* **2006**, *110*, 25421

*Synthesis of hybrid CdS-Au colloidal nanostructures.*

Shaviv, E.; Banin, U. *Acs Nano* **2010**, *4*, 1529

*Synergistic Effects on Second Harmonic Generation of Hybrid CdSe-Au Nanoparticles.*

Sheldon, M. T.; Trudeau, P. E.; Mokari, T.; Wang, L. W.; Alivisatos, A. P. *Nano Letters* **2009**, *9*, 3676

*Enhanced Semiconductor Nanocrystal Conductance via Solution Grown Contacts.*

Sonnichsen, C.; Becker, J.; Zins, I.; Jakab, A.; Khalavka, Y.; Schubert, O. *Nano Letters* **2008**, *8*, 1719

*Plasmonic focusing reduces ensemble linewidth of silver-coated gold nanorods.*

Sönnichsen, C.; Franzl, T.; Wilk, T.; von Plessen, G.; Feldmann, J.; Wilson, O.; Mulvaney, P. *Phys. Rev. Lett.* **2002**, *88*, 077402

*Drastic reduction of plasmon damping in gold nanorods.*

Sonnichsen, C.; Shaviv, E.; Schubert, O.; Alves-Santos, M.; Goldoni, G.; Di Felice, R.; Vallee, F.; Del Fatti, N.; Banin, U. *Acs Nano* **2011**, *5*, 4712

*Absorption Properties of Metal-Semiconductor Hybrid Nanoparticles.*

Steiner, D.; Dorfs, D.; Banin, U.; Della Sala, F.; Manna, L.; Millo, O. *Nano Letters* **2008**, *8*, 2954

*Determination of Band Offsets in Heterostructured Colloidal Nanorods Using Scanning Tunneling Spectroscopy*

*doi:10.1021/nl801848x.*

Steiner, D.; Mokari, T.; Banin, U.; Millo, O. *Phys. Rev. Lett.* **2005**, *95*

*Electronic structure of metal-semiconductor nanojunctions in gold CdSe nanodumbbells.*

Subramanian, V.; Wolf, E. E.; Kamat, P. V. *J. Am. Chem. Soc.* **2004**, *126*, 4943

*Catalysis with TiO<sub>2</sub>/Gold Nanocomposites. Effect of Metal Particle Size on the Fermi Level Equilibration.*

Sun, Y.; Wiley, B.; Li, Z.-Y.; Xia, Y. *Journal of the American Chemical Society* **2004**, *126*, 9399

*Synthesis and Optical Properties of Nanorattles and Multiple-Walled Nanoshells/Nanotubes Made of Metal Alloys.*

Sun, Y.; Xia, Y. *Analytical Chemistry* **2002**, *74*, 5297

*Increased Sensitivity of Surface Plasmon Resonance of Gold Nanoshells Compared to That of Gold Solid Colloids in Response to Environmental Changes.*

Tsukuda, T.; Tsunoyama, H.; Ichikuni, N.; Sakurai, H. *Journal of the American Chemical Society* **2009**, *131*, 7086

*Effect of Electronic Structures of Au Clusters Stabilized by Poly(N-vinyl-2-pyrrolidone) on Aerobic Oxidation Catalysis.*

Viswanath, B.; Kundu, P.; Halder, A.; Ravishankar, N. *J. Phys. Chem. C* **2009**, *113*, 16866

*Mechanistic Aspects of Shape Selection and Symmetry Breaking during Nanostructure Growth by Wet Chemical Methods.*

Viswanath, B.; Kundu, P.; Mukherjee, B.; Ravishankar, N. *Nanotechnology* **2008**, *19*

*Predicting the growth of two-dimensional nanostructures.*

Wood, A.; Giersig, M.; Mulvaney, P. *The Journal of Physical Chemistry B* **2001**, *105*, 8810

*Fermi Level Equilibration in Quantum Dot-Metal Nanojunctions.*

Xia, Y. N.; Xiong, Y. J.; Lim, B.; Skrabalak, S. E. *Angew Chem Int Edit* **2009**, *48*, 60

*Shape-Controlled Synthesis of Metal Nanocrystals: Simple Chemistry Meets Complex Physics?*

Yang, J.; Lu, L.; Wang, H.; Zhang, H. *Scripta Materialia* **2006**, *54*, 159

*Synthesis of Pt/Ag bimetallic nanorattle with Au core.*

Yin, Y.; Alivisatos, A. P. *Nature* **2005**, *437*, 664

*Colloidal nanocrystal synthesis and the organic-inorganic interface.*

Yin, Y.; Erdonmez, C.; and Alivisatos, A. P. *Paper LBNL* **2006**, 60696

*Faceting of Nanocrystals during Chemical Transformation: From Solid Silver Spheres to Hollow Gold Octahedra.*

Yin, Y.; Erdonmez, C. K.; Cabot, A.; Hughes, S.; Alivisatos, A. P. *Advanced Functional Materials* **2006**, *16*, 1389

*Colloidal Synthesis of Hollow Cobalt Sulfide Nanocrystals.*

Yin, Y.; Rioux, R. M.; Erdonmez, C. K.; Hughes, S.; Somorjai, G. A.; Alivisatos, A. P. *Science* **2004**, *304*, 711

*Formation of Hollow Nanocrystals Through the Nanoscale Kirkendall Effect.*

Yu, W. W.; Qu, L.; Guo, W.; Peng, X. *Chem. Mat.* **2003**, *15*, 2854

*Experimental Determination of the Extinction Coefficient of CdTe, CdSe, and CdS Nanocrystals*  
doi:10.1021/cm034081k.

Zhao, N.; Liu, K.; Greener, J.; Nie, Z. H.; Kumacheva, E. *Nano Letters* **2009**, *9*, 3077

*Close-Packed Superlattices of Side-by-Side Assembled Au-CdSe Nanorods.*

Zhu, J.; Peng, H.; Chan, C. K.; Cui, Y. *Nano Letters* **2007**, *7*, 1095

*Hyperbranched Lead Selenide Nanowire Networks.*

## Appendix A Synthesis of substrate structures

### Synthesis of gold nanorods

Inga Zins and Andreas Henkel provided the gold nanorods used in this study. The gold nanoparticles were produced by the seeded-growth technique according to the report of Nikoobath et al. [*Nikoobakht, 2003*] in a highly concentrated aqueous cetyltrimethylammoniumbromide solution (CTAB, Sigma-Aldrich). Typically The seeds are prepared by adding 50  $\mu\text{L}$  of 0.1 M hydrogen tetrachloroaurate(III) hydrate ( $\text{HAuCl}_4$ , Sigma-Aldrich) to 5.0 mL deionized water (18 M $\Omega$ m) and mixed with 5.0 mL of 0.2 M cetyltrimethylammoniumbromide solution (CTAB, Sigma-Aldrich). Under vigorous shaking 0.60 mL of ice-cold 0.01 sodium borohydride solution ( $\text{NaBH}_4$ , Aldrich) are added resulting in the formation of a brownish yellow solution.

The seed solution is kept at 37°C for 2 h before use. Gold Nanorods are produced by diluting 50  $\mu\text{L}$  of 0.1 M  $\text{HAuCl}_4$  with 5.0 mL deionized water and mixing with 5.0 mL of 0.2 M CTAB solution. Typically 20  $\mu\text{L}$  of 0.04 M silver nitrate ( $\text{AgNO}_3$ , Sigma-Aldrich ) and 70  $\mu\text{L}$  of 0.0788 M l-ascorbic acid (Sigma) are added (in this order), which turns the dark yellow solution transparent. After final addition of 12  $\mu\text{L}$  of seeds, the solution gradually develops a strong blue or brown color (depending on their final size and shape) within 10-20 min, indicating the formation of gold nanorods. (Zins Inga)

### Nanorattles synthesis

I used a procedure described in Liu et al. [*Liu, 2004*] Solution of the gold rods was centrifuged once and re-dispersed in 0.1 M CTAB. 0.8 ml of the CTAB coated gold rods solution is diluted in 4 ml of 1 wt % aqueous Polyvinylpyrrolidone (PVP, Aldrich). To the mixture of PVP, CTAB and gold

nanoparticles, I added 180 $\mu$ l (360 $\mu$ l) of 1 mM AgNO<sub>3</sub> (Sigma-Aldrich) and 100  $\mu$ L (200  $\mu$ L) of 0.1 M ascorbic acid (Sigma). Adding 200  $\mu$ L of 0.1 M NaOH (Merck) starts the coating reaction and leads to a color change within a few minutes. I kept the molar ratio between AgNO<sub>3</sub>, ascorbic acid and NaOH constant (0.6:25:50) when the concentration of silver nitrate is changed. 180 $\mu$ L/360 $\mu$ l of AgNO<sub>3</sub> results in 3 nm / 6nm coating thickness, respectively.

### **Synthesis of CdTe hyperbranched and rod-shaped nanoparticles**

CdTe hyperbranched particles are synthesized in tri-octylphosphine oxide (TOPO) by reacting tri-octylphosphine telluride (TOP=Te) with Cd - phosphonic acid (PA) complexes under argon atmosphere.[*Kanaras, 2005*]

Materials: CdO (>99,99%), Te(99,8%), 2-carboxyethyl phosphonic acid CEPA (94%), tri-n-octyl phosphine oxide TOP (>90%), tri-n-octyl phosphine oxide TOPO (99%), were purchased from Sigma-Aldrich, N-tetradecylphosphonic acid TDPA (98%), all solvents (>99,5%) from CarlRoth. All chemicals were used as received.

CdTe hyperbranched ‘substrates’ were synthesized according to the protocol described in detail in Kanaras et al.[*Kanaras, 2005*]: CdO (0.15g, 1.1 mmole) was added in a mixture of TDPA (1 g, 3.59 mmole), CEPA (0.05 g, 0.32 mmole), and TOPO (3 g, 7.7 mmole), heated at 150 °C and kept under vacuum for 30 min to remove small amounts of water. Then the temperature was set at 335°C and the brownish mixture was left under argon for 1 hour. This step resulted in a colorless solution due to the decomposition of the CdO and the formation of a Cd /phosphonic acid complex. TOP (1.2 g , 3.23 mmole) was injected and the temperature was adjusted to 335 °C. Te and Se stock solutions were prepared by dissolving Te in TOP (5%, 3.1 % w/w, respectively). The mixture of Te:TOP

(0.30 g, 0.117 mmole) was injected into the hot reaction solution and the temperature was set to 330 °C (For all experiments the volume of the injected Te precursor was kept constant). The color changed from colorless to brownish within 4-5 minutes indicating the formation of nanocrystals. The solution was left at 330 °C for another 20 min before it was cooled down to 100 °C. Toluene (3 ml) was injected and the particles precipitated with isopropanol. To purify the particles from the reactants, the solution was centrifuged and the sediment re-dissolved in toluene. After a second precipitation with isopropanol, the sediment was re-dissolved in chloroform and kept for further analysis. Some particles settle down over time, but are easily re-suspended by sonication.

We took the molar ratio of Cd:Te:TDPA:CEPA of 1:1:0.117:1.8:0.16 for the main and 1.1:0.234:1.8:0.16 for the control experiments. The nanoparticles were purified from the growth mixture by precipitation with isopropanol, centrifugation and resuspension in toluene (twice). At the end, the particles were dissolved in 20 ml of chloroform.

Rods of CdTe were synthesised in a coordinating solvent by sequential chalcogenide precursor injection similar to the procedure reported by Shien et al.<sup>42</sup> The cadmium precursor was prepared by degassing a mixture of 0.114 g CdO (0.89 mmol), 0.43 g n-tetradecylphosphonic acid (TDPA) (0.155 mmol) and 7 g of trioctylphosphine oxide (TOPO) at 65 °C for 3 h. The mixture was heated slowly to 320 °C under argon and then cooled to 300 °C. The tellurium precursor was prepared by dissolving 0.2 g of Te powder in 4 ml of trioctylphosphine (TOP) and stirring for 72 h at room temperature. Growth was initiated by injecting the Te precursor in 0.25 ml volumes four times, every 2 min, into the hot reaction mixture. To remove the reaction mixture, the nanorods were precipitated with isopropanol, washed by centrifugation and re-suspension in toluene (twice). Finally, the particles were dissolved in 20 ml of chloroform.

### **Synthesis of rodshaped CdS and CdSe/CdS semiconductor nanorods**

*Materials.* All chemicals, except ethanol, were used as received without further purification. Chloroauric acid trihydrate ( $\text{HAuCl}_4 \cdot 3\text{H}_2\text{O}$ , 99.9%), Sulfur (S, 99.998%), Selenium (Se, powder 100 mesh 99.5%), Cadmium Oxide ( $\text{CdO}$ , 99.99%), poly (vinylpyrrolidone) (PVP) (MW 30000,), mercaptoundecanoic acid (98 %) (MUA), anhydrous Chloroform, and Toluene were purchased from Sigma-Aldrich. Trioctylphosphine (TOP, 97%) was purchased from Fluka. denaturated Ethanol was from Roth ( $\text{EtOH}$ ,  $\geq 99.8\%$ ). Trioctylphosphine oxide (TOPO, 99%) and Tributylphosphine (TBP, 99%) were purchased from Strem Chemicals; Octadecylphosphonic acid (ODPA, 99%) and Hexylphosphonic acid (HPA, 99%) were from Polycarbon Industries, Ethylene glycol was from CarlRoth (99%), 18 MOm deionized water (Millipore)

### **Synthesis of CdSe nanoseeds.**

All syntheses are carried out under Ar atmosphere in a glovebox. CdSe quantum dots are synthesized according to the procedure of Manna *et al.*[Carbone, 2007] In brief, 3.700g of TOPO, 0.280g of ODPA and 0.060g of CdO are stirred in a 50 mL flask, heated to  $150^\circ\text{C}$  and exposed to vacuum for 1 hour. Afterwards, the solution is heated to approx.  $300^\circ\text{C}$  while flushing the flask with Ar until it turns optically clear and colorless in order to decompose CdO. At this point, 1.5 g of TOP is injected into the flask and the temperature set to the value required for the injection of the Se:TOP solution (0.063g Se + 0.575g TOP). The Se:TOP solution is swiftly injected at  $370^\circ\text{C}$  and the heating mantle is removed after 1 min of growth reaction. Later, the CdSe nanoseeds are transferred to the glovebox and washed twice by precipitating them and then re-solubilizing them with methanol and anhydrous chloroform, respectively. In the last precipitation step, the nanoseeds are dissolved in TOP in a final CdSe dots concentration of  $150\mu\text{M}$  (calculated according to X. Peng *et al.*[Yu, 2003]).

### **Synthesis of CdSe/CdS nanorods.**

CdSe/CdS nanorods are synthesized using a seeded-growth approach.[*Carbone, 2007*] In a typical nanoparticle synthesis, 0.085 g of CdO is mixed together in a flask with 3.000 g of TOPO, 0.297 g of ODPA and 0.084 g of HPA. The flask is pumped to vacuum for about 1 hour at 150°C. Then, the resulting solution is heated to 350°C and flushed with Ar. At this point, 1.5 g of TOP is injected. After the temperature has recuperated the set value (350°C), a solution of S precursor-TOP-CdSe nanodots is swiftly injected into the flask. This kind of solution is prepared by dissolving 0.120 g of S in 1.5 g of TOP and adding 570 µl of a solution of CdSe dots (see above) dissolved in TOP (150 µM). After the injection, the dark red CdSe/CdS nanocrystal solution is allowed to grow for 6 min. The reaction is then stopped by removing the heating mantle. When the solution temperature cools down to about 60-70°C, the nanoparticles are transferred into the glovebox and purified twice by precipitating them with methanol and re-solubilizing them in anhydrous chloroform. If we assume that there is a CdSe seed inside every CdS rod, we get a nanoparticle mother solution concentration  $k_{jysd}$  (calculated from seeds).

### **Transfer of CdSe/CdS to the water phase.**

2-3 ml of as prepared nanorods in chloroform are mixed with 10 ml of mercaptoundecanoic acid in water (11 mg of MUA in 10 g of H<sub>2</sub>O, pH adjusted by KOH to 10) Solution was homogenized by ultrasound and left for the phase separation overnight. Water phase containing nanorods was separated and particles were washed from excess of MUA by adding small amount of Ethanol. centrifugation at 10000 rpm for 15 min. and then redispersion in Millipore water. Finally concentration of nanorods were standardized by dilution to achieve optical density 0.1 at 400 nm which we use as a reference point for dilutions.

### **Photo-induced Au reduction on semiconductor rods**

A volume of 200  $\mu\text{l}$  of a water based solution of the CdSe/CdS rods sample is added to a 3 ml of water and 200 ml of 1% PVP solution in a glass vial. Afterwards, 200  $\mu\text{L}$  of EG is added. Finally, we inject 200 ml of Au solution (0.01 M  $\text{HAuCl}_4 \cdot 3\text{H}_2\text{O}$  in water). The resulting mixture is then UV irradiated ( $\lambda = 366$  nm) in the darkness while stirring. The sample is allowed to grow under UV irradiation for up to 60 min with aliquots withdrawn at scheduled times (see main text). Finally, the growth reaction is stopped by interrupting the irradiation, and applying 10 min of centrifugation at 10 000 rpm, and re-solubilizing the precipitate in water. Depending on the dilution, the final sample appears red, dark or pale violet. In order to rule out any light absorbance of the glass vial for the UV irradiation (366 nm), a few control experiments with identical results were performed in a quartz cuvette. We have not observed any remarkable gold growth when no UV light was applied or vials made of brown glass were used.

### **Some Control Experiments**

*Without semiconductor nano-rods or dumbbells.*

To test the influence of UV irradiation on Au nucleation in the normal reaction conditions, we performed a control experiment without any semiconductor particles. 60 min of irradiation leads to the formation of small gold crystals in the range of 2-3 nm in diameter (Figure S4c).

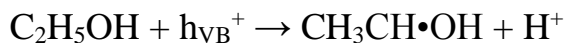
We think that particles produced by our new synthetic approach will allow to produce selectively functionalized particles and to understand exciton-plasmon interaction far more in details than it was done till now.

**Transferability to polar solvents.**

The sample semiconductor nanorods-large gold domain prepared as described in the previous paragraph is easily transferable in polar solvents through ligands exchange. Shortly the sample purified and finally solubilized in  $\text{CHCl}_3$  is mixed with 150  $\mu\text{L}$  of HS-PEG- $\text{OCH}_3$  (MW=5000 g/mol) in  $\text{CHCl}_3$  (0.002M) and shaken for 25 min. Afterward the particles are precipitated with hexane and re-suspended in a polar solvent such as ethanol or water.

**Control Experiments.** In order to test the role of each component in the reaction mixture, we carried out several control experiments employing nanodumbbells as starting material see Figure A1.

**2.7.1 Without EtOH.** In de-aerated organic solutions, the holes  $h^+$  generated by the semiconductor photo-excitation are supposed to be scavenged according to reactions (1) and (2) by the two organic solvents EtOH and  $\text{CHCl}_3$ .<sup>34</sup>



The absence of EtOH does not prevent the asymmetric gold growth entirely, although the growth is less uniform and the size of the gold domain is visibly decreased (Figure A1a). Experimentally, a gold solution (9 mg  $\text{HAuCl}_4 \cdot 3\text{H}_2\text{O}$ , 42 mg DDABr, 70 mg DDA, 3mL  $\text{CHCl}_3$ ) is dropwise injected (3 min) in a 1mL of chloroformic solution of Au-CdSe/CdS-Au nanodumbbells  $2.5 \cdot 10^{-7}$  M, then stirred and simultaneously UV irradiated for 60 min.

**2.7.2 In storage conditions.** Nanodumbbells are irradiated for a long-time (ca 30 min) before gold injection with the purpose of accumulating charge carriers in the metal. Surprisingly, there is no noticeable etching of the starting dumbbells from the irradiation probably due to the ability of the dumbbell's gold domains to store electrons.<sup>23</sup> The gold injection after pre-irradiation seems to induce dumbbell network-formation and randomly creates a few large gold islands

(Figure A1b). However, no large gold domains form on each particle as in our standard conditions. Experimentally, 400  $\mu\text{L}$  of dry ethanol is injected in 4 mL of nano-dumbbells chloroform solution  $6.25 \cdot 10^{-8}$  M and UV irradiated for 30 min. Later, the irradiation is interrupted and the typical gold solution injected dropwise and the sample stirred for 30 min.

**2.7.3 Without semiconductor nano-rods or dumbbells.** To test the influence of UV irradiation on Au nucleation in the normal reaction conditions, we performed a control experiment without any semiconductor particles. 60 min of irradiation leads to the formation of small gold crystals in the range of 2-3 nm in diameter (Figure A1c). Experimentally a gold solution (9 mg  $\text{HAuCl}_4 \cdot 3\text{H}_2\text{O}$ , 42 mg DDABr, 70 mg DDA, 3mL  $\text{CHCl}_3$ ) is furthermore diluted with 1 mL of chloroform and 400  $\mu\text{L}$  of ethanol and while stirring UV irradiated fo 60 min.

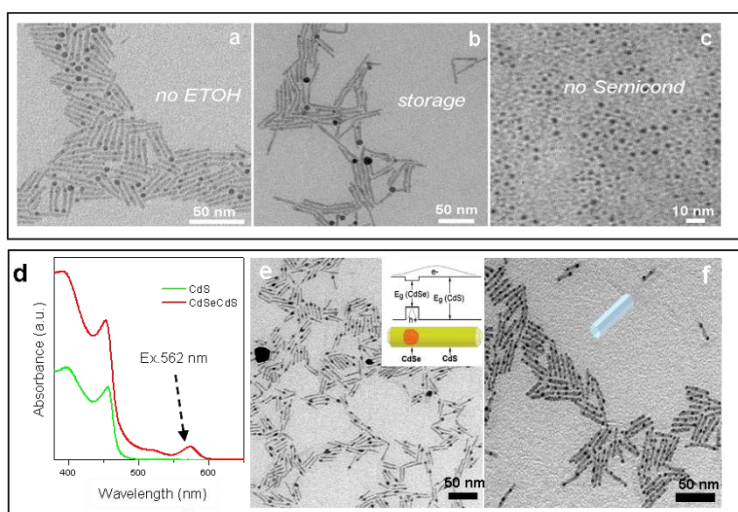


Figure A1. TEM images relative to the control experiments. (a) Experiment with no EtOH. The sample shows gold deposition on one dumbbell's end although the deposition is less uniform and much smaller than in the presence of EtOH. (b) This experiment describes the sample in conditions of charge carrier storage: before Au injection, the nanodumbbells have been irradiated for 30 min. The

particles show a tendency to network perhaps due to an attempt of the system to either delocalize as much as possible the charge carriers or to attract opposite charges localized on the small gold domains. (c) Control experiment achieved irradiating the Au growth solution without dumbbells. The experiment tests the tendency of gold to nucleate under 60 min of 366 nm UV irradiation. Without semiconductor seeds, only small gold crystals form. The scarce quality of the image reflects the difficulty to purify the small gold particles from the unreacted species. (d) original spectra of the CdS and CdSe/CdS nanorods: effect of irradiation at 562 nm. Irradiation at 562 nm induces excitation only in CdSe seeds. e-f) show TEM images of the CdSe/CdS and pure CdS nanorods (respectively, as indicated by the insets) after one hour of irradiation at 562 nm in the presence of a  $\text{Au}^{+3}$  solution. For the CdSe/CdS rods, gold nucleates preferentially in the area where the CdSe seed is localized and some isolated gold domains form (e). For CdS nanorods, gold nucleates on random positions on the nanorod surface (f).

**Preparation of flow cells.** For single-particle optical characterization in an oxygen-free environment, we use a flow cell made from a flat borosilicate glass capillary glued with epoxy to polyethylene tubing. After the flow cell is produced, motorized syringes allow for the addition of constant flow of liquids to the flow cell. First, washing stages are performed in order to ensure a complete removal of contaminants and to tune the glass wall's contact angle in the direction of the organic mercapto-silane solution. Then, the capillary is functionalized with mercapto-silane, which covalently binds to the cell walls through silanolic bonds. When a diluted nanoparticle solution is flowing in, the thiol groups of the mercaptosilane bind to the semiconductor particles. Before optical measurements, the unbound nanoparticles are washed out and the cell is filled with a mixture of EtOH and  $\text{CHCl}_3$ . The detailed 10-steps protocol is as follows (the injection rates

are always 1 mL/min): (1<sup>st</sup>) the cell is washed with 60mL of Hellmanex (Hellma)/Millipore H<sub>2</sub>O solution 4% v/v; (2<sup>nd</sup>) washing with 60 mL of Millipore H<sub>2</sub>O; (3<sup>rd</sup>) washing with 60 mL of pure EtOH. The flow cell is now transferred into the glovebox for the following steps and anhydrous solvents are used hereafter. (4<sup>th</sup>) Washing with 6 mL of pure CHCl<sub>3</sub>; (5<sup>th</sup>) functionalizing with 12 mL of mercapto-silane in CHCl<sub>3</sub> (5% v/v); (6<sup>th</sup>) washing with 6 mL of pure CHCl<sub>3</sub>; (7<sup>th</sup>) 4 mL of chloroformic solution 1.4 10<sup>-10</sup>M; (8<sup>th</sup>) washing with 2 mL of pure CHCl<sub>3</sub>; (9<sup>th</sup>) washing with 4 mL of EtOH in CHCl<sub>3</sub> (30% v/v); (10<sup>th</sup>) the glass capillary is filled again with a solution 30% (v/v) of EtOH in CHCl<sub>3</sub> and sealed tightly with two syringes at both ends of the flow cell. At this point, the flow cell is taken out of the glovebox and investigated under the microscope.

**Single particle microscopy.** Single particle scattering was recorded in a self-made dark-field microscope setup. The flow-cell was glued to a microscope slide at both ends and placed on the sample stage. Immersion oil is placed between the dark field condenser and the microscope slide, and between the microscope slide and the flow cell to avoid refraction of the illuminating light. The sample is observed with an oil immersion microscope objective for the highest possible magnification and contrast (Carl-Zeiss Achroplan 100x, oil iris). Images are recorded in regular time intervals using an imaging spectrometer (SP2300i, Acton Research) equipped with a Peltier-cooled CCD camera (Pixis 400 Princeton Instruments). For observing the CdS/CdSe quantum dot blinking, we use 1 s exposure time with zero delay between exposures for 5 minutes. For observing the growth of the gold domains, we use 30 ms exposure time in 30 sec time intervals for 60 minutes. The intensity of a structure-free area in close vicinity to the particle under investigation is used for background correction of the particle signal.

**Estimation of laser illumination intensity.** To estimate the laser light intensity at the sample level, we measured the response of a regular photodiode (Siemens BPW 34). The diode is initially calibrated using the diode laser, an optical power sensor (Thorlabs S130A), neutral optical filters, and a  $10\text{k}\Omega$  resistor as load. If the diode is positioned in the place of the sample, the measured voltage drop is 88 mV, which corresponds to a laser power of 0.8 mW over the field of view or an irradiance of  $6\text{ W/cm}^2$ .

## Acknowledgements



## Curriculum vitae

**Date of birth:** February, 9, 1983

**Birth-place:** Stryy, Lviv, Ukraine

**E - mail:** [ykhalavk@uni-mainz.de](mailto:ykhalavk@uni-mainz.de)

**ResearcherID:** <http://www.researcherid.com/rid/A-6442-2008>



### Education

Since 07/2007 – PhD student in University of Mainz

09/2004 – 06/2005 Yuriy Fedkovich Chernivtsi National University, Chernivtsi. Master's degree in chemistry, honours diploma. Master's thesis: "The Technology of CdTe Nanoparticles' Synthesis". Supervisor Prof. L.Shcherbak

09/2000 – 06/2004 Yuriy Fedkovich Chernivtsi National University named after Yuriy Fedkovich, Bachelor's degree in Chemistry.

### Employment

Since .2012 - Assistant, Chernivtsi National University.

01/2011 – 03/2011 Wiss.Mitarbeiter, Institut für Physikalische Chemie, Uni-Mainz, Germany

09/2010 – 12/2011 Assistant, Chernivtsi national university, Institute of Inorganic chemistry.

09/2007 – 08/2010 MATCOR-scholarship holder University of Mainz.

10/2006 – 08/2007 Wiss.Mitarbeiter, Institut für Physikalische Chemie, Uni-Mainz, Germany

09/2005 – 08/2006 Assistant, Chernivtsi national university, Institute of Inorganic chemistry.